Journal of Research of the National Bureau of Standards

Volume 89 | Number 3 | May-June

Pressure–Volume–Temperature Relationships for Normal Deuterium Between 18.7 and 21.0 K
L. A. Schwalbe and E. R. Grilly 227

An Equilibrium Model for the Calculation of Activity and Osmotic Coefficients in Aqueous Solutions
Robert N. Goldberg 251

An Absolute Electric Current Probe Based on the Faraday Effect
W. Caton and J. Katzenstein 265

A Head-Space Method for Measuring Activity Coefficients, Partition Coefficients, and Solubilities of Hydrocarbons in Saline Solutions
Stanley P. Wasik, Frederick P. Schwarz, Yadu B. Tewari, Michele M. Miller, and J. H. Purnell .. 273

List of Publications of the National Bureau of Standards 279

ISSN 0160-1741 **Library of Congress Catalog Card No.: 63-37059**

The Journal of Research of the National Bureau of Standards features advances in measurement methodology and analyses consistent with the NBS responsibility as the nation's measurement science laboratory. It includes reports on instrumentation for making accurate and precise measurements in fields of physical science and engineering, as well as the mathematical models of phenomena which enable the predictive determination of information in regions where measurements may be absent. Papers on critical data, calibration techniques, quality assurance programs, and well characterized reference materials reflect NBS programs in these areas. Special issues of the Journal are devoted to invited papers in a particular field of measurement science. Survey articles appear periodically on topics related to the Bureau's technical and scientific programs. As a special service to subscribers each issue contains complete citations to all recent NBS publications in NBS and non-NBS media.

Issued six times a year. Annual subscriptions: domestic $17.00; foreign $21.25. Single copy, $3.00 domestic; $3.75 foreign.

United States Government Printing Office, Washington: 1984
Order all publications from the Superintendent of Documents
U.S. Government Printing Office, Washington, DC 20402

The Secretary of Commerce has determined that the publication of the periodical is necessary in the transaction of the public business required by law of this Department. Use of funds for printing this periodical has been approved by the Director of the Office of Management and Budget through April 1, 1985.

JOURNAL OF RESEARCH of the National Bureau of Standards
Vol. 89, No. 3, May-June 1984

Pressure-Volume-Temperature Relationships for Normal Deuterium Between 18.7 and 21.0 K

L. A. Schwalbe and E. R. Grilly
Los Alamos National Laboratory, Los Alamos, NM 87545

Accepted: December 19, 1983

Analytical expressions are derived for the melting line and liquid equation of state of normal deuterium near the triple point. Melting pressures were measured between the triple point and 20.4 K. These results combined with existing pressure measurements along the saturated liquid-vapor curve fix an accurate value, T_{tp}=18.723 K, for the triple-point temperature. Data for the isothermal compressibility and thermal expansion coefficients of the liquid were taken over the temperature and pressure ranges 18.8 to 21.0 K and 4 to 70 bar, respectively. The liquid molar volume was measured at nine points below 20.4 K. All liquid PVT data are shown to be internally consistent. Measurements of the volume changes on melting are also presented. The heat of fusion and the solid molar volume at melting are deduced from these data. Also included are detailed comparisons of our results with existing data. A critical appraisal is given of all measured thermodynamic quantities in this regime.

Key words: compressibility; deuterium; equation of state; melting pressure; ortho-para concentration; pressure-volume-temperature (PVT); thermal expansion; thermodynamic properties; triple point.

1. Introduction

Interest in the properties of the condensed-phase hydrogen systems has continued for well over 50 years. As early as 1935, Clusius and Bartholome [1][1] published the first comprehensive thermodynamic study of normal deuterium (n-D_2) in the triple-point region. These results were followed by others [2,3] and included in the 1948 review article by Woolley et al.[4]. Since that time, there have been some additional measurements in this regime [5,6], but most efforts have been toward establishing the pressure-volume-temperature (PVT) relationship over extended ranges of temperatures and pressures.

By 1959, an incomplete collection of fluid-phase density data was available at various intervals in the temperature range from the triple point to 420 K and at pressures to 3 kbar. Prydz [7,8] critically reviewed these results, fit them to a modified Strobridge equation, and derived analytical expressions for selected thermodynamic properties.

More recently Mills et al. [9] measured simultaneously the molar volume and ultrasound velocity of fluid n-D_2 in a piston-cylinder apparatus. The data spanned temperatures of 75 to 300 K and pressures of 2 to 20 kbar. The results were fit to a Benedict-type equation of state, and analytic forms were derived for both constant-volume and constant-pressure heat capacities over these ranges. In a companion to this work, Liebenberg et al. [10] reported measurements of the melting line from 4 to 19 kbar and the corresponding changes in the molar volume and longitudinal sound velocity. From these data, they derived the entropy change on melting, the adiabatic compressibility for the solid and other thermodynamic properties.

Most work on solid deuterium has been done at low temperatures and low pressures although the volume-pressure dependence at 4 K was measured to 20 [11] and 25 kbar [12]. Recently, solid-phase isochoric equation-of-state data were taken to 2 kbar [13,14].

About the Authors, Paper: The work reported on was performed at the Los Alamos National Laboratory where L. A. Schwalbe, a physicist, remains and from which E. R. Grilly, also a physicist, is retired. The work was supported by the Fusion Target Fabrication Group at Los Alamos.

[1]Figures in brackets indicate literature references at the end of this paper.

The purpose of this study is to supplement existing PVT and melting data with accurate and precise measurements[2] in the region of the phase diagram near the triple point. Data are presented for the pressures and liquid molar volume of n-D_2 along the melting line from the triple point to 20.4 K. The isothermal compressibility and thermal expansion coefficients of the liquid are given over the same temperature range and at pressures between 4 and 70 bar. The combined liquid data are fitted to an empirical equation of state and are shown to be internally consistent.

Measurements of the volume changes on melting are also presented. The heat of fusion and the solid molar volume at melting are deduced from these data. Throughout the discussion, we have included detailed comparisons of our results with existing data and have attempted to provide a critical appraisal of all measured quantities in this regime.

2. Experimental

Our studies on n-D_2 were carried out with essentially the same apparatus as that used earlier for similar work [15-17] on ^{3}He and ^{4}He. The pressure cell, which was referred to in previous descriptions [16,17] as "cell I," consisted of three BeCu diaphragms that were welded together at their circumference and separated by 0.3 mm gaps (see fig. 1). The lower gap was connected to a capillary tube and remained open to a room-temperature helium gas-handling system. With this arrangement P_l, the pressure of the lower-cell volume, could be adjusted or measured directly. The upper cell gap served as the deuterium sample chamber; a fixed quantity of material could be maintained in its volume V_u by sealing the low-temperature valve. The sample pressure P_u was determined from the deflection of the upper diaphragm. Originally the deflection measurement was made with a linear differential transformer [15], but the capacitance technique was adopted because of its greater sensitivity [17].

Changes in the volume of the sample chamber depend upon changes in P_u, P_l, and the bath pressure P_b according to the equation

$$\Delta V_u=(S_u+S_l)\Delta P_u-S_l\Delta P_l-S_u\Delta P_b \qquad (1)$$

where S_u and S_l are pressure sensitivity factors of the volume changes to changes in the upper and middle diaphragm displacements, respectively.

The pressure sensitivity factors for the cell were not constants but varied reproducibly by 1 or 2% as P_l and P_u varied between 0 and 70 bars, the highest working pressures in this experiment. For the earlier helium measurements, these variations did not critically affect the results, but for the present work it was first necessary to calibrate the system more precisely. To do this, three separate sets of calibration measurements were run. In each, the procedure first involved loading the sample chamber with liquid p-H_2 at $T=20.00$ K and then "bleeding" small amounts from the cell through the valve and into a calibrated standard volume held nominally at room temperature. The quantity of material drawn from the cell was then measured and the corresponding changes in the sample volume ΔV_u were calculated using the p-H_2 density values tabulated by Goodwin et al. [18]. According to eq (1), isothermal changes

[2]Full data are available from the authors.

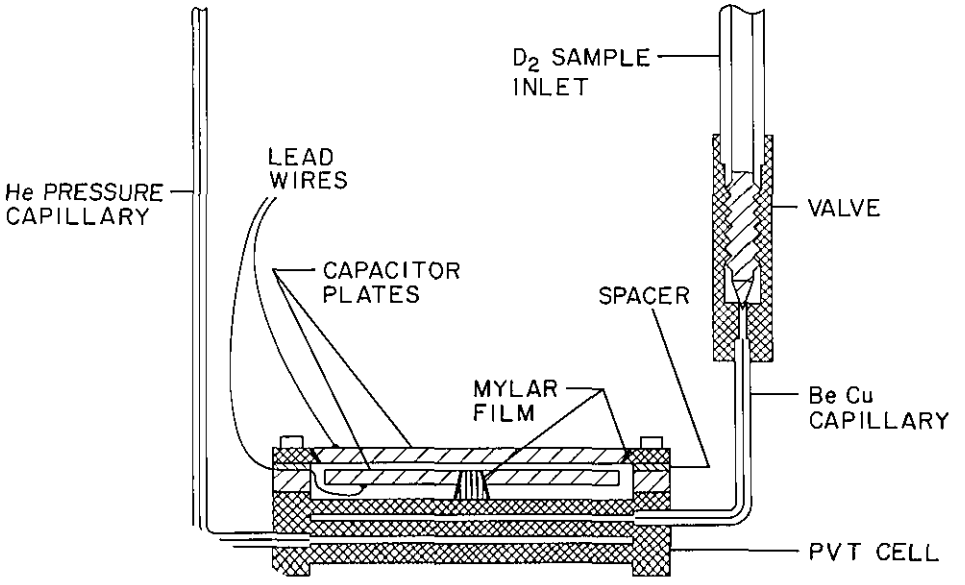

Figure 1—The pressure cell and low-temperature valve assembly.

in V_u under the constraints $\Delta P_u=0$, $\Delta P_u=\Delta P_l$, and $\Delta P_l=0$ yield the factors S_l, S_u, and S_u+S_l, respectively.

A consistent set of pressure sensitivity parameters was obtained at $T=20.000$ K for the entire working range of both upper- and lower-cell pressures. The quantities S_u and S_l that were used in the data analysis were accurate to $\pm 0.1\%$. Extrapolations of total volume measurements to $P_u=P_l=P_b=0$ absolute pressure determined V_{u0}, the zero-pressure volume of the sample chamber. The latter calibration was made at two separate times: initially, before any of the deuterium work was begun and again near its completion about 18 months later. The first set of measurements obtained an average value 0.37477 cm^3 for six separate runs; for the second set the average of five runs was 0.37426 cm^3. In the data analysis we used the mean of these two values, $V_0=0.37452$ cm^3, and set an accuracy limit of $\pm 0.15\%$ for this quantity. This error includes the $\pm 0.1\%$ uncertainty of the original p-H_2 density data [18].

Equation (1) has no explicit temperature dependence included. In this range, there are negligible effects introduced by the temperature coefficient of the cell material. The thermal expansion of BeCu should be comparable to that of Cu. Rubin et al. [19] reported a linear expansion coefficient of 6×10^{-6} K^{-1} for copper at 25 K. The effects introduced by thermal expansion are, therefore, about an order of magnitude smaller than the quoted uncertainties in our data. To check this explicitly, we measured thermal expansion coefficients of liquid hydrogen in our cell. Hydrogen data were taken at 0.4 K intervals between 19.0 K and 21.0 K along six isobars (5.48, 14.76, 28.52, 42.28, 56.05, and 69.81 bar). The measured values agree with those that Roder et al. [20] derived from the original density data of Goodwin et al. [18].

The uniform sample temperatures required for this study were maintained by holding the pressure cell assembly immersed in a bath of liquid 20 K-equilibrium hydrogen (e-H_2). Temperatures were controlled by regulating the bath pressure with a Baratron[3] Type 77H-1000 metal diaphragm gauge (0-1000 Torr range). Bath pressures were obtained directly with an 18-mm-bore mercury manometer. The mercury column heights were measured with a cathetometer, and standard corrections for the temperature and local gravity constant were applied to these readings. From these data the sample temperatures were calculated with the saturated liquid-vapor pressure equation of Souers et al. [21]:

$$\ln P_b(\text{torr}) = 10.57411 - 101.3378\ T^{-1} + 5.432005\times 10^{-2}\ T - 1.105632\times 10^{-4}\ T^2. \quad (2)$$

This function is identical to that defined by the International Practical Temperature Scale of 1968 (IPTS-68) [22] although it is expressed in somewhat different form.

Temperature precisions of slightly better than 1 mK were attainable with this procedure. From run to run, with the possible exceptions noted below, the scale seems to have been reproducible to within about ± 2 mK.

3. Results and Discussion

3.1 Melting Pressures

The melting pressures of n-D_2 were measured by closing the cell valve on a liquid-phase sample and increasing P_l until the capacitance readings showed the sample to be in the two-phase region. At each temperature, capacitance readings were recorded for several different P_l values. Finally, the valve was opened and the capacitance-pressure calibration was rechecked against the piston gauge. The results are given in table 1. Measurements were taken during four runs, each lasting one week; each run represents a separate filling of e-H_2 refrigerant.

It is important to note that all melting pressures reported here correspond to the "first-freeze" characteristics of the sample. The pressure-temperature measurements were recorded for small solid fractions ($<5\%$) of the two-phase mixture. In a later section, we discuss in more detail the problems involved with precision measurements of the sample pressure when larger relative quantities of solid are present.

Values for the slope of the melting curve are plotted in figure 2. Those obtained from run numbers 1, 2, 3b, and 4 were derived from consecutive melting pressure measurements. Those labeled "3a" were measured directly by temperature cycling a single sealed sample. The plot indicates a nearly linear temperature dependence for the slope. The melting line $P_m(T_m)$ should, therefore, be adequately represented by a quadratic function over this limited range. For the least-squares fit, we chose an equation of the form

$$P_m(T_m)=P_{tp}+A_1(T_m-T_{tp})+A_2(T_m-T_{tp})^2 \quad (3)$$

where A_1 and A_2 are fitting constants and P_{tp} and T_{tp} are parameters that represent the pressure and temperature values at the triple point. Our best fit gave $A_1=38.884$

[3]Certain trade names and company products are identified in order to adequately specify the experimental procedure. In no case does such identification imply recommendation or endorsement by the Los Alamos National Laboratory or the *Journal of Research* of the National Bureau of Standards, nor does it imply that the product is necessarily the best available for the purpose.

Table 1. Measured pressure and temperatures of normal deuterium along the melting line.

Run No. 1	T_m(K)	P_m(bar)	Run No. 2	T_m(K)	P_m(bar)	Run No. 3	T_m(K)	P_m(bar)	Run No. 4	T_m(K)	P_m(bar)
	20.407_7	69.61		19.504_2	31.90		19.703_0	40.03		20.306_4	65.16
	20.206_0	60.75		19.302_4	23.73		20.407_0	69.44		20.103_1	56.62
	20.006_6	52.40		19.102_2	15.72		20.204_3	60.86		19.902_4	48.24
	19.805_7	44.02		18.902_0	7.81		20.004_9	52.48		19.699_5	39.86
	19.605_5	36.10		20.007_0	52.57		19.802_2	44.08		19.504_4	31.88
	19.404_6	27.88		19.804_2	44.14		19.192_7	19.40		19.301_9	23.68
	19.198_2	19.61		19.603_8	35.93		19.000_9	11.75		19.100_4	15.64
	20.306_9	65.29		19.402_9	27.75					18.899_2	7.69
	20.107_1	56.83		20.407_6	69.44					19.404_1	27.79
	19.906_0	48.12		20.305_6	65.10					19.195_1	19.38
	19.704_6	39.79		20.205_6	60.83					19.000_7	11.65
	20.408_1	69.87		20.105_4	56.63					18.829_2	4.88
				19.906_2	48.05					19.603_8	36.04
										18.828_7	4.96

bar/K, $A_2=1.078$ bar/K^2, and $T_{tp}=18.7067$ K with $P_{tp}=0.17$ bar.

Grilly [23] reported a triple-point temperature of 18.73 K. The result obtained here 18.7067 K is considerably lower. We attempted to fit eq (3) by varying only A_1 and A_2 with $T_{tp}=18.73$ K and $P_{tp}=0.17$ bar held fixed, but the results showed large systematic deviations. We believe the difference is due to impurity effects in the actual fixed-point values of our sample lot. Mass spectrometric analysis of the sample material showed 0.75% HD present with no detectable traces of H_2, N_2, or H_2O at the 50 ppm sensitivity level. Sample impurities in low concentrations affect both triple-point parameters, but within the resolution limits of this experiment, the temperature T_{tp} is much more sensitively dependent on impurity effects than is the pressure P_{tp}. Therefore, in the final calculation we retained the fixed value $P_{tp}=0.17$ bar and allowed only T_{tp} to vary along with A_1 and A_2.

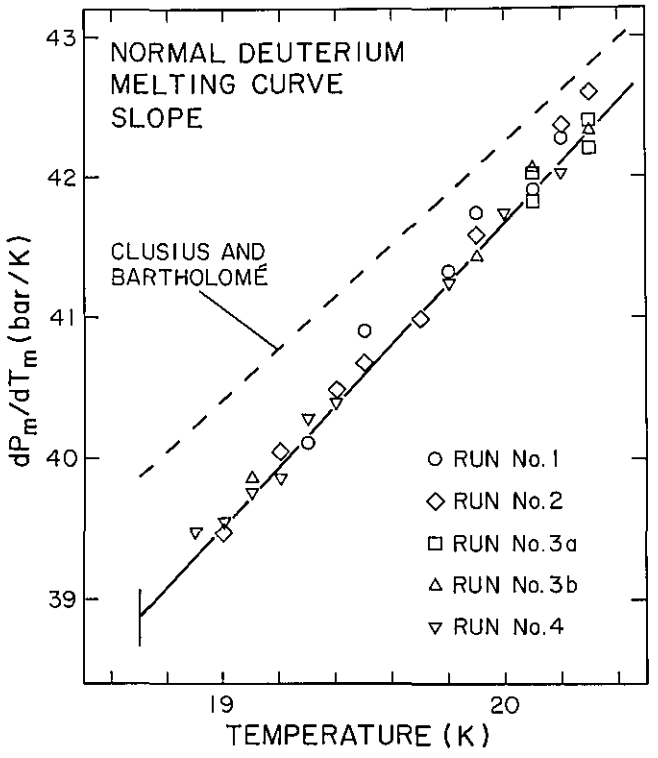

Figure 2—The slope of the melting curve. Data from runs 1, 2, 3b, and 4 were obtained by subtracting consecutive measurements of the melting pressure. Data from run 3a were measured by temperature cycling a single sealed sample. The solid line was obtained by evaluating eq (4). The dashed line is the slope of the melting function given by Clusius and Bartholome [1].

Equation (3) with the above parameters describes the melting line for our sample, but for pure n-D_2, a pressure correction must be applied. If this correction is proportional to the HD concentration and to the difference in pressure between the HD and D_2 melting curves, 0.6 bar should be subtracted from P_m in eq (3) to obtain the melting pressure of pure n-D_2.

A plot of the deviations of our data from eq (3) is shown in figure 3. With the exception of a few points, mainly all from the first run, the data appear to lie within ± 0.1 bar of the smooth curve. The precision of our measurements is comparable to that of Bereznyak and Sheinina [24], who measured the melting lines of e-H_2, n-H_2, and e-D_2 over roughly the same pressure interval. Their P_m measurements on e-D_2 exceed ours on n-D_2 by 1.5 bar at 18.8 K and 2.3 bar at 21.0 K. (This difference is similar to that observed between the melting lines of e-H_2 and n-H_2.) However, they observed a slope discontinuity in their e-D_2 melting curve at $T=19.02$ K and $P=14.2$ bar. Our data show no anomalous behavior anywhere in the range 18.7067 to 20.400 K.

An analytic form for the slope of the melting curve is obtained by differentiating eq (3) with respect to T_m:

$$\frac{dP_m}{dT_m}=A_1+2A_2(T_m-T_{tp}). \quad (4)$$

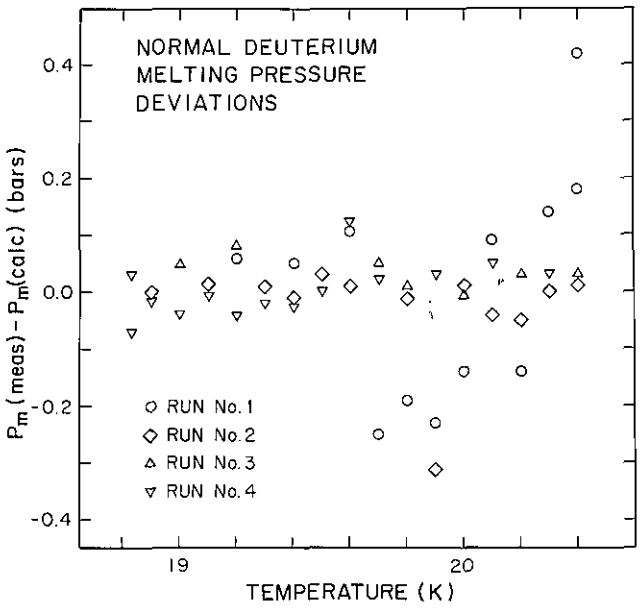

Figure 3—The deviations of the melting pressure data from the smooth curve defined by eq (3).

We have included in figure 2 a plot of eq (4) with the values A_1, A_2, and T_{tp} found above. This function represents the data for the slope of the melting curve to within $\pm 0.5\%$.

Other melting data are available for comparison. Among the earliest of these are the Clusius and Bartholome [1] results on n-D_2. These measurements extend from the triple point up in pressure to about 100 bar. Clusius and Bartholome employed a technique in which the liquid sample was held at nominally constant pressures while the surrounding n-H_2 bath pressure was gradually lowered. The freezing transition temperature was measured by observing the effect of the latent heat of the sample on the cryogen bath pressure. Their quoted temperatures were obtained from the measured cryogen vapor pressure and the centigrade-scale, $\theta(P)$, vapor-pressure equation of Keesom et al. [25]. Absolute temperatures, according to Bartholome [2], were then calculated from the expression $T(\mathrm{K}) = \theta + 273.15$. Clusius and Bartholome fit their results to a Simon-type melting equation. This curve, corrected to the IPTS-68, is seen to lie about 2 bar higher than the present measurements.

Later studies have considerably extended the pressure range for the deuterium melting line. Chester and Dugdale [26] measured n-H_2 and n-D_2 to 2.8 kbar, but their results cannot be used for direct comparison here because the data were expressed only as melting pressure differences between the two isotopes at the same temperature. They observed a nearly constant difference of 167 ± 8 bar between 25 and 57 K.

Further results were reported by Mills and Grilly [27,28] who used a blocked-capillary technique. Their first data set [27], on n-H_2 and n-D_2 only, was limited in pressure to 1.5 kbar because of embrittlement and cracking failures in the measurement apparatus. However, a later, improved system [28] allowed them to measure pressures of n-H_2, n-D_2, and n-T_2 to 3.5 kbar. Their deuterium samples had about the same HD concentration as ours. Below 70 bar, the limit of the present study, they obtained three points which we corrected to IPTS-68 by adding 6 mK to their temperatures. Comparison of these results with eq (3) shows their P_m measurements falling lower than our smooth curve by 0.4 to 0.8 bar. A comparison of the melting curves obtained for n-H_2 and n-D_2 shows a difference of about 170 bar near 20 K.

Goodwin [29] proposed the empirical function

$$(P_m - P_{tp})/(T_m - T_{tp}) = A \exp(-a/T_m) + BT_m + C \quad (5)$$

as a universal equation for the melting lines of the three hydrogen isotopes. For $C = 0$, the constants A, a, and B were fixed from existing normal and *para*-hydrogen melting data. The equation was then applied to n-D_2 and n-T_2 using their respective triple-point parameters, T_{tp} and P_{tp}. Goodwin adjusted the values of C to obtain best fits to the melting data of the two heavy isotopes. At pressures exceeding 100 bar, the function for deuterium was made to agree with the melting equation published by Mills and Grilly [28] to better than 0.5%. Goodwin's equations for n-H_2 and n-D_2 differ in pressure by 169 bar in the 20 K region.

Several years after this work was done, Younglove [30] obtained additional melting data on p-H_2 and found these to be systematically offset from Goodwin's original function [29,31]. At low pressures, Younglove's melting pressures are about 0.4 bar lower than Goodwin's, and at high pressures (ca. 130 bar) they are 1.2 bar lower. It is, therefore, interesting to compare our measurements on n-D_2 with eq (5). In doing so, we find the temperature-corrected [32] form of Goodwin's equation to be about 0.5 to 0.8 bar lower than eq (3). However, the earlier function refers to a triple-point temperature of 18.72 K, which more nearly represents the pure n-D_2 value than does our direct measurement of 18.7067 K. The impurity correction of -0.6 bar discussed above brings the two melting curves into nearly complete correspondence. We suggest that Goodwin's equation describes the melting pressures of pure n-D_2 to about ± 0.2 bar at pressures below 70 bar.

The only other melting curve available is that of Liebenberg et al. [10]. Although the range of validity of this experimental curve extends to 20 kbar, there are large

(≃40 bar) discrepancies in the low-pressure range of present interest.

3.2 Triple-point Temperature

As we have mentioned, the physical significance of T_{tp} in eq (3) is that it represents an empirical triple-point temperature for our sample material. A review and discussion of existing triple-point data for deuterium is presented separately [33].

Most of the earlier triple-point measurements were derived from saturated solid- and liquid-vapor pressure data. With this approach, separate empirical functions are fitted to the data in both solid and liquid temperature regimes. Simultaneous solution of these functions then defines the two triple-point parameters. In general, this technique allows P_{tp} to be fixed with precisions comparable to those of the direct pressure measurements. However, the temperature value at the intersection point is difficult to find closer than about 20 or 30 mK [33]. The greater relative uncertainty in T_{tp} results from the small difference in slope between the solid and liquid vapor pressure functions.

Greater precision for T_{tp} can be obtained with supplementary melting data because the slope of the melting curve is very much larger than that of either the solid or liquid vapor pressure functions. Even with a relatively approximate estimate of the triple-point pressure, the temperature T_{tp} should be determined quite precisely. (For example, an error of 25% in P_{tp} would offset T_{tp} by only about 0.001 K.) By similar argument it is clear that imprecise estimates of T_{tp} taken as fixed parameters in eq (3) should introduce systematic deviations in the residual plot corresponding to figure 3. We examined this effect explicitly and found that significant deviations are apparent in the fitting results for all fixed T_{tp} values that lie outside the range 18.7067 ± 0.002 K.

This value cannot be taken as the triple-point temperature of pure n-D_2 because the HD impurity introduces some offset. Bereznyak et al. [34] published melting diagrams for mixtures of p-H_2/o-D_2, p-H_2/HD, and o-D_2/HD. The melting-temperature function of isotopic concentration for the o-D_2/HD system was found to be nearly linear between the triple points of the two pure elements. It is, therefore, reasonable to assume that a small concentration of HD-impurity c(HD) in otherwise pure n-D_2 will shift the observed triple-point temperature from the pure-component value by an amount

$$\Delta T_{tp} = c(\mathrm{HD})[T_{tp}(\mathrm{HD}) - T_{tp}(\text{n-}D_2)]. \qquad (6)$$

Substituting T_{tp}(HD) = 16.60 K, T_{tp}(n-D_2) = 18.73 K, and c(HD) = 0.0075 into eq (6) yields a temperature shift of $\Delta T_{tp} = -0.016$ K.

There is another possible source of systematic error. We noted earlier that our melting data are actually observations of the "first-freeze" behavior of the material. Grenier and White [35] similarly measured "first-freeze" temperatures of deuterium. But, they also measured melting temperatures of samples that contained larger relative fractions of the solid phase, and for these they reported differences of "a few millikelvin." The effect was attributed to variations of the *ortho-para* compositions of the solid and liquid phases. While this suggestion may be true, we feel the data are insufficient to warrant any firm conclusions. Recall that our direct measurements of the melting curve slope (labeled "3a" in Fig. 2) gave results that are consistent with those derived from the differences of consecutive "first-freeze" melting pressures. In our experiment, the melting characteristics were affected little by the relative phase composition of the sample.

In view of these uncertainties, we feel that a triple-point temperature of 18.723 ± 0.010 K for pure n-D_2 is the most reasonable estimate from our measurements. If this value is used in eq (3), the calculated P_m values will have been corrected for the HD impurity.

3.3 Liquid Isothermal Compressibility

The isothermal compressibility β is calculated from the measured change in the sample pressure ΔP_u that results when the lower chamber pressure is changed by an amount ΔP_l at constant temperature. The expression used in this calculation

$$\beta \equiv -\frac{1}{V}\left(\frac{\partial V}{\partial P}\right)_T = \frac{1}{\bar{V}_u}\left[S_u + S_l\left(1 - \frac{\Delta P_l}{\Delta P_u}\right)\right] \qquad (7)$$

is easily derived from eq (1). In this equation, $\bar{V}_u$ represents the average sample volume for the measurement. For small changes in P_l and P_u, the sensitivity factors S_u and S_l may be taken directly from the calibration curves. However, to obtain more precise compressibilities for the liquid, we chose to measure over larger pressure intervals. This procedure requires the sensitivity parameters in eq (7) to consist of rather complicated weighted averages of the measured S_u and S_l functions.

A plot of the liquid isothermal compressibility measurements along three isotherms is shown in figure 4. The values obtained by extrapolating eight isotherms to the melting curve are represented by circles in the plot. The estimated accuracy is about ±1%.

The functional behavior of these data suggests that we consider a liquid equation of state of the form:

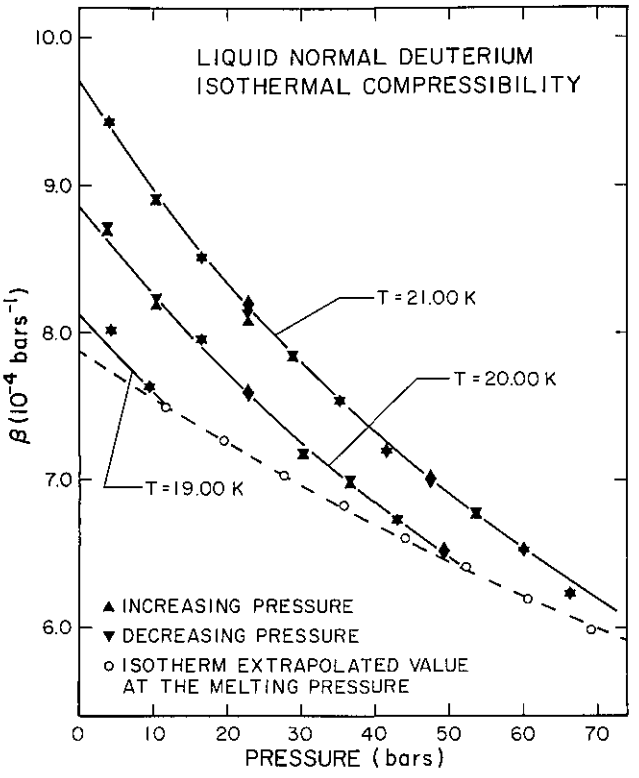

Figure 4—Isothermal compressibility data for liquid n-D_2. Solid curves are isotherms calculated from eq (9) and the fitting constants listed in table 1. The dashed curve represents eq (9) evaluated along the melting line.

$$V(T,P)=V_0(T)[P+P_0(T)]^{-a} \tag{8a}$$

$$V_0(T)=\exp[b_0+b_1(T-T_{tp})+b_2(T-T_{tp})^2 + b_3(T-T_{tp})^3] \tag{8b}$$

$$P_0(T)=c_0+c_1(T-T_{tp})+c_2(T-T_{tp})^2 \tag{8c}$$

where $T_{tp}=18.7067$ K, and a and the subscripted letters b and c are all constants to be determined by fitting eq (8) and their derivative functions to the experimental data.

For the isothermal compressibility, we obtain the following relationship:

$$\beta(T,P)\equiv-\left(\frac{\partial \ln V}{\partial P}\right)_T=\frac{a}{P+P_0(T)}. \tag{9}$$

A fit of eq (9) to the compressibility data gives the numerical values for the constants a, c_0, c_1, and c_2 listed in table 2. In figure 4, the smooth curves depicted for three isotherms and the liquid compressibility along the melting line were calculated from eq (9) and these constant values.

To our knowledge, there are no published compressibility data in this temperature and pressure range that could be used for direct comparison. But, there have been several measurements of liquid molar volume at pressure and some estimates of compressibilities can be calculated from these by taking first differences. Bartholome [2] published volume data along three isotherms between 19.5 K and 21.0 K. Compressibilities obtained from Bartholome's raw data are too scattered to allow any meaningful comparison, but those calculated from his smooth curves show qualitatively correct pressure and temperature dependences. Quantitatively, the agreement with our results is less satisfactory; compressibilities derived from the earlier work typically lie 10 to 14% higher than those calculated from eq (9).

Table 2. Coefficients to eqs (8), (9), and (11) that describe the equation of state for the liquid.

$a=0.12$	$c_0=152.0$
$b_0=3.7408$	$c_1=-13.2$
$b_1=0.0017$	$c_2=0.50$
$b_2=0.00028$	
$b_3=0.00001$	

Friedman et al.[6] published molar volume data for liquid normal deuterium at seven temperatures between 20.3 and 38.0 K and at pressures to 100 bar. Their volume measurements along the 20.33 K and 20.31 K isotherms were shown to agree reasonably well with the earlier but less precise Bartholome [2] data. Compressibilities derived from the Friedman 20.33 K data are in ±1% agreement with values found from eq (9). Those calculated from their isotherms at 20.31 K and 23.52 K scatter about our fitted smooth curves with an average absolute deviation of about 6% and 4%, respectively.

3.4 Liquid Thermal Expansivity

The isobaric thermal expansion coefficient α is calculated from the measured change in the lower-cell pressure ΔP_l that is required to maintain a constant sample pressure P_u when the temperature of the system is changed by an amount ΔT. From eq (1) it follows that

$$\alpha\equiv\frac{1}{V}\left(\frac{\partial V}{\partial T}\right)_P=-\frac{S_l\Delta P_l}{\bar{V}_u\,\Delta T}-\frac{S_u}{\bar{V}_u}\left(\frac{dP_b}{dT}\right) \tag{10}$$

where $\bar{V}_u$ is again the average sample volume for the measurement, and dP_b/dT is the temperature derivative of the liquid p-H_2 vapor pressure calculated from eq (2).

Figure 5 is a plot of the liquid expansion data obtained at six different pressures. We estimate the experimental uncertainty for these measurements to be about ±1 or 2%. The data precision was limited to some extent by the temperature measurements but mostly by a slight

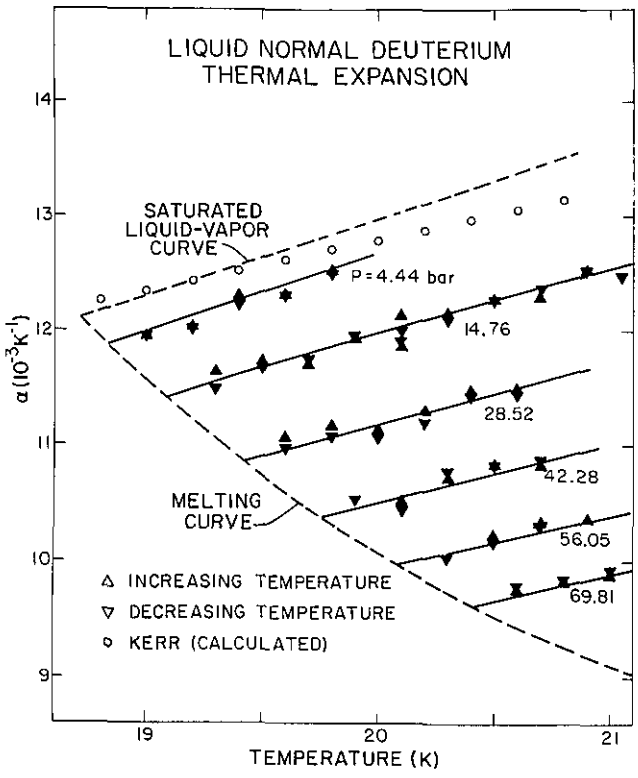

Figure 5—Thermal expansion data for liquid n-D_2. Solid curves were calculated from eq (11) and the fitting constants listed in table 1. The dashed curve represents eq (11) evaluated at saturated liquid-vapor pressures and melting as indicated. Open circles are calculated values from the fitted equation by Kerr [5].

nonlinearity in the pressure readout of the TI-144 bourdon gauge used for measuring P_l. Occasionally some hysteresis effects were observed in the deflection of the cell diaphragm although these only occurred for the initial points in either warming or cooling series of measurements. Errors of about 6% were observed for such artifacts, and these few data were discarded.

Differentiation of eq (8) yields the following expression for the thermal expansivity:

$$\alpha(T,P)=b_1+2b_2(T-T_{tp})+3b_3(T-T_{tp})^2 \\ -\beta(T,P)[c_1+2c_2(T-T_{tp})] \qquad (11)$$

where $T_{tp}=18.7067$ and $\beta(T,P)$ is calculated from eq (9). The constants a and the subscripted c's are those determined from the compressibility measurements. These constraints assure that the identity

$$\left(\frac{\partial\alpha}{\partial P}\right)_T \equiv -\left(\frac{\partial\beta}{\partial T}\right)_P \qquad (12)$$

holds and, thereby, provide a condition of internal consistency that is automatically met if the expansivities can be fitted to eq (11) by adjusting only b_1, b_2 and b_3.

Equation (11) was fitted to the thermal expansivity data to fix the values in table 2 for the three additional constants. Smooth curves corresponding to the pressures of the six experimental isobars were calculated from eq (11) and are plotted with the data. The dashed lines in figure 5 represent the values along the vapor-pressure and melting curves as indicated.

As before with the compressibilities, we found our thermal expansivity measurements to be the only explicit data in this range. Here again, we have derived estimates from the smooth curves that were fitted to independent measurements of the molar volume [2,5].

Kerr [5] measured the molar volume of the liquid along the vapor pressure curve. He combined his results with those of Clusius and Bartholome [1] and fitted them to a quadratic function of temperature. We calculated thermal expansion coefficients from this function by differentiation. The slight correction to constant pressure was made with eq (9) and Grilly's [23] vapor pressure function. The results of this calculation, included in figure 5 as the series of open circles, agree reasonably well with eq (11) near 19 K but deviate systematically with temperature to more than 2% at 20.5 K.

Bartholome [2] presented measurements of the liquid molar volume as a function of pressure along three isotherms. Again, we consider the smooth curves that he fit to his raw data. The differences between these isotherms at constant pressure were taken to calculate average thermal expansivities in the two temperature intervals. At low pressures there is satisfactory agreement with our data. (Here, the consistency is reasonable if it is recalled that Bartholome calibrated the volume of his pressure cell along the vapor curve against the molar volume data of Clusius and Bartholome. The latter measurements were included by Kerr [5] in his quadratic fit, and thermal expansion coefficients derived from this function were shown to correspond closely to our extrapolated measurements.) However, with increasing pressure, the average thermal expansion coefficients calculated from Bartholome's data decrease much more rapidly than ours do. At 70 bars they fall to about 50% of our results.

3.5 Liquid Molar Volume

Data for V_{lm}, the liquid molar volume along the melting curve, were obtained by a two-step operation. First, the volume of a sealed liquid sample was measured at a given temperature and two-phase pressure P_u. The sample quantity was then determined by expanding the gas into a standard volume at room temperature. The latter measurement followed essentially the same procedure

as that used for the calibration measurements of the cell volume and pressure-sensitivity factors.

The results are listed in table 3. We estimate their accuracy and precision to be about ±0.035 and ±0.003 cm³/mole, respectively. For all of the measurements except one, the data were taken within about 6 h from the time of the sample loading. The point at $T_m = 19.000_8$ K was obtained from a sample that had been loaded and held at that temperature for approximately 17 h before the measurement.

The results are plotted together as a function of temperature in figure 6. Also included in the figure are three points that Woolley et al. [4] had compiled from earlier work [1,2]. The liquid molar volume measurements of

Table 3. Measured liquid molar volumes along the melting curve.

T_m(K)	V_{lm}(cm³/mole)
18.830_8	23.00_4
19.000_8	22.93_0
19.201_0	22.84_6
19.403_0	22.76_4
19.604_3	22.68_4
19.805_5	22.60_5
20.008_0	22.53_2
20.204_5	22.45_6
20.408_5	22.38_6

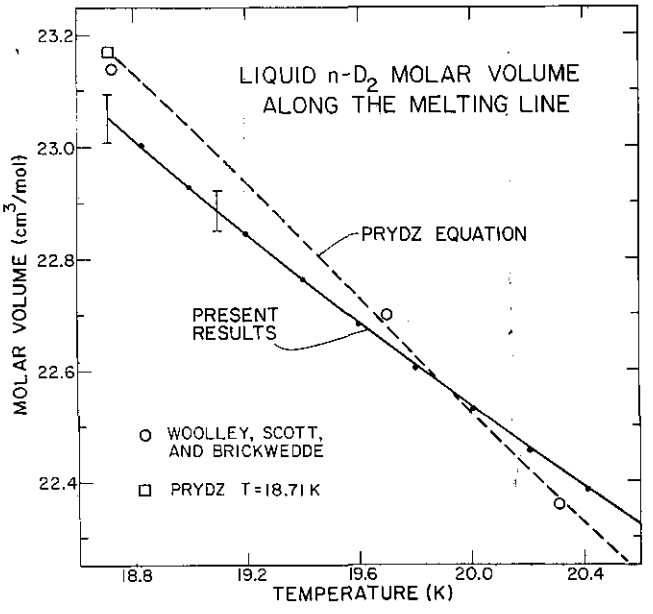

Figure 6—Measurements of the molar volume of liquid n-D_2 at melting. The solid curve was calculated from eq (8) at the temperatures and pressures prescribed by eq (3). A ±0.15% error is indicated for these results. The liquid density function of Prydz [7] was evaluated at the same points and the results are represented in the plot by the dashed curve. Also included are three points that were tabulated by Woolley et al. [4].

Bartholome were discussed in the two previous sections. To obtain the points at 19.70 and 20.31 K, Woolley evaluated Bartholome's smoothed functions at the temperatures and pressures prescribed by the melting curve of Clusius and Bartholome [1]. The triple-point value, 23.14 cm³/mole, was taken directly from the work of Clusius and Bartholome [1].

Prydz [7] used these and other earlier data to fit an equation of state for liquid normal deuterium. We evaluated the Prydz density function at temperatures and pressures corresponding to our observed melting line. The resulting curve, which is also plotted in figure 6, adequately represents the earlier data. However, our measurements indicate that the liquid compression along the melting curve is not nearly as great as the Prydz function would suggest.

The liquid molar volume data were taken with the parameters a, b_1, b_2, b_3, c_0, c_1, and c_2 in table 2 to fix the remaining constant b_0. With the full set of fitting parameters, eq (8) can be used to calculate liquid n-D_2 molar volumes for any temperature and pressure within or even somewhat beyond the ranges of the measurements. The curve depicted in figure 6 was calculated along the melting line defined by eq (3). The average absolute deviation of the measured data from the calculated curve is 0.0026 cm³/mole, which is comparable to the estimated precision of the measurements.

We have shown in this and in the two preceding sections that the isothermal compressibility, thermal expansion, and molar volume data for the liquid are all well described by a single empirical equation of state. This is a sufficient demonstration of the internal consistency of these measurements. It remains now to compare the predictions of this equation with independent data, but first some comment should be given about the effects of sample contamination.

Our volume data and their representation, eq (8), were presented without any correction for impurity effects. The choice is somewhat arbitrary as to whether or not these should be formally included. Some of the existing data were given as corrected values [5,36], but others [1,2,6] were published without corrections as we have done. The effects are not entirely negligible. For our case, the only significant impurity was the 0.75% HD discussed above. If we assume the volume correction is proportional to the HD concentration and to the difference between the molar volumes of HD and D_2, we have

$$\Delta V_l = c(\mathrm{HD})\,[V_l(\mathrm{HD}) - V_l(\text{n-}D_2)]. \qquad (13)$$

The most recent density measurements on HD are those of Rudenko and Slyusar' [37], which extend from 16.6 to 35.5 K along the vapor curve. These data, combined

with extrapolated values from eq (8), yield a volume difference of about 2 cm^3/mole. The correction to eq (8) is then toward smaller values by an amount 0.015 cm^3/mole. With the possible exception of some of the earliest work [1,2], the extent of impurity effects in previous data is comparable to that estimated for our own.

Bartholome [2] published the earliest measurements of the molar volume of n-D_2 at pressure. Bartholome's raw data scatter about the fitted smooth curves with an average absolute deviation of 0.025 cm^3/mole. The precision of these measurements is, therefore, roughly an order of magnitude less than that typical of more recent work [5,6]. The average absolute deviation of Bartholome's data from eq (8) is 0.073, 0.035 and 0.058 cm^3/mole for the isotherms at 19.723, 20.346 and 21.032 K (IPTS-68), respectively. Although these differences are probably no larger than the combined error for the two experiments, the earlier data show significant systematic deviations from eq (8). As has been mentioned the compressibilities derived from Bartholome's work are larger than our measurements by 10 and 14% at $T=20.346$ and 21.032 K (IPTS-68), respectively. The discrepancies may be the result of sample contamination which we shall discuss later in more detail.

The later measurements by Friedman et al. [6] provide us with a more critical basis for comparison. Of particular interest here are their tabulated results along the isotherms at 20.31 and 20.33 K. We plotted these two sets of volume data as functions of pressure and found them to agree nearly identically. To compare these with our results, we next included the corresponding isotherm calculated from eq (8). The plot of the calculated values parallels the Friedman measurements but is uniformly lower in magnitude by about 0.05 cm^3/mole. This discrepancy is larger than our estimated error but probably smaller than the combined experimental uncertainties. Although Friedman et al. gave no explicit error limits, an accuracy comparable to our own (± 0.035 cm^3/mole) is reasonable. With this assumption the combined error is ± 0.07 cm^3/mole, and their volume measurements at 20.3 K are shown to agree with our equation of state. A similar comparison was made with their data at 23.52 K. At this higher temperature, the difference between the earlier measurements and the values calculated from eq (8) is no greater than 0.035 cm^3/mole throughout the entire pressure range.

The Friedman data were presented without any explicit impurity corrections although the authors gave an impurity level of 0.2 at % hydrogen (equivalent to 0.4% HD), roughly half the HD-concentration of our samples. This result seems improbable because most available deuterium has the same impurity as our sample, and they apparently made no special effort to purify their material. Ultimately, the accuracy of their impurity analysis (whether they had 0.4 or 0.8% HD) does not change the overall conclusion. The correspondence between their data and ours is not significantly affected by differences in contamination levels.

In a previous section, we mentioned that independent measurements of the liquid volume are available along the vapor pressure curve. These should provide useful comparisons, but because our lowest working pressures were between 4 and 5 bar, it is necessary to extrapolate our results somewhat. To do this, we calculated a molar-volume function of temperature by combining Grilly's [23] vapor-pressure equation for liquid n-D_2 with eq (8). A plot of this curve is shown in figure 7. Also included are the values Clusius and Bartholome [1] reported in the range 18.80 to 20.53 K, the measurements Kerr [5] made between 19.5 and 24.5 K, and the values found by extrapolating the data of Bartholome [2] to the vapor

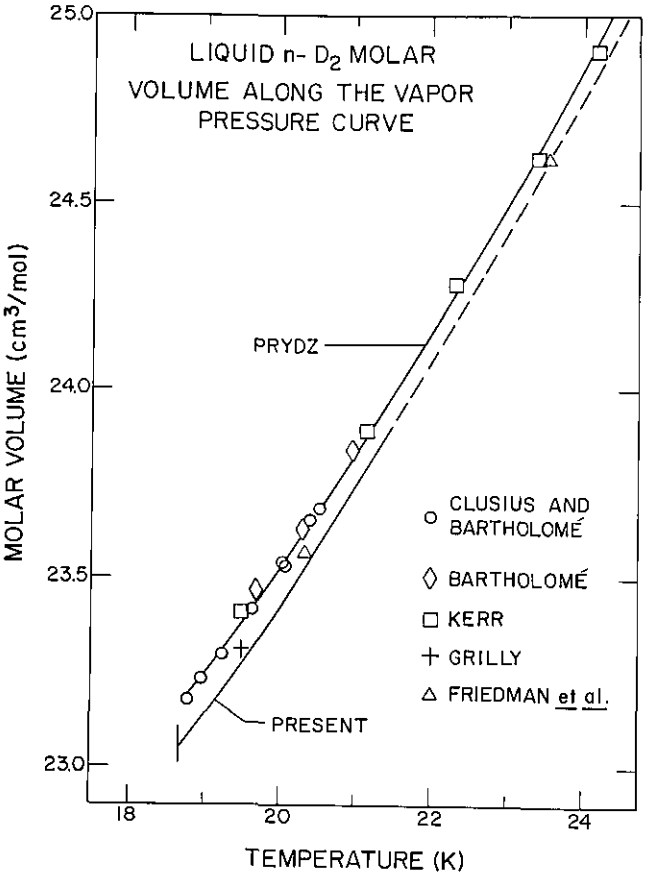

Figure 7—Existing molar volume data for liquid n-D_2 along the saturated vapor pressure curve. Direct measurements by Clusius and Bartholome [1], Grilly [36], and Kerr [5] are included with extrapolated values from the data of Bartholome [2] and Friedman et al. [6]. The solid curve through these data was calculated from the liquid equation of state of Prydz [7]. The lower curve was calculated from eq (8). The dashed portion represents an extrapolation beyond our measured temperature range.

pressure curve. As figure 7 illustrates, these results are well described by the Prydz equation. However, throughout the plotted range, the earlier values are all consistently larger than those extrapolated from this work. In the interval 18.7 to 20.4 K, the offset is approximately 0.5%. About midway between the two curves are the extrapolated values from the data of Friedman et al. [6] and the direct measurement at 19.48 K by Grilly [36].

If each research had ±0.15%uncertainty, our results agree with [6] and [36] but not with the others. The most serious discrepancy appears to be that between Kerr's data and ours. Kerr published five measurements of the molar volume between 19.5 and 24.2 K. His results at 19.51 and 21.14 K are larger than corresponding values calculated from eq (8) by 0.13 and 0.10 cm^3/mole, respectively. Kerr stated that a mass spectrometric analysis of the sample showed it to contain 0.4 at % hydrogen (equivalent to 0.8% HD) as the only detectable impurity. He corrected the data for impurities in the manner described above. If we compare our corrected data to his, the differences appear to be as large as 0.12 to 0.15 cm^3/mole. No error limits were quoted for the results Kerr presented, but if we assume an accuracy of ±0.15%, these data remain in substantial disagreement with our calculated values.

The source of the large discrepancy is not clear. We considered the possibility that some systematic error may have arisen from either of the volume calibrations at low temperature. Kerr calibrated his pycnometer with "pure hydrogen" and the data of Scott and Brickwedde [38]. On this point Kerr's report is somewhat ambiguous because Scott and Brickwedde included measurements on both liquid normal and *para* hydrogen. However, both sets of these earlier data extend along the saturated vapor pressure curve from 14 to 20.4 K. They were obtained with the same experimental apparatus and, except for sample preparation, by the same procedure. We may reasonably assume that they are internally consistent. Therefore, regardless of the form of hydrogen that Kerr used, we can check his calibration against our own by comparing the respective p-H_2 density standards.

It was not necessary for us to do this explicitly because Roder et al. [39] made this very comparison only a short time after the Goodwin data were published. To do this, Roder first fitted the Goodwin data to low-order polynomial expansions to represent both isotherms and isochores of the liquid density. These smoothed functions were then extrapolated to the saturated liquid-vapor pressure curve reported by Weber et al. [40]. Roder finally combined these "derived" data in the range 17.0 to 33.0 K with the Scott and Brickwedde measurements and fitted the set to a single analytic function. They showed that deviations from the fitting function were of the same magnitude as the expected error of the data. This overall consistency is taken to establish the correspondence between our own volume calibration and that of Kerr's research. Whatever the source of the discrepancy is in the deuterium measurements, it does not arise from any disparity in the hydrogen densities used for the calibrations of the low-temperature sample volumes.

It would appear from figure 7 that Kerr's data agree with those of Clusius and Bartholome [1] and Bartholome [2]. The average deviation of the Clusius and Bartholome results from our extrapolated function is 0.10 cm^3/mole. But, there are several reasons to suspect that these earlier data are too large by roughly 0.05 cm^3/mole. The molar volume measurements that Clusius and Bartholome made were only part of a rather comprehensive thermodynamic study. In addition to these data and among others, they included measurements of the triple-point and, at one temperature, the saturated liquid-vapor pressure. This information is useful because the most likely occurring sample contaminants in the earlier work on deuterium are H_2 and HD [33]. It is known that both impurities tend simultaneously to increase measured vapor pressures and to depress observed triple-point temperatures. From the results of these additional measurements it is argued [33] that the sample lot of deuterium used by Clusius and Bartholome was contaminated to higher levels than were judged in their report. Estimates of either 1.0% H_2 or 2.6% HD are proposed to explain the observed offsets in their results for the vapor pressure and triple-point temperature. In either case, the corresponding values for ΔV_l calculated from eq (13) are approximately 0.05 cm^3/mole.

In the later high-pressure experiment [2], Bartholome calibrated the volume of his cell with both liquid hydrogen and liquid deuterium. Absolute volumes were calculated from the measured mole contents by using the density data of Onnes and Crommelin [42] for hydrogen and Clusius and Bartholome [1] for deuterium. The results obtained from the two calibrations reportedly agree to within 0.03%. This is interesting because the Onnes and Crommelin data are known now to be high by about 0.05 cm^3/mole [38]; the agreement suggests that the deuterium results of Clusius and Bartholome (and Bartholome [2]) are also high by the same amount. The discrepancy is exactly that estimated above from considerations of impurity effects. If the Clusius and Bartholome data are corrected for this suspected contaminant, their measurements are seen to agree almost identically with the direct measurement of Grilly [36]

and also with the extrapolated data of Friedman et al. [6]. For the Clusius and Bartholome measurements, an error limit of ± 0.04 cm^3/mole is not an unreasonable estimate, given the combined uncertainties of the data and the impurity correction. If this limit is assumed, their results are seen to be consistent with our own data even after the 0.015 cm^3/mole impurity correction is applied to the latter.

To summarize this discussion, we have examined several series of measurements of the molar volume of liquid n-D_2. Some of these were direct measurements along the saturated liquid-vapor pressure curve [1,5,36] while others were made along isotherms at pressure [2,6]. The individual results were compared directly when possible and by extrapolation when not. Generally, the values prescribed by our equation of state are lower than those obtained from earlier measurements. Comparisons with independent measurements of the molar volume show our work to be consistent with that of Friedman et al. [6], which are the more precise of the existing data at pressure. At the vapor-pressure line, we find that our extrapolations are consistent with the data of Clusius and Bartholome [1] if these are corrected for a substantial impurity effect. However, there is a significant difference between the molar volume measurements of Kerr [5] and corresponding values calculated from our equation of state. We examined the possibility that some error may have arisen from inconsistencies in the hydrogen density data used as standards in the volume calibrations, but we were unable to substantiate this hypothesis. The source of the discrepancy between Kerr's results and ours is unknown.

3.6 Other Related Data

Most of the previous discussion has involved direct comparisons of our data with those of others. There are also indirect data comparisons worth considering. One quantity that is often discussed is the isochoric temperature derivative of the pressure, $(\partial P/\partial T)_v$. An analytic form for $(\partial P/\partial T)_v$ can be derived in either of two ways: eq (8a) can be inverted to express the pressure as a function of temperature and volume, and the desired function is obtained by differentiation. Or, the result can be calculated directly from the identity

$$\left(\frac{\partial P}{\partial T}\right)_v = \frac{\alpha}{\beta} \tag{14}$$

and eqs (9) and (11). In either case, we estimate an uncertainty of $\pm 2\%$ for this calculated quantity.

In figure 8, we have plotted $(\partial P/\partial T)_v$ for our liquid data along the melting curve as a function of temperature. For comparison, we have also included results calculated at the same temperatures and pressures from the $(\partial P/\partial T)_\rho$ function given by Prydz [7]. The curves show two obvious dissimilarities. First, they differ in magnitude by approximately 20%. Second, the Prydz function shows a large positive curvature, whereas our $(\partial P/\partial T)_v$ results are more nearly constant with only a slight positive slope and curvature. The magnitude and functional behavior of our $(\partial P/\partial T)_v$ is consistent with that deduced by Friedman et al. [6] from their liquid PVT measurements. In particular, they found their data best described by the reciprocal volume relationship

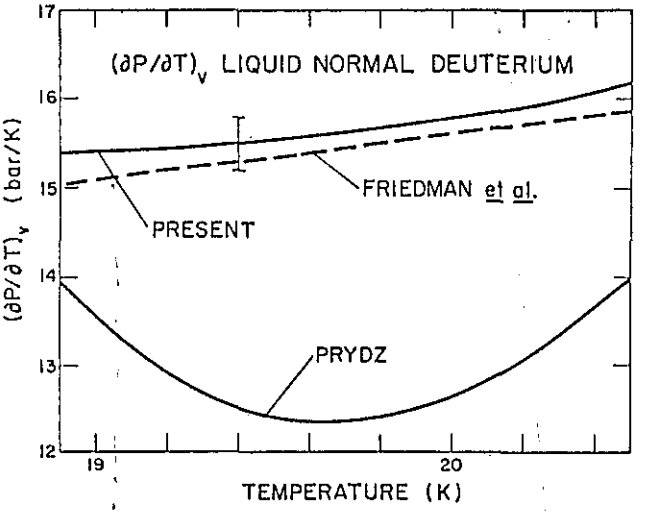

Figure 8—Plot of $(\partial P/\partial T)_v$ for liquid n-D_2 along the melting line defined by eq (3). The upper solid curve was calculated from eq (14). The dashed curve was calculated from eq (15). The lower solid curve represents the empirical function for $(\partial P/\partial T)_\rho$ given by Prydz [7].

$$\left(\frac{\partial P}{\partial T}\right)_v = -14.3 + \frac{674}{V_l} \tag{15}$$

where the molar volume V_l is taken in cm^3/mole and $(\partial P/\partial T)_v$ is given in bar/K. In figure 8, we have plotted the results obtained from eq (15) with the liquid molar volume data in table 3.

Thus far, we have only discussed equation-of-state data although these alone are not sufficient to describe the thermodynamic properties of a system. Supplementary thermal data are necessary for complete information. In connection with the present work, it is, therefore, interesting to briefly review the existing calorimetric data.

The earliest specific heat measurements on liquid n-D_2 were published by Clusius and Bartholome [1]. Their data, over the temperature range 19.4 to 21.7 K, were later found to be about 8% lower than those of subsequent measurements [35,43]. Kerr et al. [43] con-

cluded that some systematic error may have affected the earliest liquid results. Today, the liquid heat capacities of Clusius and Bartholome remain a matter of historic interest but are no longer given as preferred data [44].

Subsequent calorimetric measurements were reported by Kerr et al. [43] on o-D_2 (2.2% *para*) in the range 19.9 to 22.8 K and by Grenier and White [35] on 78.6% *para* at three temperatures between 19.9 and 22.1 K. The results of these two experiments agree to within 1 or 2%. Grenier and White considered this discrepancy reasonable in view of the uncertainties involved in the independent investigations. They further concluded that any effects of *ortho-para* composition are negligible in this temperature and pressure range.

Still later, Brouwer et al. [45] measured the specific heat of liquid n-D_2 as part of an extended study of the liquid phase separation properties of the n-D_2/Ne binary system. Their results for pure n-D_2 apparently extend over the entire range 20 to 30 K because they present a difference plot of the raw data from a fitted smooth curve. Curiously, Brouwer et al. did not explicitly include the analytic function in their publication, although they did tabulate values that were calculated from it at 0.2 K intervals between 24.0 and 27.4 K.

In each of these four experiments, the actual measured quantity is the heat capacity along the saturated vapor pressure curve, which we denote as C_{sat}. From these data, the familiar isobaric quantity C_p can be derived from the relationship:

$$C_p = C_{sat} + T\left(\frac{\partial V}{\partial T}\right)_P \left(\frac{dP}{dT}\right)_{vp} \tag{16}$$

where $(dP/dT)_{vp}$ is the slope of the vapor pressure curve. The second term in eq (16) may be calculated from eqs (8a) and (11) and the temperature derivative of Grilly's [23] saturated liquid-vapor pressure function.

For temperatures below about 23 K, the second term in eq (16) contributes less than 1% and could be neglected, but at higher temperatures there is a significant difference between C_p and C_{sat}. We, therefore, calculated C_p explicitly for each of the later sets of measurements discussed above [35,43,45]. The results were then fitted to a quadratic function to yield

$$C_p(T,P_{vp}) = 22.16 + 0.73(T-18.73) + 0.044(T-18.73)^2. \tag{17}$$

We find that eq (17) reproduces the "corrected" Brouwer et al. [45] tabulated data to well within 1%. The C_p values corresponding to the Kerr et al. [43] measurements likewise fall in this range except, perhaps, for the highest temperature result, which may be lower by slightly more than 1%. However, at roughly this same temperature, the Grenier and White [35] measurement is seen to fall about 2% higher than the smooth curve. We, therefore, postulate that eq (17) describes to within ±1% the isobaric heat capacity for the liquid along the saturated vapor pressure curve from the triple point to 27 K.

Corresponding values at higher pressures are calculated from

$$C_p(T,P) = C_p(T,P_{vp}) - \int_{P_{vp}}^{P} (\partial^2 V/\partial T^2)_P \, dP \tag{18}$$

where a closed-form expression for the second term is derived from eq (8). Equation (18) illustrates that the qualitative effect of increasing pressure is to decrease C_p. For example, at $T = 20.4$ K and $P = 70$ bar, the calculated heat capacity is about 9% lower than its value at the same temperature on the vapor curve.

There are no independent measurements of C_p at pressure that could be checked against eq (18) directly, but there are data for C_V, the specific heat at constant volume. Bartholome and Eucken [3] measured C_V for liquid n-D_2 in the temperature range 19.5 to 23.5 K. In principle, these results could be compared with C_{sat} and our equation of state by calculating

$$C_V(T,P) = C_p(T,P) - T\,V(T,P)\,\frac{\alpha^2(T,P)}{\beta(T,P)} \tag{19}$$

where the first term on the right-hand-side is obtained from eqs (17) and (18) and the second from eqs (8a), (9), and (11).

There is, unfortunately, some ambiguity in the interpretation of the earlier results. To understand this, it is helpful to think of C_V in terms of temperature and molar volume as the independent variables. The difficulty is then clear because Bartholome and Eucken did not explicitly include the sample density along with their temperature and specific-heat measurements. From the reported volume of the sample chamber (3.5 cm^3) and the amount of material used for the liquid measurements (0.171 moles), we might infer the value $V_1 = 20.47$ cm^3/mole, but at this density we see from figure 6 that a sample could not exist in the liquid state over much of the quoted temperature range. We observe from eqs (3) and (8) that at 19.65 K the liquid molar volume must assume some value between 22.655 cm^3/mole at the melting line and 23.310 cm^3/mole at the saturated liquid-vapor pressure.

Despite this ambiguity, there is some useful information available. The measurements of Bartholome and Eucken [3] are plotted in figure 9. If we assume these

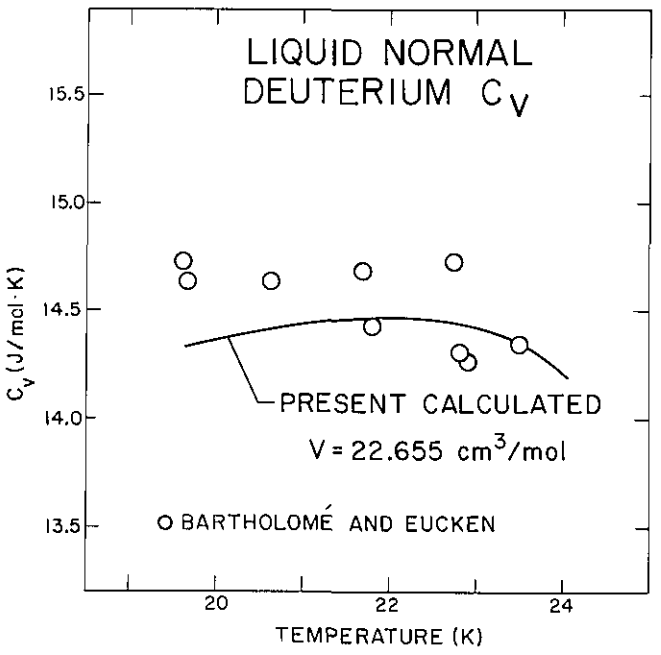

Figure 9—The isochoric heat capacity data of Bartholome and Eucken [3]. The solid curve was calculated from eq (19) for the liquid density at 19.65 K on the melting line.

data were terminated by the onset of freezing at 19.65 K, a sample volume of 22.655 cm^3/mole is implied. The solid line plotted in figure 9 is the C_V curve prescribed by eq (19) for this molar volume.

The calculated curve agrees reasonably well with the direct measurements. In the range 19.7 to 21.0 K the heat capacity results are reproduced to within 5%. At higher temperatures the curve follows the measurements and seems to corroborate the observed weak temperature dependence that Bartholome and Eucken observed in deuterium. This agreement is somewhat fortuitous, however. The slope and curvature of the function defined by eq (19) is very sensitive to the values chosen for b_2 and b_3 in eq (11), much more so than are the results obtained from fitting our data. Below about 20 K the calculated C_V remains little affected by the choice of these two parameters, but at temperatures near 24 K, the results can vary by as much as 20%.

Finally, we compare experimentally measured sound velocities in the liquid with those calculated from

$$\frac{1}{u^2}=M\left(\frac{\beta(T,P)}{V(T,P)}-\frac{T\,\alpha^2(T,P)}{C_P(T,P)}\right) \qquad (20)$$

where $M=4.0282$ gm/mole is the molecular weight of deuterium, and u is the longitudinal sound velocity. The term in parentheses is calculated from eqs (8a), (9), (11), (17), and (18).

Bezuglyi and Minyafaev [46] published the first ultrasound velocity measurements on liquid n-D_2. Their results along the vapor curve at $T=19$ and 20 K are plotted in figure 10. Subsequent measurements by Wanner and Meyer [47] extend from the triple point both along the melting line to about 24 K and along the saturated-vapor-pressure curve to nearly 26 K. Data from the lower portion of their measured temperature ranges are included in the plot. Typical error limits for these experiments are 0.5 to 1.0%.

To compare with these direct measurements, we have included the results calculated from eq (20) and our own data. Sound velocities corresponding to our measured temperature range are indicated in figure 10 by the solid line segments. The dashed portions represent calculated

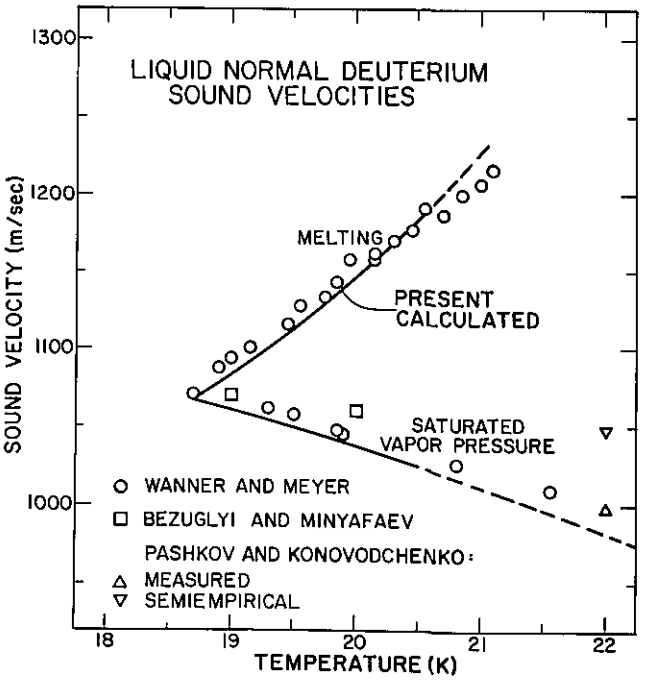

Figure 10—Liquid sound velocity measurements by Bezuglyi and Minyafaev [46], Wanner and Meyer [47], and Pashkov and Konovodchenko [48]. Also included in the plot is the semiempirical result that [48] derived from multistructure theory and the data of Prydz et al. [8]. Equation (20) was evaluated both along the saturated vapor pressure curve and at melting. The solid lines represent these results in the temperature range of the present experiment. Extrapolations of eq (20) are shown as the dashed portions.

values in the extrapolated regions. We estimate roughly ±2% uncertainties for these results. In the range below 20.5 K, the experimental measurements and the calculated curves agree. There is even a reasonable correspondence among the results along the vapor curve as high as 22 K. However, along the melting line in the extrapolated range above 20.5 K there is a significant divergence. This discrepancy may indicate a systematic

error in our measurements, but it may also be an artifact introduced by the particular functional form chosen to represent our equation of state.

Finally, we mention the work of Pashkov and Konovodchenko [48] who measured sound velocities at three temperatures: 22.00, 26.00, and 29.00 K. At 22.00 K they obtained 998.8, 1105.0, and 1195.8 m/sec at pressures of 0.605, 50.66, and 101.33 bar, respectively. Corresponding velocities calculated from eq (20) are 983, 1114, and 1241 m/sec, respectively. At the two lower pressures there is satisfactory agreement between the measured and calculated values, but at 101.33 bar the difference is nearly 4% and is in the same sense as the divergence indicated at high temperatures along the melting line.

3.7 Volume Change on Melting Heat of Fusion, and Solid Molar Volume

The volume change on melting (freezing) ΔV_m was measured by sealing the sample chamber with liquid n-D_2. At constant temperature, the lower cell chamber was first pressurized to freeze the sample and then depressurized to melt it. The volumes of the solid and liquid at the melting pressure were determined quite precisely from the abrupt slope discontinuities in P_u as observed in the calibrated capacitance measurements. The results presented in table 4 are expressed as $\Delta V_m/V_{lm}$, the volume change normalized to the liquid molar volume at the melting pressure. An uncertainty of about ± 0.0005 is estimated for these data.

Equation (8) was used to calculate ΔV_m, the absolute volume changes. The results are plotted in figure 11 together with the single value, 2.66 cm^3/mole, that Clusius and Bartholome [1] quoted for the triple point. Bartholome [2] published the only other direct measurements at these temperatures. His average values, 2.16 and 1.98 cm^3/mole at 20.31 and 20.97 K respectively, are much smaller than our data. The ΔV_m measurements by Liebenberg et al. [10] were carried out in a much higher range, 75 to 164 K. The results were

Table 4. Measured volume changes on melting (freezing).

T_m(K)	$\Delta V_m/V_{lm}$(freezing)	$\Delta V_m/V_{lm}$(melting)
18.83	0.1171	0.1171
19.00	0.1156	0.1156
19.20	0.1144	0.1146
19.40	0.1128	0.1131
19.60	0.1120	0.1121
19.80	0.1111	0.1112
20.00	0.1099	0.1102
20.20	0.1090	0.1091
20.40	0.1078	0.1081

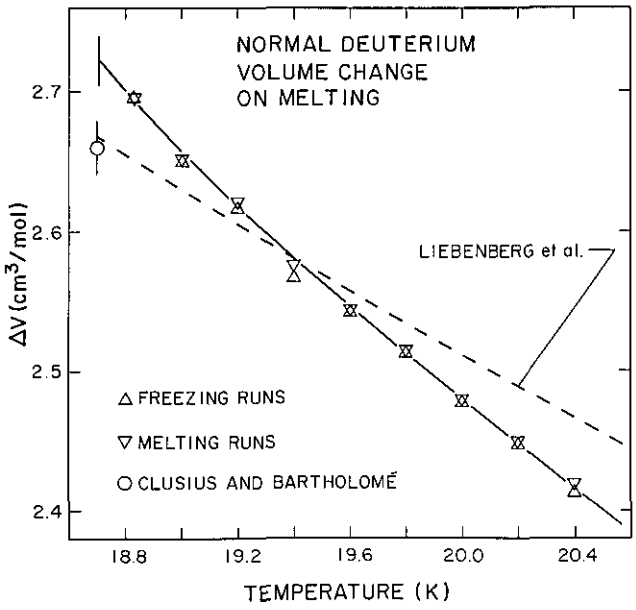

Figure 11—Measurements of the volume changes on melting. Included with these is the triple-point value derived by Clusius and Bartholome [1] from their measurement of the heat of fusion. The dashed line is an extrapolation of the empirical function given by Liebenberg et al. [10] to represent their high-temperature data.

fitted to an empirical function of temperature. The dashed curve in figure 11 represents this function extrapolated to the triple-point region. The agreement between Liebenberg's extrapolation and the Clusius-Bartholome measurement is fortuitious.

The data presented here are relevant to some interesting questions first raised more than a decade ago. In 1973, Roder [49] speculated that hydrogen may exhibit a solid phase transformation near the melting curve at some temperature between 15 and 26 K. The suggestion was made as an attempt to explain certain anomalies observed in solid molar volume [50] and heat capacity data. Independent measurements of the polarizibility [30,51,52] and sound velocity [46,47] in the solid phase also showed inconsistencies that seemed to corroborate his hypothesis.

At the same time that Roder's work appeared, Manzhelii et al. [53,54] found that solid hydrogen undergoes an abrupt, but reversible, increase in density with increasing temperature at about 14 K and 30 bar. They attributed the effect to a solid phase transition. For a time, the proposed explanation drew some criticism [13,14], but supporting evidence was later obtained from detailed measurements of the hydrogen melting line [24]. A small cusp-like singularity was observed near 14 K and interpreted as the intersection point of the solid-solid phase line. Mills [55] concluded that the equilibrium line of the solid hydrogen transformation must

have negative slope, but the structure of the high-temperature form is still uncertain. X-ray diffraction studies at 16 K and 100 bar [56] suggest the change may be to an fcc structure, but the possibility of an isomorphic hcp transformation has not been dismissed entirely [24].

Our volume-change measurements are relevant in this context because the solid phase transition is apparently not limited to pure p-H_2 alone. Manzhelii et al. [54] and Bereznyak and Sheinina [24] discovered that the phenomenon is independent of the *ortho-para* concentration of hydrogen. Observed irregularities in the melting line of e-D_2 [24] further suggest that similar transformations may be characteristic of the heavier isotopes as well. The effect is apparently also present in hydrogen-helium mixtures [57]. It is, therefore, reasonable to expect some indication of a solid phase transformation in the melting properties of n-D_2. Yet, as we mentioned earlier, there are no anomalies observed in our measurements of the melting curve. Nor do we observe any jump-like singularities in the data for the volume change on melting.

Manzhelii et al. [53,54] measured a density discontinuity of 0.15% in solid hydrogen. If a comparable difference in density were present between two solid phases of n-D_2, we would expect to see a step in the curve representing our results in figure 11. The high-temperature solid phase should, by analogy, be more dense. The volume change from the liquid would be greater, and the step would be positive with increasing temperature. The discontinuity would occur at about 19 K and be about 0.0 3 cm^3/mole in magnitude. There is no obvious indication of such a step discontinuity in figure 11. Although it could be that the precision and density of our data are not sufficient to resolve the effect, it is difficult to dismiss the observed regularity of the melting pressure measurements. Our result does not directly contradict any existing data. At this time there is no evidence for a solid-solid phase transformation in solid n-D_2.

From measurements of the melting curve and the accompanying volume changes, the heat of fusion ΔH_f of n-D_2 can be calculated with the Clausius-Clapeyron equation

$$\Delta H_f = T\frac{dP_m}{dT_m}\Delta V_m. \tag{21}$$

Dwyer et al. [58] directly measured the heat of fusion of solid p-H_2 and found their results to be well described by a linear function of the melting pressure. Although they offered no explanation for this simple behavior, it suggests that we attempt a similar representation. A least-squares fit to our calculated heats of fusion gives

$$\Delta H_f = 197.22 + 0.179 P_m \tag{22}$$

where the melting pressure P_m is in bars and ΔH_f is in J/mole. The average absolute deviation of the data from eq (22) is 0.17%. No better fitting results are obtained by including quadratic or other high-order terms to the empirical function.

Calculated ΔH_f are plotted as a function of pressure in figure 12. Included in the plot is the earlier direct result by Clusius and Bartholome [1], which is seen to be consistent with the present measurements. An extrapolation of eq (22) to the triple point yields a value of 197.25±0.40 J/mole. Kerr et al. [43] obtained 196.94±0.40 J/mole for the heat of fusion of o-D_2 at the triple point. Measurements on 80% p-D_2 by Grenier and White [35] give an average value of 197.41±0.40 J/mole. The general agreement among these independent data indicates that beyond the nominal error limits of ±0.40 J/mole there is no measurable dependence of the heat of fusion on *ortho-para* concentration in deuterium. The only inconsistent results are those presented by Bartholome [2] whose data on n-D_2 show ΔH_f *decreasing* with increasing temperature.

The molar volume V_{sm} of the solid along the melting line can be derived from the equation

$$V_{sm} = V_{lm}\left(1 - \frac{\Delta V_m}{V_{lm}}\right) \tag{23}$$

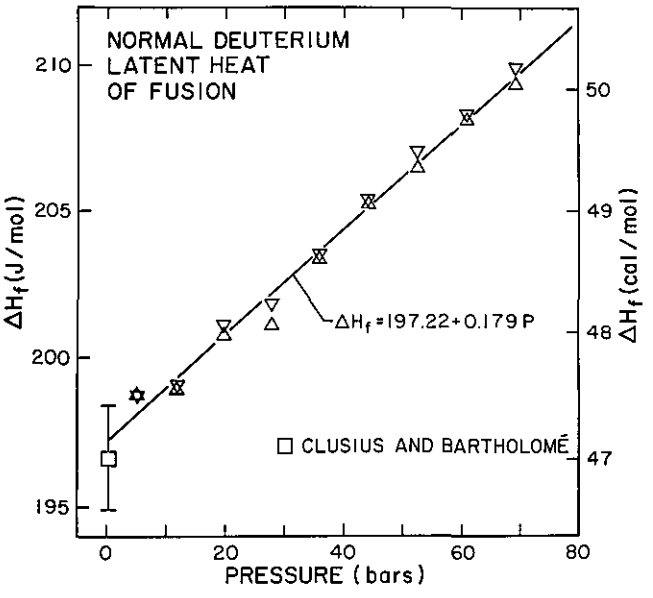

Figure 12—Data for the latent heat of fusion derived from eq (22). Included with these is the single direct measurement on n-D_2 by Clusius and Bartholome [1].

where the liquid molar volume V_{lm} at the same temperature and pressure is determined from eq (8). Calculated V_{sm} corresponding to the measured values of $\Delta V_m/V_{lm}$ in table 4 are plotted in figure 13. Also included in the plot are two points that Woolley et al. [4] derived from the work of Clusius and Bartholome [1] and Bartholome [2].

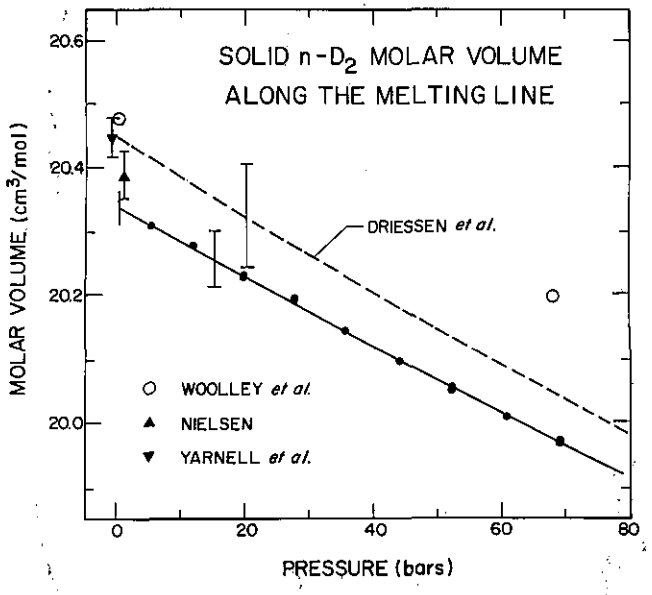

Figure 13—Data for the molar volume of solid n-D_2 along the melting curve derived from eq (23). The dashed line was derived from the equation of state of Driessen et al. [14]. Also included are two points compiled by Woolley et al. [4] and two neutron diffraction results [64,65].

The functional behavior of these data suggests a simple linear relationship. A least-squares fit gives

$$V_{sm}(P_m)=20.337-0.0053P_m \qquad (24)$$

where $V_{sm}(P_m)$ is in cm^3/mole and the melting pressure P_m is in bars. The average absolute deviation of the data from eq (24) is 0.015%. No improvement is obtained by including a quadratic term in the fitting polynomial. We estimate the accuracy of this expression to be about ± 0.04 cm^3/mole.

Within our range of measurements, eq (24) describes the data quite well, but it cannot be used reliably for extrapolation. A better representation is obtained by following some of the earlier work on p-H_2. Dwyer et al. [59] first measured the molar volume of solid p-H_2 along the melting line at pressures up to 340 bar. Younglove [30] later corrected portions of these data and fit the solid densities to a linear function of melting temperature. A similar least-squares fit to the present data gives

$$\rho_{sm}(T_m)=0.039133+0.0005362T_m \qquad (25)$$

where $\rho_{sm}(T)$ is the density of solid n-D_2 along the melting curve in moles/cm^3. Equations (24) and (25) both describe our measurements with comparable accuracy and precision, but eq (25) may provide a useful representation for the solid density to temperatures as high as 27 K. In the following discussion, we examine the consistency of eq (25), first with independent measurements on the low-pressure solid and then with various extrapolated data at higher pressures. We conclude this section with a discussion of the existing measurements of the dielectric constant of the solid and liquid phases.

An extrapolation of eq (25) to the measured triple point yields a density corresponding to $V_{sm}(T_{tp}=18.7067$ K$)=20.342\pm0.04$ cm^3/mole. It is possible to compare this value with the result of existing x-ray [60], electron [61], and neutron scattering experiments [62-65] on the low-pressure solid.

For our discussion, the most important of this earlier work is the single-crystal neutron diffraction study of Nielsen [64]. These data include lattice parameter measurements on o-D_2 along its saturated vapor pressure curve from 5 to 18 K. From the hcp lattice constants that Nielsen reported at 5 K, we deduce a molar volume of 19.94 cm^3/mole. With increasing temperature, expansion of the material in the **a** and **c** directions was observed to be uniform within the limits of experimental uncertainty. Nielsen gave an analytical expression for the thermal expansion; from it we calculate for o-D_2 a molar volume of 20.41 cm^3/mole at 18.7 K. Next, we apply the prescription of Driessen et al. [14] to calculate the small volume difference between *ortho* and normal deuterium at this temperature and density. The final result for solid n-D_2, 20.39 cm^3/mole, is larger by about 0.05 cm^3/mole than that found by extrapolating eq (25). However, if the lattice measurements are accurate to $\pm 0.05\%$, the uncertainty in the corresponding molar volume is ± 0.03 cm^3/mole. A small additional error is involved with the extrapolation to 18.7 K. When these uncertainties are combined with those of the present study, the neutron diffraction result is shown to agree with our triple-point value.

Nielsen [64] published the only measurements on large single-crystals. The remaining work includes powder-diffraction data [60,62,63,65] and one set of measurements on relatively thin samples grown on a cold substrate [61]. We have included a compilation of these results in table 5. All of the data were taken at temperatures lower than the triple point, but we have included corrections to the corresponding solid molar volumes of n-D_2 at 18.7 K in the manner described

Table 5. Compilation of existing measurements of the molar volume of solid deuterium.

References	Sample (% *para*)	Temperature	Measured molar volume (cm^3/mole)	Molar volume corrected to 18.7 K[a] (cm^3/mole)
Mucker et al. (1965) [62]	33%	13 K	20.08 (±0.12)[b]	20.39±0.12
neutron powder diffraction	2%	13 K	20.08 (±0.12)[b]	20.41±0.12
Schuch and Mills (1966) [60]	33–65%[c]	1..5 K	19.80±0.20[d]	20.28±0.20
x-ray powder diffraction				
Bostanjoglo and Kleinschmidt (1967)	33%	4.2 K	19.90±0.11	20.37±0.11
[61] electron powder diffraction				
Mucker et al. (1968) [63]	3%	12.9 K	20.02 (±0.12)[e]	20.33±0.12
neutron powder diffraction	33%	10.2 K	19.91 (±0.12)[e]	20.33±0.12
	63%	2.0 K	19.74 (±0.12)[e]	20.32±0.12
	80%	10.5 K	19.84 (±0.12)[e]	20.37±0.12
	80%	4.2 K	19.85 (±0.12)[e]	20.46±0.12
Nielsen (1973) [64]	2%	5.0 K	19.94 (±0.03)[f]	20.39±0.04
single-crystal neutron diffraction				
Yarnell et al. (1975) [65]	2%	4.2 K	19.994±0.013	20.45±0.03
neutron powder diffraction				

[a]This calculation is done in three steps. First, the measured molar volume is corrected according to the prescription of Driessen et al. [14] to the value corresponding to zero percent *para* at the same temperature. Next, the temperature correction is made to 18.7 K using the analytic expression for the linear thermal expansion by Nielsen [64]. Finally, the o-D_2 volume is corrected at 18.7 K to that of n-D_2 again according to reference [14]. We assume a error of ±0.03 cm^3/mole for this calculation. The accuracy limit in column 5 is taken as the square root of the sum of the squares of the error limit in column 4 and the assumed error in the temperature correction.

[b]Estimated error assumes ±0.005 Å uncertainty in a and ±0.005 in c/a.

[c]No trend was observed in the hcp molar volume with *para* concentration.

[d]We set the uncertainty limit equal to the observed data scatter.

[e]The ±0.6% volume error was calculated from the quoted ±0.2% uncertainty in the nearest neighbor distance.

[f]The ±0.15% volume error was calculated with an assumed 0.05% uncertainty for the lattice parameter measurements.

above. Generally, the corrected data are consistent with the extrapolated results of the present measurements. However, there are relatively large experimental uncertainties associated with most of the earlier work [60-63]. The data of Nielsen [64] and Yarnell et al. [65] are more precise. As we mentioned above, the solid molar volume obtained by extrapolating eq (25) to the triple point agrees with Nielsen's measurements, but it is 0.11 cm^3/mole lower than the corresponding value inferred from the work of Yarnell.

At higher pressures, the most instructive comparisons are made using the solid equations of state established by Driessen et al. [13,14]. This work was based in large part on their measurements of the isochores of solid n-H_2 and n-D_2 to pressures up to 2 kbar at the melting line. The molar volumes were not measured directly but were determined by correlating the isochore data with existing measurements at 4.2 K for both H_2 and D_2 [12] and along the melting line for H_2 [59]. The equations of state for p-H_2 and o-D_2 are presented in tabular form, and corrections to arbitrary *ortho-para* mixtures are accomplished by straightforward calculation.

A direct comparison of our data to those of Driessen et al. is not possible. Their lowest density isochore corresponds to 19.851 cm^3/mole, which is slightly beyond the range of our data. However, they did extrapolate their equation of state to low pressures. We interpolated their tabulated values to calculate the molar volume of n-D_2 at the temperatures and pressures corresponding to our melting line. The results are plotted in figure 13. The ±0.42% uncertainty was taken from figure 22 of their paper [14]. Our measurements agree with the extrapolated results of Driessen et al. within the combined error limits. However, we note that the most reliable of the low-pressure diffraction work [64,65] is more nearly consistent with the extrapolated equation-of-state than it is with eq (25).

Driessen et al. quoted a value of 19.95 cm^3/mole for o-D_2 at zero temperature and pressure. This corresponds closely to the volume, 19.94± 0.03 cm^3/mole, that Nielsen measured directly at 5 K. According to the equation of state, this isochore should intersect the melting line at 90.7 bar. The corresponding melting temperature, 20.90 K, was used in eq (25) to calculate an

extrapolated density, and from this we obtain the molar volume 19.87±0.04 cm³/mole. Nielsen's measurement corrected to the normal spin mixture at 20.90 K becomes 19.92±0.03 cm³/mole. Again, the two results agree within experimental error.

In addition to his low-pressure data, Nielsen measured the lattice parameters of hcp o-D_2 at 5 K and 275 bar. From these lattice data, we calculate a molar volume of 18.64±0.03 cm³/mole, which is consistent with the Driessen et al. analysis at that temperature. (Existing P-V data at low temperatures [12] were fitted to the Birch equation. At this solid density, this equation yields a pressure of 271.5 bar.)

According to eq (19) of reference [14], the isochore at 18.64 cm³/mole intersects the melting line at 422.5 bar. At this pressure the melting temperature, 27.45 K, in eq (25) yields a molar volume of 18.57±0.04 cm³/mole, which agrees with 18.63±0.03 cm³/mole, the Nielsen volume corrected to 33% *para* at 27.5 K. Equation (25) is thus seen to reproduce the extrapolated results of the neutron diffraction measurements within the combined limits of experimental error for the two experiments. This equation may, therefore, provide a useful representation for the solid density along the melting line to temperatures as high as 27 K.

There have been a few measurements of the dielectric constant of solid [52] and liquid [66,67] n-D_2. It is instructive to discuss these results in terms of the molecular polarizability of the material. To do this, it is necessary to combine the dielectric data with independent measurements of the sample density. The polarizability P_E can then be calculated from an expression such as the Clausius-Mossotti equation

$$P_E = \frac{3V}{4\pi N_a}\left(\frac{\epsilon-1}{\epsilon+2}\right) \tag{26}$$

where $N_a = 6.0225\times10^{23}$ molecules/mole and V is the molar volume.

We first apply eq (26) to the existing liquid data. Kogan et al. [66] measured the dielectric constant of liquid n-D_2 along the saturated vapor-pressure curve from the triple point to 20.4 K. From their 12 data points and the corresponding liquid molar volumes computed from eq (8), we calculate an average value of $P_E = 7.9371\times10^{-25}$ cm³ with a standard deviation of 0.0014×10^{-25} cm³. This result agrees with those derived from similar data reported by Constable et al. [67] in the range 18.9 to 23.0 K. From their 22 measurements, we calculate an average of 7.9330×10^{-25} cm³ with a standard deviation of 0.0077×10^{-25} cm³.

To our knowledge, the only solid phase measurement on n-D_2 is that published by Wallace and Meyer [52]. Their value, $\epsilon = 1.3324$, was obtained from a single sample under the melting pressure at 21.1 K. The molar volume of the sample is calculated from eq (25) to be $V_{sm} = 19.825$ cm³/mole. These values substituted into eq (26) give $P_E = 7.8388\times10^{-25}$ cm³ which is about 1.2% lower than the values derived from the liquid data.

The large difference between the derived polarizabilities for the solid and liquid phases is probably artificial. The melting pressure at 21.1 K is only 99.4 bar according to eq (3). There should be no significant change in the liquid polarizability at this temperature over the limited pressure interval between the vapor and melting curves. Udovidchenko and Manzhelii [51] measured isothermal compressibilities of solid p-H_2 to pressures as high as 180 bar. They assumed a pressure-independent molecular polarizability in their data analysis. The results agree with the compressibilities that Driessen et al. [14] later found from their isochoric measurements.

Again, there is probably little if any difference between the molecular polarizabilities of the solid and liquid phases at 21.1 K on the melting line. Once more, our justification derives from independent work on p-H_2. Younglove [30] first measured the dielectric constants of solid and liquid p-H_2 along the melting line. Although, these data suggest a possible difference of 0.4%, subsequent measurements by Wallace and Meyer [52] and Udovidchenko and Manzhelii [51] have not supported Younglove's findings. The later experiments obtained solid- and liquid-phase polarizabilities that are identical to within 0.1 to 0.2%, an accuracy limit imposed by the available solid density data. The large apparent difference in the deuterium polarizabilities suggests to us that more careful measurements of the dielectric constant are required for both solid and liquid in this pressure range.

3.8 Solid Thermal Expansivity and Isothermal Compressibility

Measurement accuracies of solid-phase properties are severely constrained with the present technique. The problem derives from the nonplastic-flow characteristics of the solid and a rather sensitive dependence of the experimental results on the homogeneity of the sample density. For measurements of both thermal expansivity and isothermal compressibility, it is necessary to measure changes in the sample volume that result from unequal deflections of the upper and middle diaphragms of the pressure cell (see Fig. 1). Volume changes of the thin disk-shaped solid always introduce radial variations in the compression. As P_1 is increased, for example, the middle diaphragm is displaced upward, and the sample

is compressed to a higher density at the center than around the periphery.

For liquids, the distortion of the sample geometry is no problem. Reasonably accurate results were even obtained earlier on solid helium [16,17], although hysteresis effects, particularly at the lowest temperatures indicate similar problems. With solid n-D_2, we cannot assume that our samples were free of internal strain even after several hours equilibration near the two-phase region. We observed that density gradients persisted in sufficient degree to preclude all but very approximate measurements of α and β for the solid.

We tried a number of approaches to defeat the problem but could only obtain reproducible results by allowing long (2-10 h) relaxation periods with the solid at temperatures and pressures near the melting curve. Typically, in the melting pressure range 20 to 70 bar, the isothermal compressibilities decreased from about 3.8 to 2.0×10^{-4} bar^{-1} with increasing P_m. Thermal expansivities were in the range 2.4 to 2.6×10^{-3}K^{-1} for melting temperatures between 19.2 and 20.4 K.

These results are somewhat inconsistent with our solid molar volume data. Consider the equation

$$-\frac{1}{V_{sm}}\left(\frac{dV_{sm}}{dP_m}\right)=\beta_{sm}-\frac{\alpha_{sm}}{dP_m/dT_m} \tag{27}$$

where β_{sm} and α_{sm} denote respectively the isothermal compressibility and thermal expansivity for the solid at melting. The quantity on the left-hand side of this equation represents a coefficient of compression for the solid along the melting curve. It can be calculated from the fitted curve of eq (24); the resulting values increase from 2.61×10^{-4} bar^{-1} at the triple point to 2.65×10^{-4} bar^{-1} at 70 bar. The average measured values over the pressure range 20 to 70 bar, $\beta_{sm}=2.73\times10^{-4}$ bar^{-1}, $\alpha_{sm}=2.56\times10^{-3}$ K^{-1}, and $dP_m/dT_m=41.5$ bar K^{-1}, yield the value 2.11×10^{-4} bar^{-1} for the right hand side of eq (27).

Estimates of the solid-phase properties are available from the Driessen et al. [14] equation of state. Although their tabulated equation is for o-D_2, the compressibility and thermal expansion coefficient for n-D_2 can be calculated from the information provided. In the temperature range 18.7 to 21.0 K, the differences between the differential quantities of o-D_2 and n-D_2 are less than 1%. At the triple point, we calculate a compressibility for solid n-D_2 of 4.28×10^{-4} bar^{-1} and a thermal expansion of about 5.3×10^{-3} K^{-1}. At $T_m=20.5$ K, the corresponding values are about 12% lower.

An indirect estimate of the solid thermal expansivity can be made from some of the data that we have already discussed. Consider the temperature change of the liquid enthalpy along the melting curve

$$\frac{dH_{lm}}{dT_m}=C_{P,lm}+V_{lm}\frac{dP_m}{dT_m}\left(1-T_m\alpha_{lm}\right). \tag{28}$$

In this expression $C_{P,lm}$ denotes the isobaric heat capacity of the liquid at the melting line. The right-hand side of eq (28) can be evaluated from eqs (4), (8), (11), and (17). At the triple point we obtain $dH_{lm}/dT_m=91.5\pm1.0$ J/mole K.

The enthalpy of the solid at melting H_{sm} is equal to the liquid enthalpy minus the heat of fusion. We may, therefore, write

$$\frac{dH_{sm}}{dT_m}=\frac{dH_{lm}}{dT_m}-\frac{d(\Delta H_f)}{dP_m}\frac{dP_m}{dT_m} \tag{29}$$

The second term evaluated from eqs (4) and (22) contributes an amount 7.0 ± 0.5 J/mol K. The combined results in eq (29) gives $dH_{sm}/dT_m=84.5\pm1.2$ J/mol K.

Clusius and Bartholome [1] and Kerr et al. [43] measured the specific heat of the solid along the vapor pressure curve. These data extrapolate to the triple point to yield $C_{P,sm}=11.0\pm0.1$ J/mole K. This value combined with dH_{sm}/dT_m, V_{sm} from eq (25), and dP_m/dT_m at the triple point give $\alpha_{sm}=3.8\pm0.6\times10^{-3}$ K^{-1}. This indirect estimate of the solid thermal expansivity lies about midway between the value derived from the work of Driessen et al. [14] and our direct result.

We began this section with a brief discussion of the problems that we met in applying our technique to solid samples. It is appropriate to conclude with some suggestions for improving the method. As we mentioned earlier, the major problem derives from the design of our pressure cell. Impressed changes in the sample volume always introduce radial inhomogeneities in the density. For solid deuterium, the very thin disk-shaped geometry of the sample combines with an inherently large internal friction. Together, they allow substantial pressure gradients to persist for prohibitively long periods of time.

We were unable to improve our results by annealing, even when this was done at pressures and temperatures very close to melting. We feel the only possible solution is to redesign the cell in a way that minimizes the radial density gradients. For example, it may be possible to construct a cell with a sample chamber thickness that is very nearly proportional to the displacement of the diaphragms. If this can be done, it is clear that changes in the sample volume will induce density gradients in the axial rather than the radial direction. Sample distortions can never be totally eliminated, but they should be far less severe in a carefully designed, lens-shaped sample than they were shown to be with our geometry.

3.9 Further Observations

Finally, we discuss the effects of *para* to *ortho* conversion and their possible influence on the PVT results. We ran a number of experiments to measure such effects explicitly in both hydrogen and deuterium. For both isotopes, spin compositions were determined from the thermal conductivity of the gas samples [68]. On solid-liquid mixtures of n-H_2, the measured time rate of change in x_p, the *para* mole fraction, was $dx_p/dt \simeq 0.01$ h^{-1}. This result agrees with the self-conversion rate given by Woolley et al. [4]. Measurements of the melting pressure P_m and the liquid molar volume V_l (close to the melting curve) as functions of time gave $dP_m/dt \simeq 0.06$ bar h^{-1} and $dV_l/V_l dt \simeq 7\times10^{-5}$ h^{-1}. These results divided by dx_p/dt gives $dP_m/dx_p \simeq 6$ bar and $dV_l/V_l\, dx_p \simeq 7\times10^{-3}$, which are consistent with previous results: P_m(p-H_2) − P_m(n-H_2) from the data of Woolley et al. [4], Mills and Grilly [28], and Goodwin and Roder [31]; V_l(p-H_2) − V_l(n-H_2) by Scott and Brickwedde [38] and Wallace and Meyer [69].

For liquid n-D_2, the rate of self conversion, dx_o/dt, was estimated by Woolley et al. [4] to be 5×10^{-5} h^{-1}. For the solid, Motizuki [70] calculated the value 5×10^{-4} h^{-1} which is in the range 2 to 8×10^{-4} h^{-1} that Grenier and White [35] obtained by direct measurement. We measured the conversion rate of n-D_2 several times in our cell. The results for dx_o/dt were between 1 and 3×10^{-4} h^{-1} for observation periods of 60 to 90 h. The data are reasonably consistent with the earlier theoretical and experimental work. The conversion rates are small, and we feel that our PVT measurements are not significantly influenced. The following numerical estimates should illustrate this point.

One effect of self-conversion is an increase in P_m at constant temperature. We noted in previous discussion that the melting pressures reported by Bereznyak and Sheinina [24] on o-D_2 exceed ours on n-D_2 (33.3% *ortho*) by about 2 bar. This difference scales to 6 bar for $\Delta x_p = 1$, which is similar to the difference in P_m between pure *ortho* and *para* hydrogen. For the self-conversion rate $dx_o/dt = 2\times10^{-4}$ h^{-1}, we should observe $dP_m/dt \simeq 1.2\times10^{-3}$ bar/h.

Another effect of conversion is an increase in the molar volume of the sample. An estimate of the fractional change in the liquid volume can be calculated from the equation

$$\frac{\Delta V_l}{V_l} = -\beta_l \left(\frac{\partial P_Q}{\partial x_p}\right)_{T,V} \Delta x_p \qquad (30)$$

where β_l is the compressibility of the liquid, x_p is the fraction of the *para* spin modification in the mixture, and P_Q is an effective pressure introduced by the electric quadrupole interactions of the *para* species. We estimate the value $(\partial P_Q/\partial x_p)_{T,V} \simeq 12.3$ bar from table 1 of Driessen et al. [14]. For liquid compressibilities on the order of 7×10^{-4} bar^{-1}, we calculate $\Delta V_l/V_l \simeq 8\times10^{-3}$ for $\Delta x_p = 1$, which is also similar to H_2. Thus in n-D_2 with $dx_p/dt = -dx_o/dp$, we expect the rate $dV_l/V_l\, dt \simeq 2\times10^{-6}$ h^{-1}.

The longest times taken for the various measurements were 1 h for the liquid α and β, 10 h for solid α and β, and 20 h for ΔV_m. The longest time of low-temperature exposure before P_m and V_l measurements were made was 12 h. Thus, in all cases the effects of *ortho-para* conversion are within the quoted accuracy limits of the data. It is nonetheless interesting to compare the values of P_m and V_l at the beginning and at the end of the long runs (60 to 90 h) involving ΔV_m.

Again, with an assumed conversion rate of 2×10^{-4} h^{-1}, we expect a fractional volume change in the liquid to be roughly 1.6×10^{-4} for an 80-h period. Volume changes of this magnitude are easily measured in our apparatus. Indeed the observations include such results, but there were also some changes that are much smaller and, in two cases, some large volume *decreases* (1.7 to 1.9×10^{-4}). However, volume losses were also observed in the p-H_2 measurements, where no conversion occurs, and these can be explained by a loss of the sample through a leaky cell valve.

For the melting pressure this self-conversion rate should produce an increase of about 0.10 bar for n-D_2 during an 80-h period. Actual measured values, shown in table 6, vary from −0.39 to +0.38 bar. The large decreases in P_m are not easily explained. If they were to

Table 6. Observed changes in the melting pressures of samples that had been held at low temperatures for 50- to 70-h periods.

T(K)	Seq. No.[1]	ΔP_m(bar)
18.83	9	0.00
19.00	5	−0.39
19.20	8	−0.28
19.20	11	0.10
19.40	4	0.31
19.60	6	−0.01
19.80	3	−0.06
19.80	12	0.19
20.00	7	−0.30
20.20	1	0.24
20.20	2	−0.03
20.40	10	−0.33
20.40	13	0.04
20.40	14	0.38

[1]Chronological order of the measurements.

be ascribed to bath temperature decreases, the ΔT would have to be on the order of 10 mK, which is far greater than our expected precision of a millikelvin or two.

There is evidence in some cases that a high initial measurement of P_m could have been made before the sample was adequately cooled; however, in other cases this explanation is unreasonable. For example, after the first run at 19.2 Kwas completed, we saw that a large decrease ($\Delta P_m = -0.28$ bar) had occurred in the melting pressure. We replaced the original sample with a fresh charge of n-D_2 from the storage bottle. The melting pressure of the second sample was then measured, and the result agreed with that obtained from the first sample when it was originally admitted to the cell and pressurized to cause freezing. The result removes the possibility of some kind of slow cooling of the cell, but it introduces the possibility of inadequate time for the liquid to be cooled or changed in some way with time.

Despite the lack of evidence for two solid structures in n-D_2, we did consider this possibility in connection with our observed melting pressure changes. If the Gibbs-energy functions of two solid phases are approximately equal, it should be quite easy to pressurize a liquid sample to the metastable solid form. It can be shown in this case that the observed P_m will be higher than that corresponding to the stable phase. At constant temperature the solid may then revert to the equilibrium structure, and as it does, the observed melting pressure will decrease. This argument is seen to hold for temperatures both above and below the assumed solid-solid-liquid triple point.

Although, as we mentioned, there is no direct evidence for more than a single solid structure in n-D_2, we did observe some curious behavior with p-H_2 in our cell. Recall that Manzhelii [53,54] reported volume decreases of 0.15% in solid p-H_2 with small increases of temperature. In p-H_2 and n-H_2, Bereznyak and Sheinina [24] observed kinks in the freezing curve near 14.9 K. Similarly, in our PVT apparatus, we observed $\Delta V \simeq -0.07\%$ in solid p-H_2 with slight increases of temperature. We also found the melting pressure of p-H_2 to decrease with time at rates of about 0.005 bar h^{-1}. Over time periods of 60 h, P_m decreases of approximately 0.3 bar were observed, similar to our measurements on n-D_2.

If this similarity supports the possibility that two (or more) solid phases exist in n-D_2, there is contrary evidence as well. In one of the long runs at 20.4 K, a melting pressure change of -0.33 bar was observed. After the run was completed but before the low-temperature valve was opened, the sample was held in the liquid phase for over an hour to assure that all of the solid had melted. The liquid was then refrozen and the melting pressure was again measured. The resulting value was identical to that obtained from the melting process only an hour before. This experiment tends to eliminate the possibility of a solid structure change with time. At best, it could indicate that such a change is fast when an "old" liquid is used. At this time, the anomalous changes of the melting pressure are not well understood.

4. Summary and Conclusions

The purpose of this study has been to provide an accurate and precise determination of the equation of state of n-D_2 in the region of the phase diagram near the triple point. We began by presenting measurements of the melting line. These data range in temperature from the triple point to 20.4 K. The melting pressures were fit to a quadratic function of temperature. The average deviation of the points from the smooth curve is about 0.1 bar, which is comparable to the precision of the measurements. The observed regularity of these data contrasts to the anomalous behavior reported in similar studies [24] on p-H_2, n-H_2, and o-D_2. The results of the earlier work were interpreted as evidence for the existence of solid-solid-liquid triple points in these systems. While this may be true, there appears to be no firm indication of a similar phenomenon in n-D_2.

We combined our melting data with existing vapor-pressure measurements to establish an accurate triple-point temperature. The result was corrected for the HD impurity measured by mass-spectrometric analysis. The value $T_{tp} = 18.723 \pm 0.010$ K was given as the triple-point temperature of pure-phase n-D_2. A detailed comparison of this result to existing data is given elsewhere [33].

Data for the isothermal compressibility and thermal expansivity of the liquid were collected in the temperature range 18.8 to 21.0 K and at pressures between 4 and 70 bar. We compared these with estimates of corresponding values derived from existing molar volume data [2,5,6]. The most accurate and precise of these earlier data [5,6] gave results that agree with ours to within a few percent. We also presented measurements of the molar volume of the liquid, which were made at nine points along the melting line. The combined liquid data were then fitted to a single empirical equation of state. The purpose of doing this is twofold. First, a description of the data by a single function is sufficient demonstration of their internal consistency. Second, the equation of state can be used to extrapolate beyond the limited range of the data and also to predict certain quantities that were not measured directly. This allows us to make indirect data comparison that would not otherwise be possible.

As an example of this, we began by interpolating our equation of state to compare the molar volume with existing measurements [2,6] at pressure. We then extrapolated the equation to the vapor-pressure curve where a number of direct measurements of the liquid molar volume [1,5] exist. The analysis was finally extended by incorporating some of the existing calorimetric data for the liquid [35,43,45]. This additional information allowed us to compare our results with existing sound velocity [46-48] and isochoric heat capacity measurements [3]. The overall conclusion of the analysis is that our measurements agree with the best available data for differential quantities, such as the compressibility, $(\partial P/\partial T)_V$, and sound velocity. However, small but significant uncertainties remain in the scale of the liquid data. Our volume measurements agree with those of Friedman et al. [6], but extrapolations of eq (8) to the vapor curve yield values that are at least 0.10 cm^3/mole lower than the measurements of Kerr [5].

Results for the volume change on melting were then given. These were followed by a brief review of the existing evidence for a solid-solid phase transition in hydrogen. The behavior of our volume-change measurements showed no irregularities that would indicate a similar behavior in n-D_2.

From the volume-change measurements and the slope of the melting curve we derived the corresponding heats of fusion and fitted them to a linear function of pressure. These results agree with existing measurements at low pressures [35,43]. Finally, we derived solid molar volumes along the melting curve. The corresponding solid densities were fit to a linear function of the melting temperature. This empirical function was extrapolated to both low and high temperatures to compare with existing data. We found that our extrapolations are consistent with values derived from the best existing solid-phase data [14,64].

We attempted to measure compressibilities and thermal expansion coefficients in the solid. The results of these measurements were found to be somewhat inconsistent with our solid densities along the melting curve. We briefly discussed the compressibility and thermal expansion coefficients that can be derived from the tabulated equation of state that Driessen et al. [14] presented. These results appear to be more nearly consistent with the observed solid compression. Finally, we derived an indirect estimate of the solid thermal expansion from a variety of data that had been presented earlier in the discussion. This calculation gave a higher value than we obtained from our direct measurements but lower than that deduced from the extrapolated equation of state.

The paper concluded with our unexplained observations of the changes of the melting pressure of the confined sample with time. We noted that these changes were opposite from what might be expected of the effects of *ortho-para* conversion.

The authors wish to thank Dr. R. L. Mills for participating in valuable discussions on topics in this paper and R. Jay Fries of the Laser Fusion Target Fabrication Group.

References

[1] Clusius, K., and E. Bartholome, Z. Physik. Chem. [B] **30**, 237 (1935).
[2] Bartholome, E. Z. Physik. Chem. [B] **33**, 387 (1936).
[3] Bartholome, E., and A. Eucken, Z. Electrochem. **42**, 547 (1936).
[4] Woolley, H. W.; R. B. Scott and F. G. Brickwedde, J. Res. Natl. Bur. Stand. (U.S.) **41**, 379 (1948).
[5] Kerr, E. C. J. Am. Chem. Soc. **74**, 824 (1952).
[6] Friedman, A. S.; M. Trzeciak and H. L. Johnston, J. Am. Chem. Soc. **76**, 1552 (1954).
[7] Prydz, R. Natl. Bur. Stand. (U.S.) NBS Reports 9276 (1967).
[8] Prydz, R.; K. D. Timmerhaus and R. B. Stewart, Adv. Cryog. Eng. **13**, 384 (1968).
[9] Mills, R. L.; D. H. Liebenberg and J. C. Bronson, J. Chem. Phys. **68**, 2663 (1978).
[10] Liebenberg, D. H.; R. L. Mills and J. C. Bronson, Phys. Rev. B **18**, 4526 (1978).
[11] Stewert, J. W. J. Phys. Chem. Sol. **1**, 146 (1956).
[12] Anderson, M. S., and C. A. Swenson, Phys. Rev. B **10**, 5184 (1974).
[13] Silvera, I. F.; A. Driessen and J. A. de Waal, Phys. Lett. **68A**, 207 (1978).
[14] Driessen, A.; J. A. de Waal and I. F. Silvera, J. Low Temp. Phys. **34**, 255 (1979).
[15] Grilly, E. R. Phys. Rev. **149**, 97 (1966).
[16] Grilly, E. R. J. Low Temp. Phys. **4**, 615 (1971).
[17] Grilly, E. R. J. Low Temp. Phys. **11**, 33 (1973).
[18] Goodwin, R. D.; D. E. Diller, H. M. Roder and L. A. Weber, J. Res. Natl. Bur. Stand. (U.S.) **67**, 173 (1963).
[19] Rubin, T.; H. W. Altman and H. L. Johnston, J. Am. Chem. Soc. **76**, 5289 (1954).
[20] Roder, H. M.; L. A. Weber and R. D. Goodwin, Natl. Bur. Stand. Monograph 94 (Aug. 1965).
[21] Souers, P. C.; C. K. Briggs, J. W. Pyper and R. T. Tsugawa, Lawrence Livermore National Laboratory, Livermore, CA 94550, UCRL-52226 (1977).
[22] The International Practical Temperature Scale of 1968. Metrologia **5**, 35 (1969).
[23] Grilly, E. R. J. Am. Chem. Soc. **73**, 843 (1951).
[24] Bereznyak, N. G., and A. A. Sheinina, Fiz. Nizk. Temp. **6**, 1255 (1980) [English trans., Sov. J. Low Temp. Phys. **6**, 608 (1980)].
[25] Keesom, W. H.; A. Bilj and H. van der Horst, Leiden Comm. **217a** (1931).
[26] Chester, P. F., and J. S. Dugdale, Phys. Rev. **95**, 278 (1954).
[27] Mills, R. L., and E. R. Grilly, Phys. Rev. **99**, 480 (1955).
[28] Mills, R. L., and E. R. Grilly, Phys. Rev. **101**, 1246 (1956).
[29] Goodwin, R. D. Cryogenics **2**, 353 (1962).

[30] Younglove, B. A. J. Chem. Phys. **48**, 4181 (1968).
[31] Goodwin, R. D., and H. M. Roder, Cryogenics **3**, 12 (1963).
[32] Bedford, R. E.; M. Durieux, R. Muijlwijk and C. R. Barber, Metrologia **5**, 47 (1969).
[33] Schwalbe, L. A., and E. R. Grilly (to be published in the J. Phys. Chem. Ref. Data).
[34] Bereznyak, N. G.; I. V. Bogoyavlenskii, L. V. Karnatsevich and V. S. Kogan, Zh. Eksp. Teor. Fiz. **57**, 1937 (1969) [Sov. Phys. JETP **30**, 1048 (1970)].
[35] Grenier, G., and D. White, J. Chem. Phys. **40**, 3015 (1964).
[36] Grilly, E. R. J. Am. Chem. Soc. **73**, 5307 (1951).
[37] Rudenko, N. S., and V. P. Slyusar', Zhur. Fiz. Khim. **43**, 781 (1969) [Russ. J. Phys. Chem. **43**, 434 (1969)].
[38] Scott, R. B., and F. G. Brickwedde, J. Res. Natl. Bur. Stand. (U.S.) **19**, 237 (1937), J. Chem. Phys. **5**, 736 (1937).
[39] Roder, H. M.; D. E. Diller, L. A. Weber and R. D. Goodwin, Cryogenics **3**, 16 (1963).
[40] Weber, L. A.; D. E. Diller, H. M. Roder and R. D. Goodwin, Cryogenics **2**, 236 (1962).
[41] White, D.; A. S. Friedman and H. L. Johnston, J. Am. Chem. Soc. **72**, 3927 (1950).
[42] Onnes, H. K., and C. A. Crommelin, Leiden Comm. **137a** (1913).
[43] Kerr, E. C.; E. B. Rifkin, H. L. Johnston and J. T. Clarke, J. Am. Chem. Soc. **73**, 282 (1951).
[44] Roder, H. M.; G. E. Childs, R. D. McCarty and P. E. Angerhofer, Natl. Bur. Stand. (U.S), Tech. Note 641 (Oct. 1973).
[45] Brouwer, J. P.; A. M. Vossepoel, C. J. N. Van den Meijdenberg and J. J. M. Beenakker, Physica **50**, 125 (1970).
[46] Bezuglyi, P. A., and R. Kh. Minyafaev, Fiz. Tverd. Tela **9**, 3622 (1967) [Soviet Phys. Solid State **9**, 2854 (1968)].
[47] Wanner, R., and H. Meyer, J. Low Temp. Phys. **11**, 715 (1973).
[48] Pashkov, V. V., and E. V. Konovodchenko, Fiz. Nizk. Temp. **4**, 436 (1978) [Sov. J. Low Temp. Phys. **4**, 212 (1978)].
[49] Roder, H. M. Cryogenics **13**, 439 (1973).
[50] Cook, G. A.; R. F. Dwyer, O. E. Berwaldt and H. E. Nevins, J. Chem. Phys. **43**, 1313 (1965).
[51] Udovidchenko, B. G., and V. G. Manzhelii, J. Low Temp. Phys. **3**, 429 (1970).
[52] Wallace, B. A., and H. Meyer, J. Low Temp. Phys. **15**, 297 (1974).
[53] Manzhelii, V. G.; B. G. Udovidchenko and V. B. Esel'son, Zh. Eksp. Teor. Fiz. Pis'ma **18**, 30 (1973) [Sov. Phys.--JETP Lett. **18**, 16 (1973)].
[54] Manzhelii, V. G.; B. G. Udovidchenko and V. B. Esel'son, Fiz Nizk. Temp. **1**, 799 (1975) [Sov. J. Low Temp. Phys. **1**, 384 (1975)].
[55] Mills, R. L. J. Low Temp. Phys. **31**, 423 (1978).
[56] Krupskii, I. N.; Yu. E. Stetsenko and G. N. Shcherbakov, Zh. Eksp. Teor. Fiz. Pis'ma **23**, 442 (1976) [Sov. Phys.--JETP Lett. **23**, 400 (1976)].
[57] Bereznyak, N. G., and A. A. Sheinina, Fiz. Nizk. Temp. **7**, 685 (1981) [Sov. J. Low Temp. Phys. **7**, 335 (1981)].
[58] Dwyer, R. F.; G. A. Cook, B. M. Shields and D. H. Stellrecht, J. Chem. Phys. **42**, 3809 (1965).
[59] Dwyer, R. F.; G. A. Cook, O. E. Berwaldt and H. E. Nevins, J. Chem. Phys. **43**, 801 (1965).
[60] Schuch, A. F., and R. L. Mills, Phys. Rev. Lett. **16**, 616 (1966).
[61] Bostanjoglo, O. and R. Kleinschmidt, J. Chem. Phys. **46**, 2004 (1967).
[62] Mucker, K. F.; S. Talhouk, P. M. Harris, D. White and R. A. Erickson, Phys. Rev. Lett. **15**, 586 (1965).
[63] Mucker, K. F.; P. M. Harris, D. White and R. A. Erickson, J. Chem. Phys. **49**, 1922 (1968).
[64] Nielsen, M. Phys. Rev. **B7**, 1626 (1973).
[65] Yarnell, J. L.; R. L. Mills and A. F. Schuch, Fiz. Nizk. Temp. **1**, 760 (1975) [Sov. J. Low Temp. Phys. **1**, 366 (1975)].
[66] Kogan, V. S.; Yu. Ya. Milenko and T. K. Grigorova, Physica **53**, 125 (1971).
[67] Constable, J. H.; C. F. Clark and J. R. Gaines, J. Low Temp. Phys. **21**, 599 (1975).
[68] Grilly, E. R. Rev. Sci. Instr. **24**, 72 (1953).
[69] Wallace, B. A., and H. Meyer. Proceedings of the 13th International Conference on Low Temperature Physics, Boulder, CO, Vol. 2, p. 194 (1972).
[70] Motizuki, K. J. Phys. Soc. Japan **17**, 1192 (1962).
[71] Bereznyak, N. G., and A. A. Sheinina, Fiz. Nizk. Temp. **3**, 804 (1977) [Sov. J. Low Temp. **3**, 6 (1977)].

JOURNAL OF RESEARCH of the National Bureau of Standards
Vol. 89, No. 3, May-June 1984

An Equilibrium Model for the Calculation of Activity and Osmotic Coefficients in Aqueous Solutions

Robert N. Goldberg

National Bureau of Standards, Gaithersburg, MD 20899

Accepted: March 13, 1984

A procedure is described for the calculation of activity and osmotic coefficients which is based upon a knowledge of the equilibria in solution and assumed single-ion activity coefficients. The procedure permits one to introduce chemical equilibria of various types (ion-pairing, complexation, hydration, and hydrolysis) into a model which can be used to calculate values of the excess Gibbs energy and the activity and osmotic coefficients. Both the Debye-Hückel theory and Pitzer's expression are used to calculate the electrostatic contribution to the single-ion activity coefficients. Calculations have been performed on aqueous sulfuric acid, acetic acid, hydrofluoric acid, cadmium chloride, copper sulfate, and sodium carbonate. Properties which have been calculated are the excess Gibbs energy, the osmotic coefficient, the mean ionic activity coefficient, and Frank's single-ion activity coefficient function. Agreement between calculated and measured properties has been obtained up to molalities of ≈ 1.0 mol kg^{-1}

Key words: acetic acid; activity coefficient; cadmium chloride; copper sulfate; equilibrium; excess Gibbs energy; hydrofluoric acid; models of solutions; osmotic coefficient; sodium carbonate; sulfuric acid.

1. Introduction

Equilibrium models have been used [1 – 15][1] both for the prediction and for the correlation of activity and osmotic coefficient data in aqueous electrolyte solutions. These equilibrium models are particularly appropriate when one is dealing with solutions which exhibit association, complexation, hydration, or hydrolysis. When applied to such solutions, they are superior to the use of a model that assumes the electrolyte in solution to be a fully dissociated strong electrolyte. A variety of approaches has been used in these equilibrium models for treating these various types of equilibria in solution and for the calculation of the activity and osmotic coefficients. Several different types of functions for the calculation of the electrostatic contribution to the activity coefficient of the ions in solution have also been used.

The purposes of this paper are to 1) describe a procedure for (a) the calculation of activity and osmotic coefficients in aqueous solutions that uses a generalized approach for treating the equilibria in solution, and (b) the calculation of the Gibbs energy properties, 2) clarify the distinction between the stoichiometric and species quantities, frequently a source of confusion in the literature, and 3) explore the effects of parameter variations in the model on calculated values of the thermodynamic properties as applied to several representative types of electrolyte solutions. Using the equilibrium model, one can also calculate the values of the activity coefficients of individual ions. This permits one to then calculate values for Frank's [16] single-ion activity coefficient function.

About the Author, Paper: Robert N. Goldberg is with the NBS Chemical Thermal Dynamics Division. The research reported on was carried out at NBS under the sponsorship of the NBS Office of Standard Reference Data and the U.S. Department of Energy.

[1] Figures in brackets indicate literature references at the end of this paper.

2. The Model

A fundamental idea used here is the distinction between the stoichiometric components of which a system is composed and the particle constituents, or species, which are introduced to account for the properties of a solution. Stoichiometric quantities will be designated by "st" when not otherwise clearly indicated. Species or particle quantities will always be designated by a " ˆ " placed over the quantity. For example, for the solution formed from 0.1 moles of pure $H_2SO_4(\ell)$ and 1 kg/M_1 moles of $H_2O(\ell)$, the stoichiometric molality of H_2SO_4 is $m(H_2SO_4)=0.1$ mol kg^{-1}, $m(SO_4^{2-})=0.1$ mol kg^{-1}, and $m(H^+)=0.2$ mol kg^{-1} if one views the electrolyte as being completely dissociated. However, if one considers the equilibrium: $SO_4^{2-}(aq)+H^+(aq)=HSO_4^-(aq)$, adopts a K of 99[2] for it [17], and uses a Debye-Hückel type expression (see eq (5)) for the activity coefficients of the ions with a B parameter equal to zero, one calculates $\hat{m}(H^+)=0.134$ mol kg^{-1}, $\hat{m}(SO_4^{2-})=0.0342$ mol kg^{-1}, $\hat{m}(HSO_4^-)=0.0658$ mol kg^{-1}, and $\hat{m}(H_2SO_4)=0.0$

[2] Throughout this paper the activity will always have units of mol kg^{-1}. The equilibrium constants, formed as products and quotients of activities, will have units of mol kg^{-1}, or kg mol^{-1}, or, for symmetrical reactions, will be dimensionless. For sake of brevity, the units for equilibrium constants will be omitted.

GLOSSARY

Roman

a	activity
b	constant equal to 1.2 in Pitzer's equation
h	hydration number
m	molality/mol kg^{-1}
n	amount or moles of substance
p	pressure
t_{jk}	number of moles of species S_{jk} participating in a given reaction
z	charge
A	an anion
A_m, A_ϕ	Debye-Hückel constants; $A_m=3A_\phi=1.17642$ kg$^{1/2}$ mol$^{-1/2}$ at 298.15 K
B	parameter in the Debye-Hückel equation
C	a cation
I	ionic strength
G	Gibbs energy
K	equilibrium constant
M	molar mass/kg mol^{-1}
N_s, N_e, N_c, N_k	number of species in solution, equilibria, components, and, respectively, species in the kth equilibrium
R	gas constant
S_{jk}	the jth species in the kth equilibrium
T	temperature
X	mole fraction

Greek

γ	activity coefficient
δ_{ij}	Kronecker delta; $\delta_{ij}=1$ if i=j, $\delta_{ij}=0$ if i≠j
$\delta_\pm$	Frank's single-ion activity coefficient function
λ_{ij}	pair-wise interaction parameter
μ_{ijk}	triplet interaction parameter
ν	ion number
ξ	extent of reaction variable
ϕ	osmotic coefficient
ϕ_x	rational osmotic coefficient

Superscripts

ex	excess
id	ideal
st	stoichiometric
o	standard value quantity
*	the property of the pure substance
ˆ	a species quantity

Subscripts

a	an anion
c	a cation except when used with capital Roman N as N_c
e	see Roman N_e
i, j, k	a species or used as indices; also see N_k under Roman
ℓ	a component
m	see A_m under Roman
r	a reference cation or anion
s	see N_s under Roman
1	water
±	mean ionic
ϕ	see A_ϕ under Roman

mol kg^{-1}. Physical quantities other than amounts of substance can also be viewed as particle quantities. In particular it is the distinction between G^{ex} and $\hat{G}^{ex}$ which forms the basis of the model presented herein.

The general system to be considered is formed from 1 kg/M_1 moles of water and n_ℓ($\ell=2$ to N_c) moles of other components. In terms of a particle model, the system can be viewed as being formed from $\hat{n}_1$ moles of water and $\hat{n}_i$(i=2 to N_s) moles of particles or species. The amount of water (n_1) will always be designated by a subscript "1." The components and the species other than water will be designated by subscripts "ℓ" and "i," respectively, with i and $\ell \geqslant 2$.

Each component ℓ in the solution is represented as $C_{\nu_{\ell c}}^{z_{\ell c}} A_{\nu_{\ell a}}^{z_{\ell a}}$ where C and A are the reference cations and anions, respectively. The charges of the cations and anions are $z_{\ell c}$ and $z_{\ell a}$, respectively; the ion-numbers are $\nu_{\ell c}$ and $\nu_{\ell a}$, respectively. It is important to note that the choice of reference species is arbitrary; e.g., for a solution of aqueous sulfuric acid, the reference species could be selected as either two H^+ ions and one SO_4^{2-} ion or as one H^+ ion and one HSO_4^- ion. In the former case, sulfuric acid would be represented as $(H^+)_2(SO_4^{2-})_1$ and in the latter case as $(H^+)_1(HSO_4^-)_1$. While the choice of reference species is arbitrary, it will not affect the amounts of the various species one calculates given the same set of equilibrium constants and allowed species.However, as will be seen later, the choice does affect the values of several of the stoichiometric thermodynamic properties.

The Gibbs energy of the solution in the stoichiometric representation is given by

$$G=(m^\dagger \text{kg})G_1+\sum_{\ell=2}^{N_c}(\nu_{\ell c}G_{\ell c}+\nu_{\ell a}G_{\ell a})m_\ell \qquad (1)$$

where $m^\dagger$ is the molality of water in pure water and $G_{\ell c}$ and $G_{\ell a}$ are, respectively, the chemical potentials of the reference cation and anion of the ℓ^{th} component in the solution. In terms of an equilibrium or species model of the solution, the Gibbs energy is given by

$$G=\sum_{i=1}^{N_s}\hat{n}_i\hat{G}_i \qquad (2)$$

If the equilibrium model is accurate, the Gibbs energy of the solution calculated using eqs (1) and (2) will be identical and the chemical potentials and the activities of the i^{th} species will be the same in both the stoichiometric and species representations. The development to follow will start with a description of the solution in terms of the equilibria assumed to be present in solution, an assumed expression(s) for the activity coefficients of the solute species in solution, and the calculation of the activity of the water using the Gibbs-Duhem equation. It is important to note that there may be several equilibrium models of a solution which yield agreement with calculated properties. Thus agreement between calculated and measured properties does not, in the absence of direct molecular information, prove the correctness of the model used.

The equilibria in solution are described by a series of chemical equations:

$$\sum_{j=1}^{N_k} t_{jk}\,S_{jk}=0, \qquad k=1 \text{ to } N_e \qquad (3)$$

where S_{jk} is the j^{th} species in the k^{th} equilibrium, N_k is the number of species in the k^{th} equilibrium, N_e is the total number of equilibria, and t_{jk} is the number of moles of species S_{jk} participating in a given equilibrium; t_{jk} is positive if S_{jk} is a product and is negative if S_{jk} is a reactant. The equilibrium constants are:

$$K_k=\prod_{j=1}^{N_k}\hat{a}_{jk}^{t_{jk}} \qquad k=1 \text{ to } N_e \qquad (4)$$

where $\hat{a}_{jk}$ is the activity of species S_{jk}. Since $\hat{a}_i$ is equal to the product of the molality of the i^{th} species ($\hat{m}_i$) and its activity coefficient ($\hat{\gamma}_i$), the complete formulation of the equations which describe the equilibria in solution requires that some assumptions(s) be made concerning the form of the $\hat{\gamma}_i$'s ($i \geqslant 2$) in solution. In this paper two different expressions for the $\hat{\gamma}_i$'s will be used:

$$\ell n\,\hat{\gamma}_i=-A_m\hat{z}_i^2\hat{I}^{1/2}/(1+B\hat{I}^{1/2}) \qquad (5)$$

and

$$\ell n\,\hat{\gamma}_i=-\hat{z}_i^2A_\phi[\hat{I}^{1/2}/(1+b\hat{I}^{1/2})+(2/b)\,\ell n(1+b\hat{I}^{1/2})] \qquad (6)$$

Equation (5) is the Debye-Hückel equation with an excluded volume or "ion-size" parameter B in the denominator. Equation (6) is the leading term of Pitzer's expression for $\hat{\gamma}_i$ [18]; he has set b equal to 1.2. A_m and A_ϕ are Debye-Hückel constants, where $A_m=3A_\phi=1.17642$ $kg^{1/2}$ $mol^{-1/2}$ at 298.15 K. Equations (5) and (6) can be extended by the addition of the expression:

$$\sum_{i=j}^{N_s}\sum_{j=1}^{N_s}\lambda_{ij}\hat{m}_j+\sum_{i=1}^{N_s}\sum_{j=1}^{N_s}\sum_{k=1}^{N_s}\mu_{ijk}\hat{m}_j\hat{m}_k \qquad (7)$$

where λ_{ij} and μ_{ijk} are, respectively, the interaction parameters for pairs and triplets of particles. We shall later return to the subject of the extensions of eqs (5) and (6) and to several other aspects of the choice of an expression for $\hat{\gamma}_i$. It should be noted that I is calculated as

$$I=(1/2)\sum_{i=2}^{N_s}\hat{m}_i\hat{z}_i^2 \tag{8}$$

We have formulated the equilibrium equations using an extent of reaction variable ξ. Thus, the amount of the i^{th} species in solution is given by

$$\hat{n}_i=(m^\dagger\mathrm{kg})\delta_{il}+\sum_{\ell=1}^{N_c}(\nu_{\ell c}n_\ell\delta_{ir}+\nu_{\ell a}n_\ell\delta_{ir})$$
$$+\sum_{k=1}^{N_e}\sum_{j=1}^{N_k}t_{jk}\xi_k\delta_{ij}, \qquad i\geqslant 1 \tag{9}$$

where ξ_k is the extent of reaction variable for the k^{th} equilibrium and δ_{ij} is the Kronecker delta; r is an integer which serves to identify the reference cation and anion of each of the components in the solution. The first summation term on the right side of eq (9) specifies the amount of species i which is formed in the absence of any equilibria in solution; the second summation term specifies the contributions, which may be positive or negative, to the amount of species i in solution from the equilibria in solution. If the water is a participant in the equilibria in solution, $\hat{n}_1$ must also be calculated using the above equation. Hydration numbers can be introduced directly using

$$\hat{n}_1=\hat{n}_1\ (\text{eq (9)})-\sum_{i=2}^{N_s}\hat{h}_i\hat{n}_i \tag{10}$$

where $\hat{n}_1$ (eq(9)) is the amount of water calculated using eq (9) and $\hat{h}_i$ is the number of waters of hydration attached to the i^{th} species. If the water participates in the equilibria in solution or if hydration numbers are introduced, $\hat{n}_1\ \mathrm{kg}^{-1}$ will not be equal to $m^\dagger$. The $\hat{m}_i$ are given by

$$\hat{m}_i=\hat{n}_i(m^\dagger/\hat{n}_1), \qquad i\geqslant 2 \tag{11}$$

The activities of the species are given by

$$\hat{a}_i=\hat{m}_i\hat{\gamma}_i, \qquad 1\geqslant 2 \tag{12}$$

Thus in a model where hydration is introduced, both $\hat{m}_i$ and $\hat{a}_i$ will be affected by changes in both $\hat{n}_1$ and $\hat{n}_i$ ($i\geqslant 2$).

To obtain a numerical solution of eq (4), it is necessary to make some initial guess for the activity of water if it is a participant in the equilibria in solution; we have generally used a value of unity. Thus, having formulated the simultaneous nonlinear eq (4), which necessarily include eqs (8) to (12) and eq (5) or (6), one is left with a numerical problem to obtain a self-consistent solution of these equations. It is assumed that, while such a solution may be difficult to obtain for large systems, a unique solution does exist and that one now has values for I, $\hat{m}_i$ and $\hat{n}_i$ for $i\geqslant 1$ and for $\hat{\gamma}_i$ and $\hat{a}_i$ for $i\geqslant 2$.

The activity of the water can now be calculated by application of the Gibbs-Duhem equation stated in terms of excess properties of the species

$$\hat{n}_1 d\hat{G}_1^{ex}=-\sum_{i=2}^{N_s}\hat{n}_i d\hat{G}_i^{ex} \tag{13}$$

Use of eqs (11) and (13) leads to

$$m^\dagger d\hat{G}_1^{ex}=-\sum_{i=2}^{N_s}\hat{m}_i d\hat{G}_i^{ex} \tag{14}$$

It is also necessary to adopt some conventions concerning the limits of $\hat{a}_1$ and $\hat{\gamma}_i$. The conventions used herein are $\hat{a}_1\rightarrow 1$ and, for $i\geqslant 2$, $\hat{\gamma}_i\rightarrow 1$ as $\sum_{i=2}^{N_s}\hat{m}_i\rightarrow 0$; also, $\hat{\gamma}_i^{id}$ ($i\geqslant 2$) is defined to be equal to unity[3]. These conventions, together with the definitions of the activity $\hat{a}_i$, the activity coefficient $\hat{\gamma}_i$, and the definition of the excess Gibbs energy of the i^{th} species given in the following equations

$$\hat{a}_i=\exp[(G_i-G_i^\circ)/RT] \qquad ,i\geqslant 1 \tag{15}$$

$$\hat{\gamma}_i=\hat{a}_i/\hat{m}_i \qquad ,i\geqslant 2 \tag{16}$$

and

$$G_i^{ex}=G_i-G_i^{id} \qquad ,i\geqslant 1 \tag{17}$$

lead to

$$G_i^{ex}=RT\ell\hat{n}\hat{\gamma}_i \tag{18}$$

The introduction of eqs (5) and (18) into eq (14) yields

$$\hat{G}_1^{ex}=(2A_m RT/m^\dagger B^3)[(1+B\hat{I}^{1/2})$$
$$-2\ell n(1+\hat{B}\hat{I}^{1/2})-(1+B\hat{I}^{1/2})^{-1}] \tag{19}$$

Similarly, one obtains, using eq (6) instead of eq (5), the relationship

$$\hat{G}_1^{ex}=(2A_\phi RT/m^\dagger)\ [\hat{I}^{3/2}/(1+b\hat{I}^{1/2})] \tag{20}$$

We now consider an ideal reacting solution in which $\hat{\gamma}_i$ ($i\geqslant 2$) is equal to unity at all temperatures, pressures,

[3] This is the convention most frequently used in the description of aqueous electrolyte solutions. It is based upon the molality scale. A different convention based upon the mole fraction scale is commonly used for the description of non-electrolyte solutions.

and compositions and which also allows for the presence of both equilibria and hydration in solution. Application of the Gibbs-Duhem equation to such a solution leads to

$$\ell n\, \hat{a}_1^{id} = -\sum_{i=2}^{N_s} \hat{m}_i/m_1^* \tag{21}$$

and this in turn with eq (15) leads to

$$\hat{G}_1^{id} = \hat{G}_1^{\circ} - (RT/m_1^*) \sum_{i=2}^{N_s} \hat{m}_i \tag{22}$$

Since an excess property is defined as the difference between the real and the ideal, it follows from eqs (15) and (22) that

$$\ell n \hat{a}_1 = \hat{G}_1^{ex}/RT - (\sum_{i=2}^{N_s} \hat{m}_i/m_1^*) \tag{23}$$

If the equilibrium model is an accurate representation of the solution, a_1 is equal to $\hat{a}_1$. We thus have a procedure for the computation of the activity of the water which starts with an equilibrium model of the solution and an assumed expression for the activity coefficients in the solution. Since it is necessary to make an initial guess as to the value of the activity of the water, the calculation should be repeated using the value of $\hat{a}_1$ from the previous iteration until convergence to within a given tolerance in its value is obtained. The (stoichiometric) osmotic coefficient is calculated as

$$\phi = -(m_1^*/\sum_{\ell=2}^{N_c} \nu_\ell m_\ell)\, \ell n a_1 \tag{24}$$

where m_ℓ is the stoichiometric molality of component ℓ and ν_ℓ is equal to $(\nu_{\ell c} + \nu_{\ell a})$. Note that ν_ℓ is unity for a non-electrolytic component and that, as stated earlier, the value of the osmotic coefficient is dependent upon the choice of the reference species selected for each component in the solution.

The stoichiometric activity coefficients can be calculated using the principle that the chemical potential is independent of any representation of it. Equating $\hat{a}_i$, to a_i, the stoichiometric single-ion activity coefficient is given by

$$\gamma_i^{st} = \hat{m}_i \hat{\gamma}_i / m_i^{st} \tag{25}$$

where m_i^{st} is the total stoichiometric molality of the i^{th} species in solution. The mean ionic activity coefficient of component ℓ is given by

$$\gamma_{\ell\pm} = (\gamma_{\ell c}{}^{\nu_{\ell c}} \cdot \gamma_{\ell a}{}^{\nu_{\ell a}})^{1/\nu_\ell} \tag{26}$$

As was the case for the osmotic coefficient, the value of the mean ionic activity coefficient is dependent upon the reference species selected for a given component.

Other stoichiometric Gibbs energy properties can be calculated in addition to the activity of the water, the osmotic coefficient, and the mean ionic activity coefficient of the ℓ^{th} component. Additional properties of the water are calculated as follows:

$$G_1^{ex} = RT\, \ell n a_1 + (RT/m_1^*) \sum_{\ell=2}^{N_c} \nu_\ell m_\ell \tag{27}$$

$$G_1 = G_1^{\circ} + RT\, \ell n a_1 \tag{28}$$

$$\gamma_1 = a_1/X_1 \tag{29}$$

and

$$\phi_x = (\ell n a_1)/(\ell n X_1) \tag{30}$$

Note that eqs (29) and (30) are definitions of the activity coefficient of the water (γ_1), and of the rational osmotic coefficient (ϕ_x), respectively. These two quantities have not been frequently used in the literature. The properties of the solutes are:

$$G_\ell^{ex} = \nu_\ell RT\, \ell n \gamma_{\ell\pm} \tag{31}$$

$$\gamma_\ell = \exp(G_\ell^{ex}/RT) \tag{32}$$

$$a_\ell = m_\ell \gamma_\ell \tag{33}$$

$$G_\ell - G_\ell^{\circ} = RT\, \ell n a_\ell \tag{34}$$

and

$$a_{\ell\pm} = m_{\ell\pm} \gamma_{\ell\pm} \tag{35}$$

where the mean ionic molality of component ℓ is defined as

$$m_{\ell\pm} = \{(\nu_{\ell c} m_\ell)^{\nu_{\ell c}} (\nu_{\ell a} m_\ell)^{\nu_{\ell a}}\}^{1/\nu_\ell} \tag{36}$$

Finally, the total properties of the solution are

$$G^{ex}=\sum_{\ell=1}^{N_c} n_\ell G_\ell^{ex} \tag{37}$$

and

$$G-G^{\circ}=\sum_{\ell=1}^{N_c} n_\ell(G_\ell-G_\ell^{\circ}) \tag{38}$$

Equation (27) is the stoichiometric analogue of eq (23). Equations (29) and (30) are, respectively, the definitions of the activity coefficient of the water and of the rational osmotic coefficient. The steps used in the overall computational procedure are summarized in figure 1.

It is interesting to consider the consequences of the ideal behavior of all of the solute particles in the species representation, i.e., $\hat{\gamma}_i=1$ for $i\geqslant 2$. Application of eqs (21), (23), and (24) to such a solution leads to

$$\phi=\sum_{i=2}^{N_s} \hat{m}_i/\sum_{\ell=2}^{N_c} \nu_\ell m_\ell \tag{39}$$

Application of eqs (25) and (26) leads to

$$\gamma_{\ell\pm}=(\hat{m}_c/m_c)^{\nu_{\ell c}}(\hat{m}_a/m_a)^{\nu_{\ell a}} \tag{40}$$

If the stoichiometric and species representations are identical, then ϕ and $\gamma_{\ell\pm}$ will be equal to unity. This is the case when there are no chemical interactions (i.e., association, hydration, or hydrolysis) present in solution and the stoichiometric reference species chosen are the only ones present in solution.

An additional interesting feature of this model is that properties of individual ions and species are calculated (eq (25)). Unlike the stoichiometric properties given in eq (24) and eqs (26) to (35), there are presently no experimental data available with which one can compare these calculated values. Frank [16] has defined a quantity $\delta_\pm$ characteristic of single-ion properties for a binary electrolyte:

$$\delta_\pm=(\gamma_c^{\nu_c}/\gamma_a^{\nu_a})^{1/\nu} \tag{41}$$

The definition is easily extended to multicomponent systems as was done for the case of the mean ionic activity coefficient (see eq (26)) and values of $\delta_{\ell\pm}$ can also be calculated if the equilibria in solution are known.

An alternative way of viewing this model uses the definition of the excess Gibbs energy

$$G^{ex}=G-G^{id} \tag{42}$$

and its analogue for the species representation

Figure 1 — Steps for the calculation of the amounts of species in solution and of the stoichiometric Gibbs energy properties of the solution.

1. Set up the equilibrium eqs (1).

2. Specify the stoichiometric amounts of each component in the solution.

3. Specify the values of K_K, eq (4).

4. Choose an expression for $\hat{\gamma}_i$, eq (5) or (6).

5. Make an initial guess for $\hat{a}_1$.

6. Solve eqs (4) in a manner self-consistent with eqs (8) to (12) and with eq (5) or (6).

7. Calculate $\hat{G}_1^{ex}$, using eq (19) or (20).

8. Calculate $a_1=\hat{a}_1$, eq (23).

9. If a_1 is equal to the initial guess of $\hat{a}_1$, go to step 10; if not, return to step 6.

10. Make a choice of stoichiometric reference species.

11. Calculate ϕ using eq (24) and $\gamma_\pm$ using eqs (25) and (26).

12. Calculate the other stoichiometric properties, eqs (27) to (35).

$$\hat{G}^{ex} = G - \hat{G}^{id} \tag{43}$$

Since the Gibbs energy is independent of representation,

$$G^{ex} = \hat{G}^{ex} + \hat{G}^{id} - G^{id} \tag{44}$$

Similar equations hold for G_ℓ^{ex}, $\ell \geq 1$. From the definition of ideality,

$$\hat{G}_i^{id} = \hat{G}_i^{o} + RT\,\ell n \hat{m}_i \tag{45}$$

Equations analogous to the foregoing expression and to eq (39) exist for the stoichiometric components of a solution. Thus, introduction of eqs (22) and (45) and their stoichiometric analogues into eq (44) yields

$$\begin{aligned} G^{ex} = &\{\sum_{i=1}^{N_s} \hat{n}_i \hat{G}_i^{ex}\} \\ &+ \{n_1[\hat{G}_1^{o} - RT(\sum_{i=2}^{N_s} \hat{m}_i/m\dagger)] \\ &+ \sum_{i=2}^{N_s} \hat{n}_i(\hat{G}_i^{o} + RT\,\ell n \hat{m}_i)\} \\ &- \{n_1[G_1^{o} - RT(\sum_{\ell=2}^{N_c} \nu_\ell m_\ell/m\dagger)] \\ &+ \sum_{\ell=2}^{N_c} [\nu_{\ell c} m_\ell (G_{\ell c}^{o} + RT\,\ell n \nu_{\ell c} m_\ell) \\ &+ \nu_{\ell a} m_\ell (G_{\ell a}^{o} + RT\,\ell n \nu_{\ell a} m_\ell)]\} \end{aligned} \tag{46}$$

Note that $G_i^{o} = \hat{G}_i^{o}$ in the above equation.

The three terms in { } on the right side of eq (46) correspond, respectively, to $\hat{G}^{ex}$, $\hat{G}^{id}$, and G^{id}. Inspection of the terms for $\hat{G}^{id}$ shows that the differences between these quantities involve two factors: 1) a difference in Gibbs energies, i.e., G_i^{o} terms multiplied by n_i and $\hat{n}_i$, and 2) entropic terms, i.e., the $(RT\Sigma n_i\,\ell n m_i)$ terms for the solute particles and the $(RT\Sigma m_i)$ terms for the solvent. If one views $\hat{G}^{ex}$ as the electrostatic or ionic contribution to G^{ex}, the stoichiometric excess Gibbs energy is seen to also consist of energetic and entropic contributions which are formally accounted for with this model. While eq (46) could be used to compute G^{ex} directly, it is numerically preferable to use the computational scheme outlined earlier (see fig. 1).

In this paper, two different expressions have been used for $\hat{\gamma}_i$ (see eqs (5) and (6)). While classical thermodynamics has little to say about the correctness of either of these or any other choices for $\hat{\gamma}_i$, it does impose one important constraint on such a choice, namely that

$$(\partial \hat{G}_i^{ex}/\partial \hat{n}_j)_{T,p,n_{j\neq i}} = (\partial \hat{G}_j^{ex}/\partial \hat{n}_i)_{T,p,n_{i\neq j}} \tag{47}$$

or equivalently,

$$(\partial\, \ell n\, \hat{\gamma}_i/\partial \hat{n}_j)_{T,p,n_{j\neq i}} = (\partial\, \ell n\, \hat{\gamma}_j/\partial \hat{n}_i)_{T,p,n_{i\neq j}} \tag{48}$$

Thus, while it is tempting to try to assign a different value of B or b to each species in a solution in eqs (5) and (6), respectively, to do so would violate eqs (47) and (48). However, the extension of eqs (5) and (6) using eq (7) does not violate this thermodynamic constraint. Note that the use of eqs (5) or (6) for $\hat{\gamma}_i$ does not allow for the introduction of specific-ion effects attributable to long-range electrostatic interactions. These effects can be introduced by the use of eq (7). Specific-ion effects attributable to chemical equilibria are accounted forin the equilibrium part of the model. Expressions other than those in eqs (5) and (6) could be used to represent the electrostatic part of $\hat{\gamma}_i$.

The long range electrostatic contributions to the Gibbs energy properties are introduced via eq (5) or (6) and the use of an equilibrium model. Other interactions accounted for in this model include: 1) chemical interactions, 2) hydration, and 3) volume exclusion effects. The attractive chemical interactions are accounted for by the use of the equilibrium constants for the processes which describe the equilibria in solution. These processes can involve ion-pairing, complexation, and hydrolysis. The effects of hydration are accounted for either by the introduction of equilibrium constants for specific reactions involving hydration or by the use of hydration numbers for each species in solution. The use of hydration numbers reduces the value of $\hat{n}_i$ in eq (10) which in turn has consequent effects on the $\hat{m}_i$, $\hat{I}$, $\hat{\gamma}_i$, a_w, and other properties. Volume exclusion effects are represented by the B or b parameter in eqs (5) or (6). Short range repulsive forces between particles can also be accounted for using the λ_{ij} and/or μ_{ijk} parameters. It is worth noting that there are similarities in the effects that changes in certain parameters have on thermodynamic properties. Specifically, an increased value of B (or b) is similar to the introduction of a positive λ_{ij} or μ_{ijk} and also to the introduction of hydration effects. Physically this should be the case since the excluded volume for a hydrated ion is larger than for one that is not hydrated. Also, a negative λ_{ij} is similar to an association between particles i and j. The remainder of this paper will discuss the application of this model to several aqueous salt

solutions containing representative types of chemical interactions.

3. Results and Discussion

We now compare the results of calculations using this model with experimental data and examine the results of perturbing the various input parameters in the model, i.e., the single-ion activity coefficient expressions, the assumed equilibrium constants, and the assumed state of hydration of the species in solution. To do this, calculations have been made on the following aqueous electrolyte solutions: sulfuric acid, acetic acid, hydrofluoric acid, cadmium chloride, copper sulfate, and sodium carbonate.

The results of calculations on aqueous sulfuric acid are shown in figures 2 through 4, where the chemical equilibrium considered is

$$H^+(aq) + SO_4^{2-}(aq) = HSO_4^-(aq) \qquad (A)$$

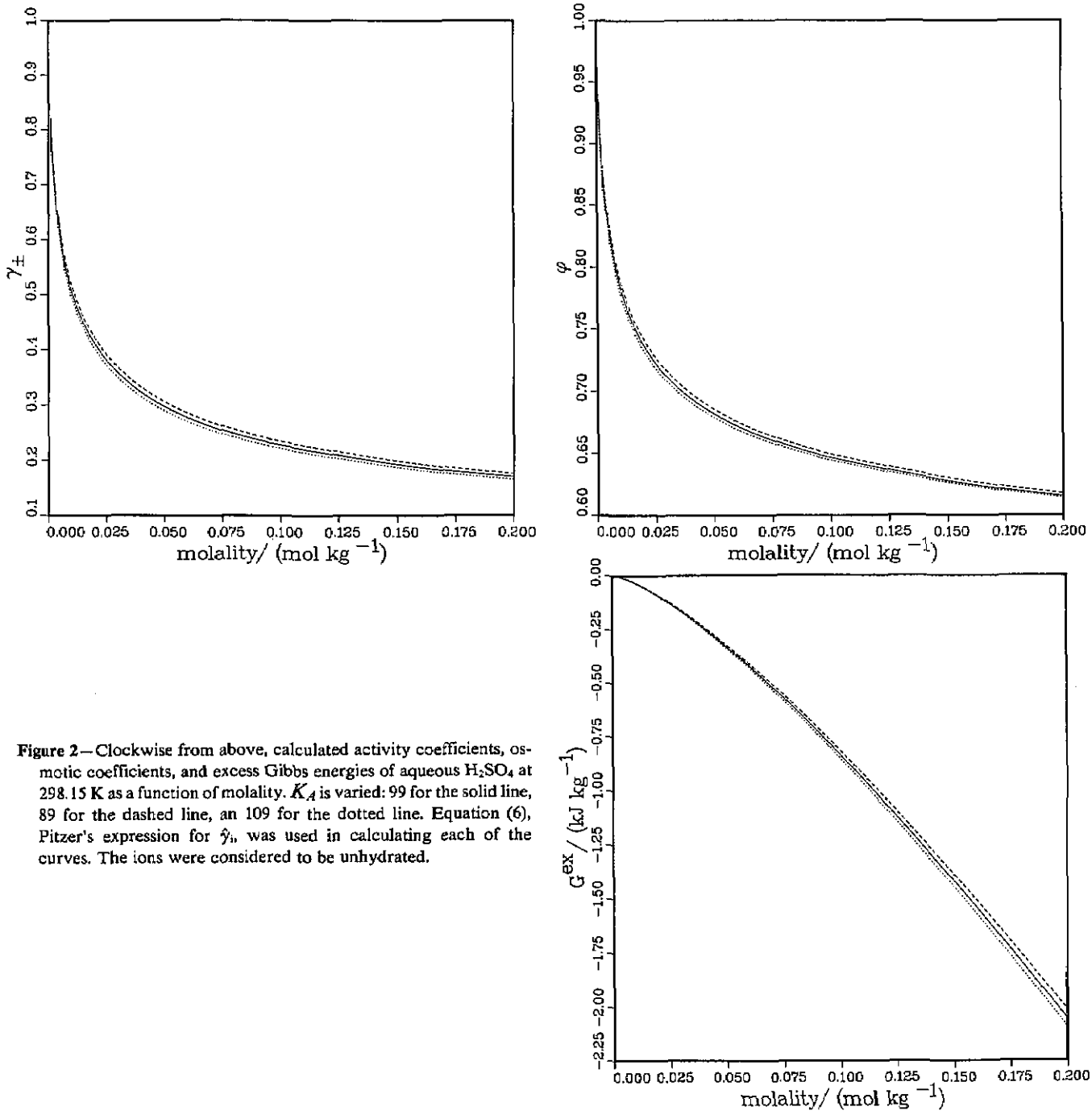

Figure 2—Clockwise from above, calculated activity coefficients, osmotic coefficients, and excess Gibbs energies of aqueous H_2SO_4 at 298.15 K as a function of molality. K_A is varied: 99 for the solid line, 89 for the dashed line, an 109 for the dotted line. Equation (6), Pitzer's expression for $\hat{y}_i$, was used in calculating each of the curves. The ions were considered to be unhydrated.

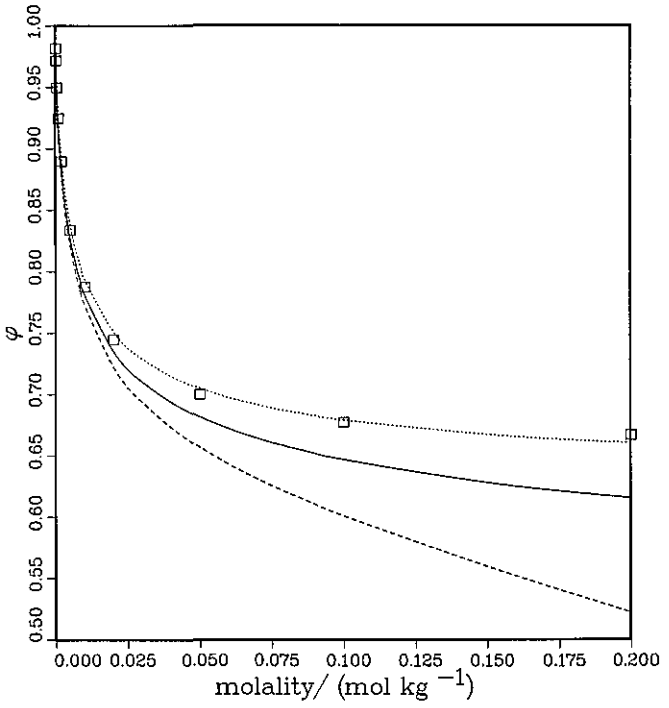

Figure 3—Comparison of calculated osmotic coefficients for aqueous H_2SO_4 at 298.15 K. The squares are the correlated values of Pitzer, Roy, and Silvester [10]. The solid line was calculated using a value of $K_A = 99$ and Pitzer's expression for $\hat{\gamma}_i$. The dashed and dotted lines were calculated using the same value of K_A and values of B equal to zero and 2.5 respectively, in a Debye-Hückel expression for $\hat{\gamma}_i$ (eq (5)). The ions were considered to be unhydrated.

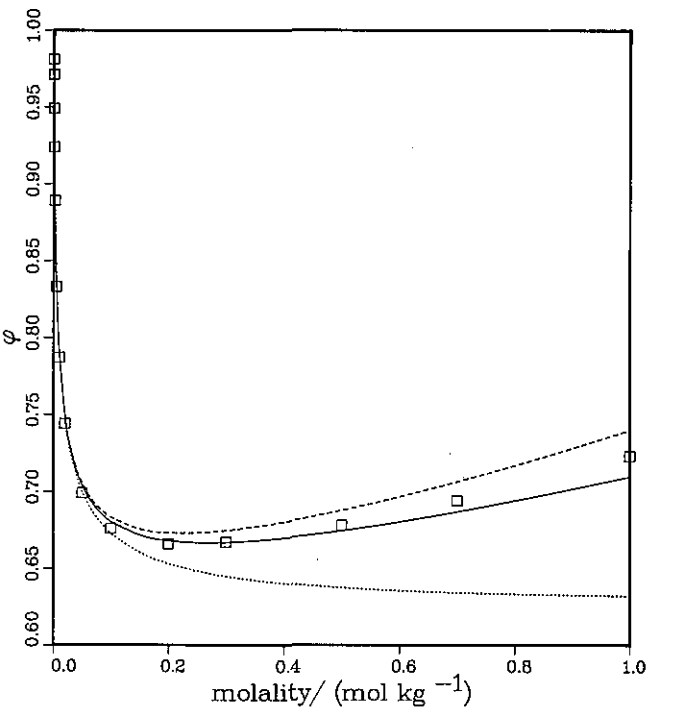

Figure 4—Calculated osmotic coefficients of aqueous H_2SO_4 at 298.15 K in which the extent of hydration of the ions is varied. All three curves were calculated using a value of 99 for K_A and a Debye-Hückel expression for $\hat{\gamma}_i$ with B equal to 2.0. The dotted line was calculated assuming that all of the ions were not hydrated. The solid and dashed line were calculated, respectively, by assuming all three ions (H^+, SO_4^{2-}, and HSO_4^-) to be hydrated with three and four waters each. The squares are from the correlation of Pitzer, Roy, and Silvester [10].

The value of K_A is 99 at 298.15 K [17]. It is seen that the calculated values of $\gamma_\pm$, ϕ, and G^{ex} are relatively insensitive to moderate variations in K_A up to molalities of 0.2 mol kg^{-1}. However, as seen in figure 3, significant changes in the osmotic coefficient are produced by perturbing the value of the B parameter. Use of a value of B equal to 2.5 in a Debye-Hückel expression for $\hat{\gamma}_i$ (see eq (5)) produces good agreement with the experimental osmotic coefficients (the squares in fig. 2d) up to a molality of $\approx$0.2 mol kg^{-1}. The effects of variations in hydration numbers is shown in figure 4. The minimum in the osmotic coefficient curve cannot be produced by variation in the B parameter, but, as seen in figure 4, a minimum is observed when hydration is introduced.

The equilibrium considered in the description of aqueous acetic acid (HAc) is

$$H^+(aq) + Ac^-(aq) = HAc^0(aq) \quad ,K = 5.96 \times 10^4 \quad \text{(B)}$$

For aqueous hydrofluoric acid, the equilibria are

$$H^+(aq) + F^-(aq) = HF^0(aq) \quad ,K = 1.44 \times 10^3 \quad \text{(C)}$$

and

$$HF^0(aq) + F^-(aq) = HF_2^-(aq) \quad ,K = 2.71 \quad \text{(D)}$$

For aqueous cadmium chloride the stepwise equilibria considered are:

$$Cd^{2+}(aq) + Cl^-(aq) = CdCl^+(aq) \quad ,K = 85 \quad \text{(E)}$$

$$CdCl^+(aq) + Cl^-(aq) = CdCl_2^0(aq) \quad ,K = 2.71 \quad \text{(F)}$$

$$CdCl_2^0(aq) + Cl^-(aq) = CdCl_3^-(aq) \quad ,K = 0.53 \quad \text{(G)}$$

and

$$CdCl_3^-(aq) + Cl^-(aq) = CdCl_4^{2-}(aq) \quad ,K = 4.3 \times 10^{-4} \quad \text{(H)}$$

The equilibria considered for aqueous copper sulfate are:

$$Cu^{2+}(aq)+SO_4^{2-}(aq)=CuSO_4^0(aq) \quad ,K=250 \quad (I)$$

$$CuSO_4^0(aq)+Cu^{2+}(aq)=Cu_2SO_4^{2+}(aq) \quad ,K=5 \quad (J)$$

$$CuSO_4^0(aq)+SO_4^{2-}(aq)=Cu(SO_4)_2^{2-}(aq) \quad ,K=5 \quad (K)$$

For aqueous sodium carbonate the equilibria considered are:

$$CO_3^{2-}(aq)+H_2O(\ell)$$

$$=HCO_3^-(aq)+OH^-(aq) \quad ,K=2.16\times10^{-4} \quad (L)$$

$$HCO_3^-(aq)=CO_2^0(aq)+OH^-(aq) \quad ,K=2.34\times10^{-8} \quad (M)$$

and

$$H_2O(\ell)=H^+(aq)+OH^-(aq) \quad ,K=1.0\times10^{-14} \quad (N)$$

All of the above equilibrium constants refer to a temperature of 298.15 K with the exception of the value for process (B) which refers to 273.15 K. The Gibbs energies of formation given in the NBS Tables of Chemical Thermodynamic Properties [17] were used to calculate the above values for equilibria (C), (D), (K), (L), and (M). The value for process (B) was calculated from the data for acetic acid tabulated by Larson and Hepler [19]; the values for processes (E), (F), (G), and (H) are those given by Reilly and Stokes [12]; and the values for processes (I), (J), and (K) are those given by Pitzer [9]. The Debye-Hückel constants recommended by Clarke and Glew [20] were used in all calculations.

The results of the calculations are shown in figures 5 through 9. For acetic acid, since the species ionic strength ($\hat{I}$) is very low (it has a value of 0.044 mol kg^{-1} at Ist=1.0 mol kg^{-1}), the choice of the expression for $\hat{\gamma}_i$ makes very little difference. Near agreement with the experimental osmotic coefficients is obtained to a molality of $\approx$0.2 mol kg^{-1}. The difference between the measured osmotic coefficients and the calculated ones

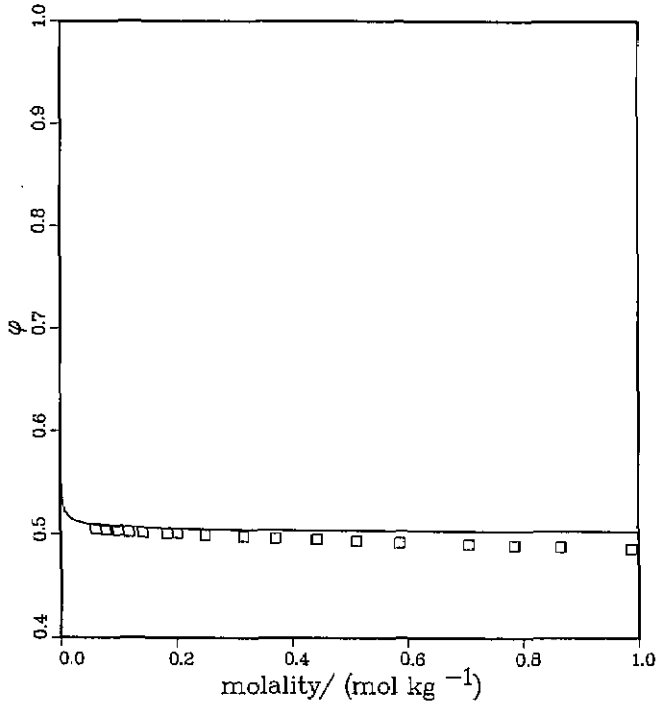

Figure 5—The osmotic coefficients of aqueous acetic acid at 273.15 K. The squares are the experimental osmotic coefficients reported by Harris, Thompson, and Wood [21]. The solid curve was calculated using a value of $K_B=5.96\times10^4$ which was obtained from the values of $\Delta G°$, $\Delta H°$, and ΔC_p^s for process (B) given by Larson and Hepler [19]. The solid curve was also calculated using either Pitzer's $\hat{\gamma}_i$ or a Debye-Hückel $\hat{\gamma}_i$ where B varied from zero to 2.0. In this figure and in all subsequent ones, the ions were considered to be unhydrated.

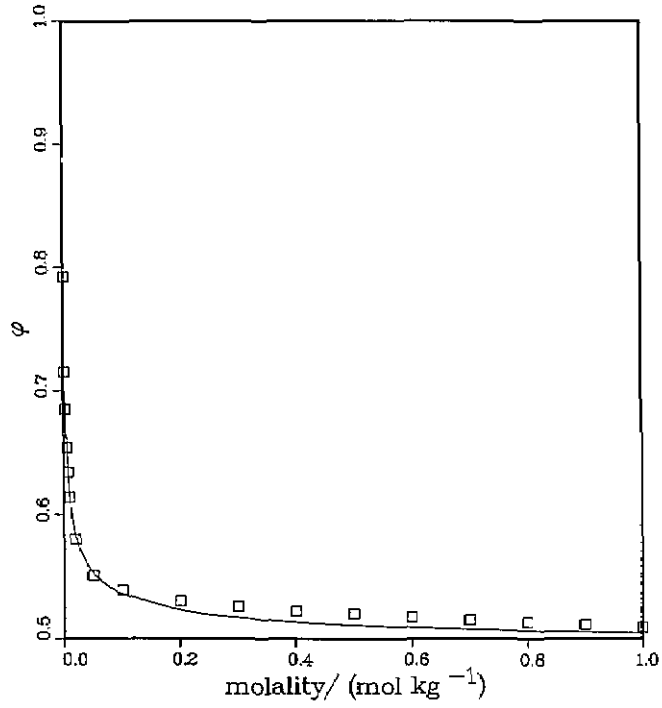

Figure 6—The osmotic coefficients of aqueous HF at 298.15 K. Values of $K_c=1442$ and $K_D=2.63$ were used to calculate the solid curve together with Pitzer's expression for $\hat{\gamma}_i$. The squares are from the correlation of Hamer and Wu [22].

can be attributed to the formation of dimers and trimers of acetic acid [21] and cannot be explained either by the introduction of hydration or by the use of different B parameters in eq (5) or by the choice of a different expression for $\hat{\gamma}_i$.

For aqueous HF, $CdCl_2$, $CuSO_4$, and Na_2CO_3, agreement of calculated with measured properties can be obtained to molalities between 0.6 and 1.0 mol kg^{-1} by the variation of the B parameter in eq (5) and, for the case of $CdCl_2$, using only eq (6) for $\hat{\gamma}_i$. Neither the use of eq (5) nor eq (6) is able to produce the minima in the calculated values of ϕ or $\gamma_\pm$ which is observed for many electrolyte solutions. These minima can be produced, however, either by the introduction of hydration or by the use of eq (7) to extend the equations for $\hat{\gamma}_i$. It should be noted that for Na_2CO_3 solutions the osmotic coefficient does not approach the usual limit of unity as m^{st} approaches zero mol kg^{-1}; instead it approaches a value of 1.395 [14]. This is a consequence of eq (39) and the presence of equilibria (L), (M), and (N).

Calculated values of $\delta_\pm$ are shown in figure 10. The fact that values of $\delta_\pm$ for acetic acid and for copper sulfate are essentially unity is attributable to a very near cancellation of terms in eqs (25) and (36). It should be noted that the value of $\delta_\pm$ for Na_2CO_3, unlike the other systems shown in figure 10, does not approach a value of unity as the molality approaches zero mol kg^{-1}; the minimum value of $\delta_\pm$ for Na_2CO_3 occurs at a molality of 0.0040 mol kg^{-1}. While there are presently no experimental values of $\delta_\pm$ available with which to compare our calculated values, this property is potentially measureable [24].

In summary, an equilibrium model for aqueous solutions has several important applications: 1) the Gibbs energy properties can be reliably estimated at low molalities if the appropriate equilibrium constants are known, 2) an equation of state can be generated which is appropriate for a particular type of solution, 3) amounts of species in a given solution can be calculated, 4) single-ion activities can be calculated, and 5) as was done here, effects of variations in the equilibria, state of hydration, and electrostatic contributions to the Gibbs energy properties can be investigated. A natural extension of this model is the calculation of enthalpies, heat capacities, and volumes of aqueous solutions.

The author thanks Drs. Graham Morrison, Ralph L. Nuttall, and, in particular, Robert H. Wood, for useful and stimulating discussions on the topics of this paper.

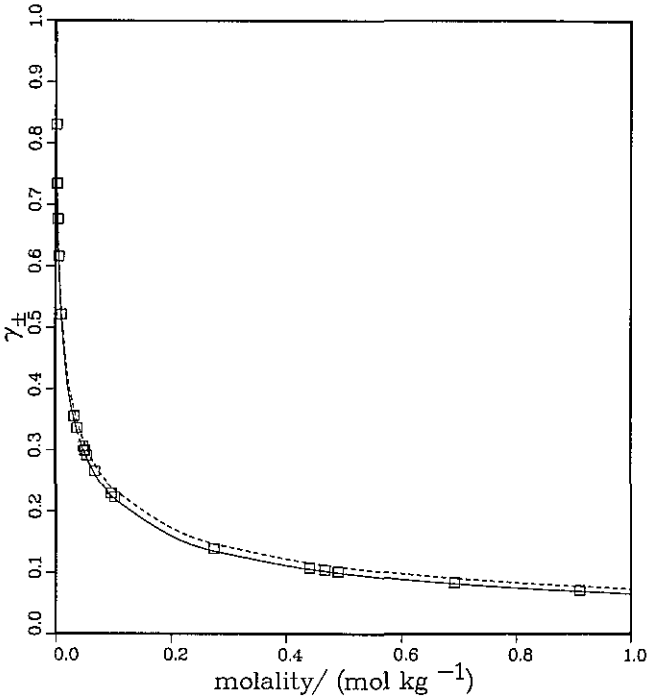

Figure 7—The activity coefficients of aqueous $CdCl_2$ at 298.15 K. The successive formation constants given by Reilly and Stokes [12] were used in doing the calculations. The solid line was calculated using Pitzer's expression for $\hat{\gamma}$i and the dashed line was calculated using the Debye-Hückel $\hat{\gamma}_i$ with B set equal to 2.0. The squares are based on the measurements of Reilly and Stoke [12].

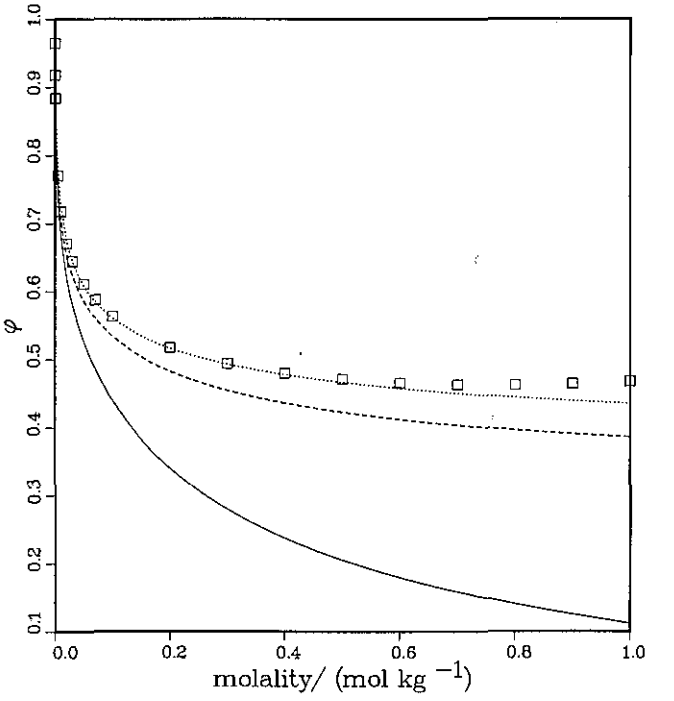

Figure 8—The osmotic coefficients of aqueous $CuSO_4$ at 298.15 K. The squares are the experimental data of Miller et al [23]. The three curves were obtained using values of $K_E=250$ and $K_F=K_G=5$. The solid line was calculated using Pitzer's expression for $\hat{\gamma}_i$, the dashed and dotted lines were obtained using the Debye-Hückel $\hat{\gamma}_i$ with B set equal to 2.0 and 5.0, respectively.

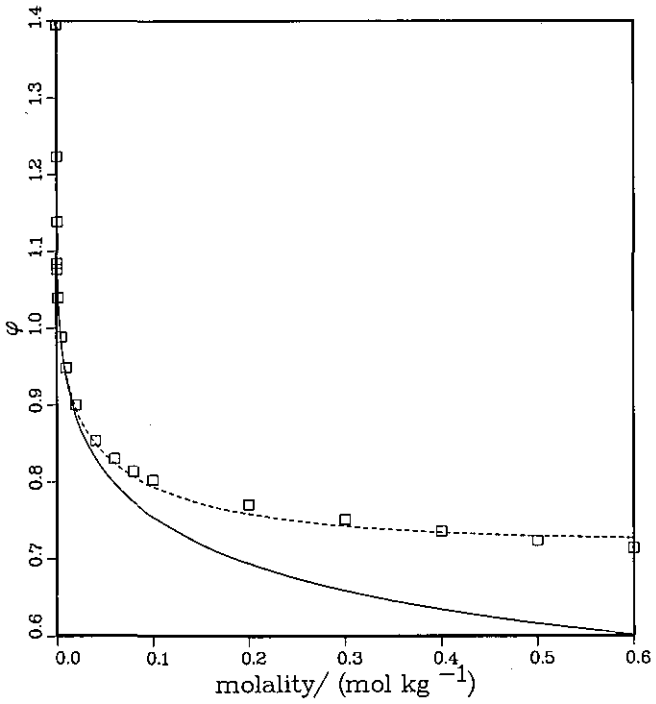

Figure 9—The osmotic coefficients of aqueous Na_2CO_3 at 289.15 K. The squares are from the correlation of Vanderzee [14]. The solid line was calculated using Pitzer's expression for $\hat{\gamma}_i$ and values of K_L, K_M, and K_N from reference [17]. The dashed line was calculated using these same values of K and a Debye-Hückel $\hat{\gamma}_i$ with B equal to 1.0.

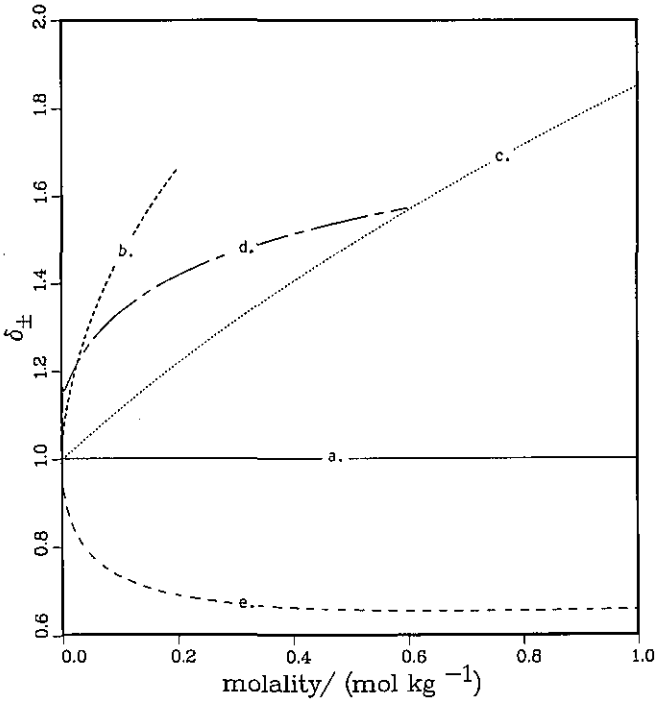

Figure 10—Calculated values of $\delta_\pm$ for several electrolyte solutions: (a) corresponds to acetic acid and to $CuSO_4$, (b) corresponds to H_2SO_4, (c) corresponds to HF; (d) corresponds to Na_2CO_3; and (e) corresponds to $CdCl_2$. These curves were calculated using the values of the equilibrium constants cited above (a value of K_A equal to 99 was used). Pitzer's expression for $\hat{\gamma}_i$ (eq (6)) was used for acetic acid, hydrofluoric acid, and cadmium chloride. The Debye-Hückel expression for $\hat{\gamma}_i$ (eq (5)) was used for sulfuric acid, copper sulfate and sodium carbonate with respective values of B equal to 2.5, 5.9, and 1.0.

References

[1] Brown, P. G. M.; Prue, J. E.; A Study of Ionic Association in Aqueous Solutions of Bi-bivalent Electrolytes by Freezing-point Measurements. Proc. Roy. Soc. London Sect. A **232**, 320—336 (1955).

[2] Cook, R. O.; Davies, A.; Staveley, L.A. K.; A Thermodynamic Study of Ion Association in Aqueous Solutions of Zinc Fluoride. J. Chem. Thermodyn. **3**, 907—913 (1971).

[3] Gardner, A. W.; Gluekauf, E.; Ionic Association in Aqueous Solutions of Bi-valent Sulphates. Proc. Roy. Soc. London Ser. A **313**, 131—147 (1969).

[4] Glueckauf, E.; The influence of Ionic Hydration on Activity Coefficients in Concentrated Electrolyte Solutions. Trans. Faraday Soc. **51**, 1235—1244 (1955).

[5] Glueckauf, E.; Further Studies of 2:2 Electrolytes: Osmotic and Activity Coefficients. Proc. Roy. Soc. London Ser. A **351**, 471—479 (1976).

[6] Hamer, W. J.; Wu, Y. C.; The Activity Coefficients of Hydrofluoric Acid in Water from 0 to 35°C; J. Res. Natl. Bur. Stand. (U.S.) **74A**, 761—768 (1970).

[7] Pan, C. F; Determination of Hydration Number of an Electrolyte by Vapor Pressure Measurements; J. Phys. Chem. 82, 2699—2701 (1978).

[8] Peiper, J. C.; Pitzer, K. S.; Thermodynamics of Aqueous Carbonate Solutions Including Mixtures of Sodium Carbonate, Bicarbonate, and Chloride; J. Chem. Thermodyn. **14**, 613—638 (1982).

[9] Pitzer, K. S.; Thermodynamic Properties of Aqueous Solutions of Bivalent Sulphates; J. Chem. Soc. Faraday Trans. 2 **68**, 101—113 (1972).

[10] Pitzer, K. S.; Roy, R. N.; Silvester, L. F.; Thermodynamics of Electrolytes. 7. Sulfuric Acid; J. Am. Chem. Soc. **99**, 4930—4936 (1977).

[11] Pitzer, K. S.; Silvester, L. F.; Thermodynamics of Electrolytes VI. Weak Electrolytes Including H_3PO_4; J. Solution Chem. **5**, 269—278 (1976).

[12] Reilly, P. J.; Stokes, R. H.; The Activity Coefficients of Cadmium Chloride in Water and Sodium Chloride Solution at 25°; Aust. J. Chem. **23**, 1397-1405 (1970).

[13] Robinson, R. A.; Stokes, R. H.; Electrolyte Solutions, London: Butterworths; 1959; p. 239 and 240.

[14] Vanderzee, C. E.; Thermodynamic Properties of Solutions of a Hydrolyzing Electrolyte: Relative Partial Molar Enthalpies and Heat Capacities, Solvent Activities, Osmotic Coefficients, and Solute Activity Coefficients of Aqueous Sodium Carbonate; J. Chem. Thermodyn. **14**, 1051—1067 (1982).

[15] Wood, R. H.; Lilley, T. H.; Thompson, P. T.; Rapidly Converging Activity Expansions for Representing the Thermodynamic Properties of Fluid Systems: Gases, Nonelectrolyte Solutions, Weak and Strong Electrolyte Solutions; J. Chem. Soc. Faraday Trans. 1 **74**, 1301—1323 (1978).

[16] Frank, H. S.; Single Ion Activities and Ion-Solvent Interaction in Dilute Aqueous Solutions; J. Phys. Chem. **67**, 1554-1558 (1963).

[17] Wagman, D. D.; Evans, W. H.; Parker, V. B.; Schumm, R. H.; Halow, I.; Bailey, S. M.; Churney, K. L.; Nuttall, R. L.; The NBS Tables of Chemical Thermodynamic Properties; J. Phys. Chem. Ref. Data **11**, Supplement No. 2 (1982), 392 pages.

[18] Pitzer, K. S.; Theory: Ion Interaction Approach, in 'Activity Coefficients in Electrolyte Solutions,' R. M. Pytkowicz, editor; Boca Raton, FL, CRC Press: 1979; p. 157—208.

[19] Larson, J. W.; Hepler, L. G.; Heats and Entropies of Ionization, in 'Solute-Solvent Interactions'; J. F. Coetzee and C. D. Ritchie, editors; New York: Marcel Dekker; 1969; p. 1—44.

[20] Clarke, E. C. W.; Glew, D. N.; Evaluation of Debye-Hückel Limiting Slopes for Water Between 0 and 150°C; J. Chem. Soc. Faraday Trans. 1 **76**, 1911-1916 (1980).

[21] Harris, A. L.; Thompson, P. T.; Wood, R. H.; Freezing Point and Enthalpies of Dilution of Aqueous Formic, Acetic, Propionic, and Butyric Acids. Free Energies and Enthalpies of Solute-Solute Interactions; J. Solution Chem. **9**, 305-325 (1980).

[22] Hamer, W. J.; Wu, Y. C.; Osmotic Coefficients and Mean Activity Coefficients of Uni-univalent Electrolytes in Water at 25°C; J. Phys. Chem. Ref. Data **1**, 1047-1100 (1972).

[23] Miller, D. G.; Rard, J. A.; Eppstein, L. B.; Robinson, R. A.; Mutual Diffusion Coefficients, Electrical Conductances, Osmotic Coefficients, and Ionic Transport Coefficients ℓ_{ij} for Aqueous $CuSO_4$ at 25°C; J. Solution Chem. **9**, 467—495 (1980).

[24] Goldberg, R. N.; Frank, H. S.; Liquid Junction Potentials and Single-Ion Activities by Computer Simulation. I. The Concentration Cell with Transference; J. Phys. Chem. **76**, 1758—1762 (1972).

JOURNAL OF RESEARCH of the National Bureau of Standards
Vol. 89, No. 3, May-June 1984

An Absolute Electric Current Probe Based on the Faraday Effect

W. Caton and J. Katzenstein
Maxwell Laboratories, Inc., San Diego, CA 92123

Accepted: April 24, 1984

This paper describes the design, construction, and testing of a probe for the measurement of electric current in a circuit. This measurement is performed by using Faraday rotation produced in a beam of polarized light that encircles the current-carrying conductor. Such a probe is an absolute instrument whose calibration only depends upon the Verdet constant of the rotative medium and is independent of the dimensions or positions of the light path relative to the current. The time resolution of the probe is the optical transit time about the closed path and can in practice be reduced to a few nanoseconds.

Key words: absolute instrument; electric current; Faraday effect; measurement; polarized light; Verdet constant.

1. Introduction

The Faraday effect, known for over a century, has been applied extensively in the measurement of magnetic fields and, more recently, in the measurement of electric current. A Faraday effect current probe offers several advantages, especially for the current measurements in high-voltage circuits. Since measurement information is conveyed by variations in the intensity of an optical signal, the probe can be perfectly insulated electrically from the measurement and recording circuitry either by the free space propagation of a light beam or the transmission of the signal via fiber optics. Indeed the probe need not interrupt the circuit in which the current is being measured; it need only be close enough to be affected in a controlled way by the magnetic field produced by the current. A second advantage of the Faraday effect current probe is the possibility of its being an absolute instrument because calibration can be made to depend solely upon the Verdet constant of the rotative medium. For diamagnetic media, the Verdet constant is determined by the dispersion curve of the medium and does not depend upon temperature.

A great deal of work has been done to develop Faraday effect current probes. Hebner et al. summarized this work up to 1977 [1][1]. The difficulties with the current probes can be summarized as owing to 1) calibration errors and, 2) limited dynamic range, signal-to-noise ratio, and the effects of optical detector sensitivity variations.

The principal source of the first set of difficulties lies in the fact that the magnetic field arising from the current flow in an arbitrary circuit, in general, has a spatial variation. Hence, the calibration of the probe involves geometric factors such as the shape and dimensions of the probe and its position relative to the circuit. The second set of difficulties stems from the relatively small value of the Verdet constant for most media and the concomitant small value of the rotation for currents of the magnitudes encountered in electric utility

About the Authors, Paper: While W. Caton remains associated with Maxwell Laboratories, J. Katzenstein is now with the University of California at Irvine. The work on which they report, performed while both were at Maxwell, was carried out for the Defense Nuclear Agency, U.S. Department of Defense, under contract DNA001-79-C-0019.

[1]Figures in brackets indicate literature references at the end of this paper.

transmission lines. The schemes [1] proposed to improve this situation, such as null-seeking feedback devices, etc., generally lead to expensive, complicated, and less than satisfactory devices. In spite of these problems, satisfactory Faraday probes for use on utility transmission lines have been realized [2,3,4].

The geometric factors in the probe calibration can be eliminated by designing the optical path in the rotative medium so that it encircles the current. Since the Faraday rotation angle θ is proportional to the line integral of the magnetic induction $\mathbf{B}$ along the path l, we can write for a closed light path

$$\theta = V \oint \mathbf{B} \cdot \mathbf{d}l \tag{1}$$

where V, the constant proportionality, the so-called Verdet constant, is characteristic of the rotative medium and is usually expressed in the units of minutes of arc per gauss-centimeter. From the circuital statement of Ampere's law, we replace the circuital integral $\oint \mathbf{B} \cdot \mathbf{d}l$ by $\frac{4\pi i}{10}$ where i is the current in amperes that is enclosed by the path of integration. The resulting Faraday rotation is thus

$$\theta = \frac{4\pi}{10} Vi. \tag{2}$$

The Faraday rotation in such a current probe depends only on the Verdet constant of the rotative medium; geometric factors do not enter. Current probes based on this principle have been developed [3,4], using optical fibers as the rotative medium. Unfortunately, optical fibers which rigorously preserve the state of polarization transversing them are at present beyond the state of the art.[2] Since the Verdet constant of the fiber core material (essentially fused quartz) is very small, a large number of turns of the fiber around the conductor is needed to obtain a measureable rotation which greatly increases the stray birefringence due to fiber strain and curvature. To minimize these effects, the radius of curvature of the fiber turns is kept as large as possible which increases the overall size of the probe. As the optical transit time of the fiber coil gives the time resolution of the current variations such a fiber optic probe would be unsuitable for measuring fast-rising currents. In spite of these problems, however, Faraday effect current monitors have been developed for use on high voltage utility transmission lines and offer a cost-effective alternative to conventional current transformers. At the relative low frequencies present in these lines, the decreased time resolution of these fiber optic probes poses no problem.

The second set of problems, dynamic range, signal-to-noise ratio etc., can be addressed by designing the probe so that the number of complete Faraday rotations at the maximum value of current is large. In our work this required no particular effort as the peak current was in the mega-ampere range. The advantage of this mode of operation can be seen from the following discussion.

The light entering the Faraday probe is rendered plane polarized by use of a suitable device (unless a laser emitting plane polarized light is used as a source) and the emerging light passes through a second polarizer or analyzer before entering the detector.

The intensity of light on the detector for an incident intensity of I_0 is given by

$$I = I_0 \cos^2(\theta + \chi) \tag{3}$$

where χ is the angle between the transmission axes of the polarizer and analyzer.

Two different methods of handling Faraday effect signals can be used depending upon whether the value $\theta(i)$ at peak current is very much less than π.

In the latter case, the usual practice is to make use of a differential analyzer such as a Wollaston prism which separates the entering light into two beams of intensity I_1 and I_2 which are polarized orthogonally to each other [4,5]. The analyzer is oriented at 45° with respect to the transmission axis of the polarizer. The intensities of the transmitted beams for a Faraday rotation angle of the θ are

$$I_1 = I_0 \cos^2(\theta - 45°)$$

$$I_2 = I_0 \cos^2(\theta + 45°). \tag{4}$$

The sum and difference of these two intensities and their quotient are computed giving

$$s = \frac{I_1 - I_2}{I_1 + I_2} = \sin 2\theta, \tag{5}$$

or using eq (2) we have for $\theta \ll \pi$

$$r = \frac{8\pi}{10} Vi. \tag{6}$$

[2]Presently single mode optical fibers have been produced with different propagation velocities for right- and left-hand polarized light. [9] Since these two modes of propagation have different phase velocities, there is no intermixing of the modes due to fiber imperfections and the relative phase of the two circular modes of propagation is preserved. If such fibers could be made with cores of high Verdet constant glass which should in principle pose no difficulty, then a Faraday rotation current probe making use of only a few turns could be produced with a concomitant low transit time and short time resolution.

Note that the result is independent of the intensity of the light or the sensitivities of the two detectors provided that the latter are equal.

An alternative method of measurement useful when $\theta(i_{max}) \gg \pi$ is to use crossed or parallel analyzers ($X=0$ or $\pi/2$). The signal is then

$$I(t)=I_0 \sin^2\theta(t) \text{ Crossed polarizers}$$

$$I(t)=I_0 \cos^2\theta(t) \text{ Parallel polarizers} \quad (7)$$

or

$$I(t)=I_0\frac{1\mp\cos 2\,\theta(t)}{2}. \quad (7a)$$

The upper sign is for crossed polarizers which, using eq (2), gives

$$I(t)=I_0\left[\frac{1-\cos\left(\frac{8\pi}{10}Vi(t)\right)}{2}\right]. \quad (8)$$

The signal given by eq (8) can be inverted numerically to obtain i as a function of t.

The accuracy is determined by the precision with which the phase of the cosine can be determined from the record of $\theta(t)$ which depends upon the signal-to-noise ratio. If we call this phase uncertainty $\Delta\phi$, then the relative error ϵ is

$$\epsilon=\frac{\Delta\phi}{\pi N+\phi}\approx\frac{\Delta\phi}{N\pi} \quad (9)$$

where N is the total number of cycles of Faraday rotation. Thus even though a relatively large value of $\Delta\phi$ is obtained due to a poor signal-to-noise ratio, the error in the current measurements can be made small by making N large. It is assumed, however, that $\Delta\phi$ is not so large that a change of sign of the time derivative of the phase cannot be detected. Such a reversal in $\frac{d\phi}{dt}$ occurs when i attains an extremum.

Variations in peak amplitudes of the Faraday signal due to noise, source intensity, detector sensitivity, or transmission fluctuations can be averaged out by normalizing all maxima except those associated with the excess fraction of a cycle. These effects will thus only affect the accuracy with which the excess fraction can be measured.

If the value of i_π can be made sufficiently small so that $i_\pi=\Delta i$ the allowable current error, then the signals can be handled purely by digital techniques. The value of the current can thus be evaluated by simple pulse counting. The reversal in sign of $\frac{d\phi}{dt}$ can be detected by using a Wollaston prism or similar analyzer crossed with the input polarization direction to obtain the two outputs given by eq (7) thus providing a phase reference. Such digital processing would eliminate most of the second class of problems in the use of Faraday probes. The problem is now that of reducing i_π to a sufficiently low value to obtain a probe of required accuracy for currents of the magnitude encountered in electric power transmission. This in turn requires the development of polarization preserving optical fibers of high Verdet constant (see footnote 2).

2. Design of a Faraday Current Probe

We have designed and tested a Faraday current probe based on the principle of the preceding section. It is designed to measure currents of up to 4 MA rising to their maximum value in times of the order of 50 ns.

Even if polarization preserving fibers were available their use in this application would be impossible since the low Verdet constant of these fibers would require many turns. The resulting long optical transit time and poor time resolution would obscure completely the details of the current waveform. In addition, only a few cycles of Faraday rotation would be obtained so the relative error given by eq (9) would be large.

We selected as the Faraday rotative medium a high density flint glass, Schott type SF-58. This glass has a Verdet constant of 0.082 min/gauss-cm and a refractive index of 1.907 at the wavelength of the helium-neon laser, 6328 Å. This glass has a very low residual birefringence and a high transmission for the He-Ne laser wavelength. An alternative choice considered was one of the terbium-doped glasses. These glasses have a large Verdet constant of the order of 0.2 min/gauss-cm. We decided against using one of these glasses, because 1) they are very costly and, 2) their Verdet constants vary with temperature since the glasses are paramagnetic. While the diamagnetic glasses such as SF-58 have lower Verdet constants, the values of these constants are approximately constant, independent of temperature variations. As the current required to produce a rotation of 180°, i_π, is $\sim 10^5$ A for SF-58, the number of cycles of Faraday rotation at the expected peak currents of 2-to 4 MA will be 20 or more. Thus a larger value of Verdet constant, while useful for reducing the relative error, was really not needed for this application.

The closed light path within the rotative medium was realized by multiple total internal reflection (TIR) within the rotative medium. As is well known, a TIR introduces a phase shift between the components of polarization parallel and perpendicular to the plane of inci-

dence. Hence, if the incident light is plane-polarized, the reflected light becomes elliptically polarized. This ellipticity would lead to a Faraday signal in which the amplitude as well as the phase varied with time unlike the simple expression, eq (8). The numerical inversion of the Faraday signal would thus be more complicated and the effects of noise more severe.

A very simple solution to this problem has been found by Kard [6]. He showed that a quarter-wave coating (corrected for angle of incidence) on the TIR interface whose refractive index was the geometric mean of that of the substrate and the external medium (usually air or vacuum) would compensate the phase shift and the reflected light would remain plane polarized if the incident light was polarized. This solution is applicable only to cases for which the angle of incidence on the interface is less than the critical angle, i.e., some of the light must enter the coating and be totally reflected from the coating-vacuum interface. For the SF-58 glass of refractive index 1.907, a magnesium fluoride coating of refractive index 1.38 is almost a perfect match and is a very satisfactory material for making a durable optical coating of very precisely controlled thickness. The critical angle of the coating-substrate interface is arcsin $(1.38)^{-1}$ or 46.4°. Thus a coat of MgF_2 will effectively compensate the ellipticity for TIR at an angle of incidence of 45°. We have tested such coatings and found that a very good null of the reflected light can be obtained with an analyzer for any arbitrary azimuth of the incident polarization.

Another fundamental problem in the design of a closed-optical-path Faraday rotator is that of mirror reversion. As is well known, the rotation sense of light reflected in a mirror is changed. Thus a magnetic field in the same direction will produce rotation in the opposite sense after mirror reflection. Indeed it was just this property that enabled Faraday to discover the very small effect that bears his name with the relatively feeble magnetic fields available to him in 1845. The sense of the rotation of the plane of polarization induced by a magnetic field changes sign when the relative direction of the field and the light propagation is changed. Thus if the light after traversing the rotative medium is reflected from a mirror back along the field direction, the change of sense of rotation due to mirror reversion is compensated by the reversed sense of the Faraday effect and the two rotations add rather than cancel as happens in the case of ordinary optical activity. Thus Faraday was able to amplify the effect by multiple passes between mirrors and obtain a measurable rotation with a field of only several hundred gauss.

In our probe, however, the relative direction of the field and the light propagation remains unchanged. Thus if we number the segments of the light path between reflections in order, we can write for the total rotation

$$\theta = V\left[\int \mathbf{B}\cdot\mathbf{d}l - \int \mathbf{B}\cdot\mathbf{d}l\right]. \qquad (10)$$

odd-numbered segments; even-numbered segments

Hence, in order to realize the Faraday rotation appropriate to the current linking the light path, it is necessary to design the probe so that the even-numbered segments of the light path are as short as possible and oriented as nearly as possible normal to the magnetic field direction. The contribution of the second integral in eq (10) can then be neglected.

Figure 1 is an isometric projection of the Faraday rotation probe design that meets these requirements. It

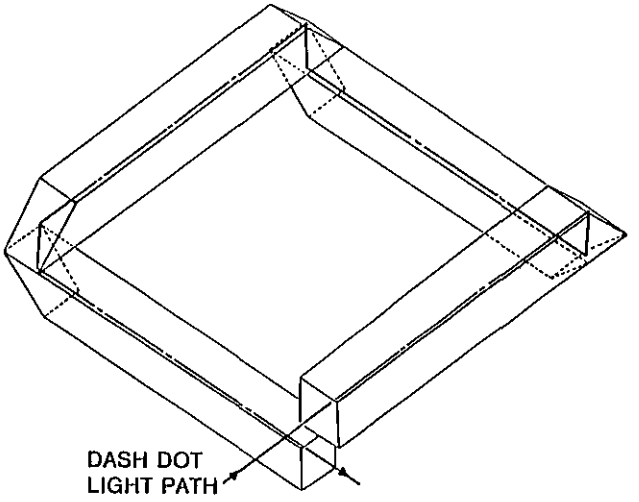

Figure 1—Optical path of Faraday effect current probe.

consists of four rectangular parallelepipeds of SF-58 glass; two of which have surfaces at each end at 45° to the direction of the edges, and two have 90° faces at one end and 45° inclined faces at the opposite end. The latter pieces form the initial and final segments of the optical path, the 90° faces being the entrance and exit windows. The four pieces are cemented or clamped together as shown. The odd-numbered segments form a closed path in the form of a square when projected into a common plane. The even-numbered segments are the short segments normal to the plane of the ring between successive 45° faces. These segments are much shorter than the odd-numbered segments forming the projected closed square. Furthermore, if the path of the current is rigorously perpendicular to the plane of the ring, the magnetic field will be normal to the short even-numbered segments, and the contribution of the second integral in eq (10) will be zero.

When dealing with rapidly varying currents, the contribution of the even-numbered segments can also be reduced to zero by enclosing the ring in a conducting shell with an equatorial slit insulated against the voltage developed by the flow of skin currents in the shell. Provided this insulation requirement can be met and the skin depth of surface currents is less than the shell thickness, only equatorial components of magnetic field can penetrate the shell, and the condition of zero contribution of the even-numbered segments can be maintained for any orientation of the plane of the ring. The situation is quite similar to that encountered in the use of a Rogowski coil; an error in the current measurement results from the inclination of the plane of an unshielded Rogowski coil with respect to the current. This error can likewise be eliminated by shielding the coil by a conducting shell with an equatorial slit.

The 45° inclined faces are all coated with quarter-wave MgF_2 coatings to compensate for the ellipticity induced by total internal reflection. It is noted that these coatings are unnecessary if there is no Faraday rotation in the short sections as would be the case of a shielded rotator. The double reflections interchange the perpendicular and parallel components so that the phase shift is compensated provided no rotation occurs between reflections. This is a well-known property of an Abbé prism formed by two 45° faces whose azimuthal directions differ by 90°.

Figure 2, the assembled probe, shows the glass ring, the conducting shield, the Banning type polarizers, and the lenses for coupling the input and output beams into optical fibers. The entire cavity can be pressurized with SF_6 for insulation in high voltage applications.

Optical fibers bring the light from the He-Ne source to the ring and return the Faraday rotation signal to the detector, both of which can be located in a screened room remote from the high current being measured. Note that since the ring is placed between crossed polarizers, residual birefringence in the fibers and Faraday effect in the fibers due to stray fields do not affect the measurement. The optical fibers thus function solely as a convenient means for conveying the light to and from the ring.

3. Experimental Results

The Faraday probe was tested by use of the discharge of a capacitor bank through a straight conductor, the shield furnishing a coaxial return circuit. The bank, which consists of 15 2.25 μF capacitors in parallel, is connected to the current probe through a parallel plate transmission line with a shorting bar linking the rotator ring. The bank could be charged to 40 kV maximum.

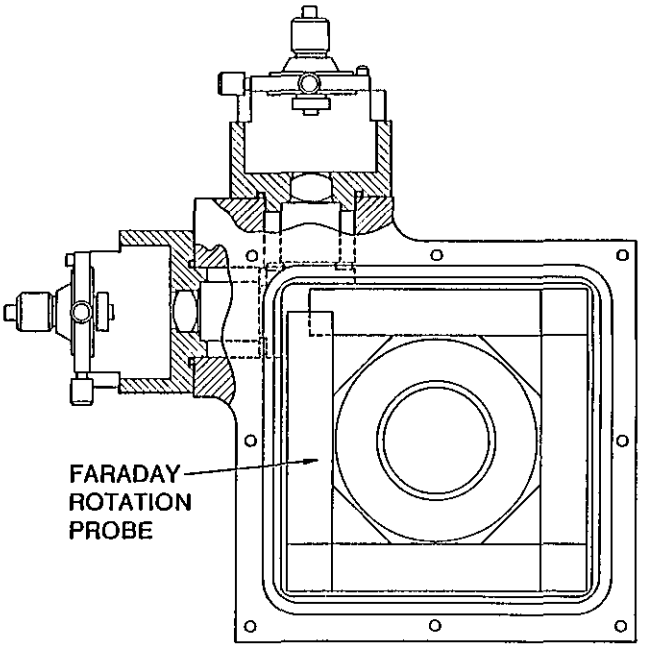

Figure 2—Drawing of assembled probe showing the glass rotator, input and output lenses and polarizers and positioners for input and output fibers.

The discharge current waveform of such a circuit is a damped sine wave. We obtain this waveform by integrating the voltage signal from a small magnetic pickup coil located in a hole in one plate of the transmission line close to the thin mylar dielectric layer that separates the two plates of the transmission line. Unfortunately this coil was inaccessible and the area and number of turns are not known so the absolute value of current could not be measured directly. We can obtain a relatively crude estimate of this value, however, by measuring the period and logarithmic decrement of the waveform. Knowing the value of capacitance C, and the charging voltage, V_0, of the bank, we can compute the total inductance $L=0.0523$ μH and the circuit resistance $R=17$ mΩ. From the elementary relationships for a simple LRC circuit

$$I=\frac{V_0}{\omega L}e^{-\alpha t}\sin\omega t \tag{11a}$$

$$\omega=[\frac{1}{LC}-\alpha^2\approx]^{1/2},\ \alpha=\frac{R}{2L}, \tag{11b}$$

we can determine the peak discharge current at the first maximum for a given initial charging voltage. The accuracy of this determination is poor because of errors in the measurement of the period and especially the logarithmic decrement from the waveform.

Using the value of the Verdet constant $V=0.082$ min/gauss-cm at 632 Å given by the supplier of the glass we can use eq (2) to compute i_π the current increment required for a complete cycle of Faraday rotation i.e., a complete fringe. The value of $i_\pi = 1.035\times10^5$ amps/fringe. We can obtain the number of half cycles of Faraday rotation N plus the excess fringe fraction ΔN from the waveform of the Faraday rotation signal. If A be the normalized amplitude of the Faraday rotation signal at time t the excess fringe fraction is given by

$$\Delta N=\frac{1}{\pi}\arcsin\,(A^{1/2}),\ N \text{ integer}, \tag{12a}$$

$$\Delta N=\left(\frac{1}{2}-\frac{1}{\pi}\arcsin\,(A^{1/2})\right),\ N \text{ half odd integer}, \tag{12b}$$

taking the principal value of the arcsin function. Note that N is either an integer or one-half times an odd integer and that ΔN varies from zero to one-half.

The corresponding current at time t is then just

$$i(t)=i_\pi[N(t)+\Delta N(t)]. \tag{13}$$

The above treatment is valid provided the current has not reached an extremum prior to t. An extremum is characterized by the failure of the Faraday rotation signal to complete a cycle, i.e., the signal reaches an extremum at an intermediate amplitude and by a marked reduction in frequency. Following such an extremum, the number of half-cycles N_2 following the extremum should be subtracted from the number of half-cycles N_1, prior to the extremum to obtain

$$i=[(N_1-N_2)-\Delta N]i_\pi \tag{14}$$

or generalizing to several extrema

$$i=[N_1-N_2+N_3-N_4+\text{----}N_i-N_j)\mp\Delta N]i_\pi. \tag{15}$$

The sign of the excess fractional fringe ΔN is taken positive for an even number of extrema and negative for an odd number. Note that the excess fractional fringe immediately before and after an extremum just cancel each other.

We can thus calculate the fringe number to the first current maximum at various charging voltages and the value of current at the first maximum using the value of i_π given above. These are compared in table 1 with those using eq (11) and the bank parameters. As one might expect the agreement is rather poor due mainly to the inaccuracy of the current determination from the oscillogram using eq (11) as mentioned before. What is more significant is the value of the current per fringe obtained by dividing the calculated current by the fringe number. The resulting values differ by less than 2%. Furthermore, if only the last three values are considered, the deviation from the mean is less than 1%. This might be expected from eq (9) since only the excess fraction depends upon the amplitude of the Faraday rotation signal and this makes an increasingly small contribution to the total current as the number of half fringes increases.

Figures 3, 4, and 5 respectively show the Faraday rotation signal for a charging voltage of 20 kV, the corresponding magnetic pickup coil signal after integration, and the waveform obtained by numerical inversion of the Faraday signal. This latter waveform is virtually identical to that of the integrated magnetic pick-up coil signal.

4. Conclusions

We have designed, constructed, and tested a current probe based upon the Faraday rotation angle of polarized light produced by propagation of the light along a light path encircling the current to be measured. Such a probe is an absolute instrument whose calibration depends upon the Verdet constant of the rotative medium independent of the dimensions or position of the light path.

The claim for an absolute instrument is not based upon our rather limited experimental work. This work

Table 1.

Bank Voltage KV	No. of Faraday Fringes to First Current Maximum N	Maximum Current Calculated from Circuit Parameters kA	Maximum Current from Faraday Effect $Nx1.035\times10^5$ kA	Current per Fringe, I_{II} Using Calculated Current kA
15	3.41	322	353	94.4
20	4.63	429	479	92.7
25	5.83	537	603	92.1
30	7.00	644	667	92.0

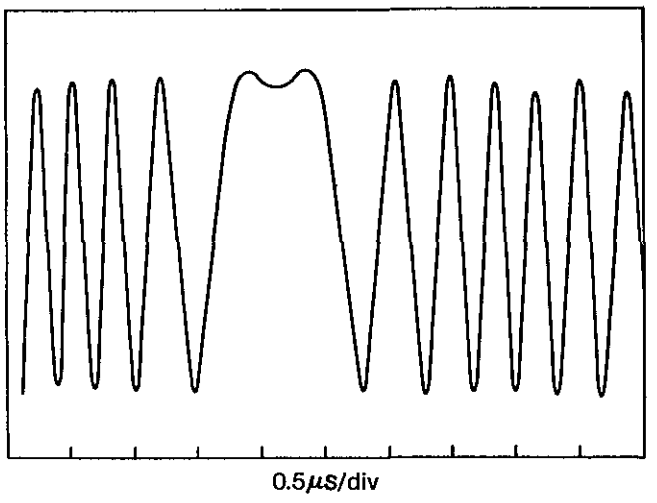

Figure 3—Faraday rotation signal.

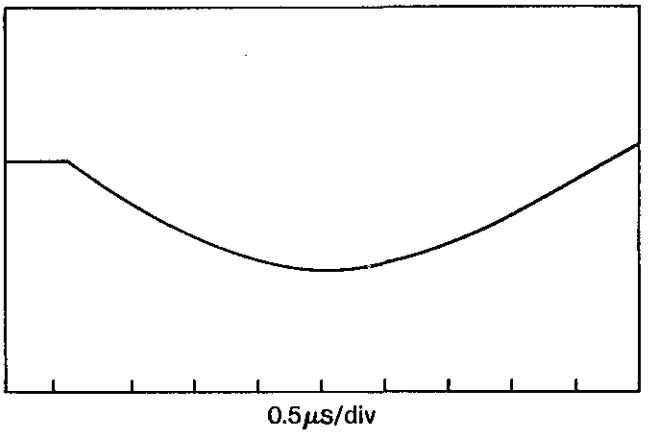

Figure 4—Bank discharge waveform corresponding to Faraday rotation signal in figure 3 obtained with a magnetic pickup coil and integrated.

had to be curtailed because of a lack of funding and really constitutes only a proof of principle. This claim rests upon the elimination of positional and geometric factors in the calibration of the probe and the fact that the Verdet constant of a diamagnetic medium depends only upon the dispersion curve of the medium and is not affected appreciably by mechanical or temperature effects [8].

It is true that the subtractive contribution of the even-ordered light path segments does complicate the claim of insensitivity to positional and geometric factors. Our design of the probe addresses this question by 1) ensuring that the odd-ordered segments alone make up the complete circuital path, 2) making the even-ordered segments as short as possible and orienting them as nearly as possible normal to the magnetic field direction, and 3) using a suitable conducting shell to shield out the poloidal magnetic field components which alone can

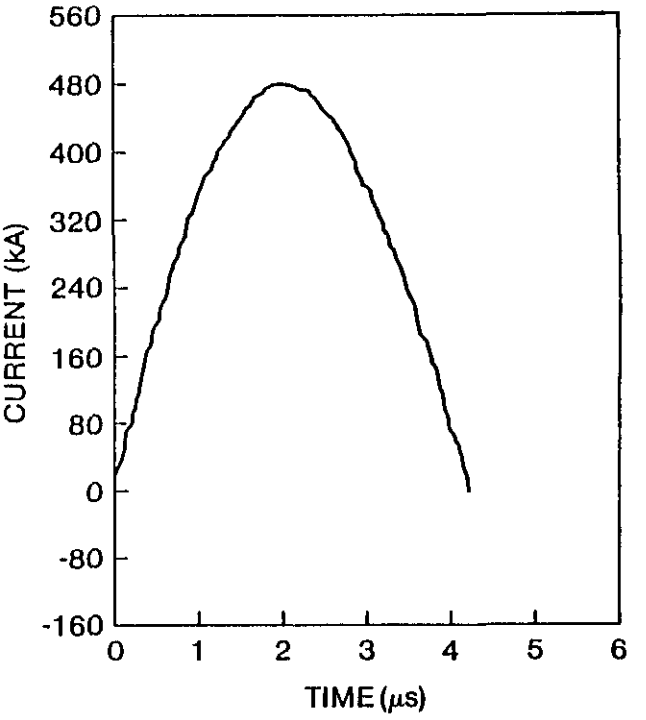

Figure 5—Numerical inversion of Faraday signal in figure 3.

contribute to the line integral of the field along these even-ordered segments.

As mentioned before, we rejected the use of the rare-earth doped glasses for use in the probe even though their Verdet constants are three times those of the diamagnetic glasses employed. This was on account of the temperature dependence of their Verdet constants.

This probe is intended for measurement of very fast transient currents in the mega-ampere range for which it is well suited. For slower varying currents of smaller magnitude, this type of probe can still be used by increasing the number of circuital paths either by multiple light transits or the use of multi-turn optical fibers [2,3]. Since the time resolution is limited to the light transit time between polarizers, the increase in current sensitivity is realized at the price of a longer resolution time.

We wish to acknowledge John Shannon, Mark Wilkinson, and Norman Rostoker of Maxwell Laboratories, Inc., for their many valuable discussions; Leslie Vargady of Metrooptics Company, Glendora, CA, for the skillful and dedicated design and fabrication of the rotator ring; Lawrence Houghton and David Lischer of Maxwell for their devoted assistance with the experi-

mental work; and Clifford Fowler, also of Maxwell, for developing the algorithm for the numerical inversion of the Faraday signal.

References

[1] Hebner, R. E.; R. A. Malewski and E. C. Cassidy, *Proc. IEEE 65*, part 2, p. 1524 (1977).
[2] Massey, G. A.; D. C. Erickson and R. A. Kadlec, Applied Optics **14**, 2712 (1975).
[3] Smith, A. M. Applied Optics **17**, 52 (1978).
[4] Papp, A. and H. Harms, Applied Optics **19**, 3729 (1980).
[5] Aulich, H.; W. Beck, N. Douklias, H. Harms, A. Papp, and H. Schneider, Applied Optics **19**, 3735 (1980).
[6] Harms, H., and A. Papp, Applied Optics **19**, 3741 (1980).
[7] Kard, P. G. Optics and Spectroscopy **6**, 339 (1959).
[8] Becker, R. *Theorie der Elektrizitat*, Vol. II, p. 142-150, B. G. Teubner, Leipzig and Berlin 1933.
[9] Barlow, A. J.; J. J. Ramskov-Hansen and D. N. Payne, Applied Optics **20**, 2962 (1981).

JOURNAL OF RESEARCH of the National Bureau of Standards
Vol. 89, No. 3, May-June 1984

A Head-Space Method for Measuring Activity Coefficients, Partition Coefficients, and Solubilities of Hydrocarbons in Saline Solutions

Stanley P. Wasik, Frederick P. Schwarz, Yadu B. Tewari, and Michele M. Miller

National Bureau of Standards, Gaithersburg, MD 20899

and

J. H. Purnell

University College of Swansea, Swansea, Wales, UK

Accepted: February 2, 1984

An apparatus is described which measures the equilibrium distribution of a hydrocarbon between a gas and aqueous phase. Soluble hydrocarbons are extracted from an aqueous salt solution by very small bubbles of hydrogen generated electrolytically from a gold electrode located at the bottom of a cylindrical cell. The partition coefficient is determined from the volume of the aqueous solution and the solute concentration in the head-space after a measured volume of hydrogen has bubbled through the cell. The concentration of the solute in the head-space is measured by gas chromatography. The observed distribution is supplemented by vapor pressure and molar volume data and can be used to calculate the solubility and the activity coefficient of the solute in the aqueous phase. The partition coefficient, activity coefficient, and solubility for 18 alkylbenzenes in aqueous 0.5 M NaCl at 25 °C were measured by this method.

Key words: activity coefficient; aqueous solubility; head-space; partition coefficient.

Introduction

A knowledge of the equilibrium properties of aqueous hydrocarbon solutions is valuable in several fields. In water pollution control, such information is helpful in devising abatement processes [1][1], in modeling natural water systems [2], in designing toxicity experiments, and in developing analytical methods. In petroleum research, it is useful for understanding how hydrocarbons migrate and accumulate to form oil deposits [3]. In biology, a knowledge of how hydrocarbons behave in aqueous solutions is important for understanding the effects of hydration on the configuration of biopolymers [4]. In chemistry, experimental data on these systems are needed for testing models of water and aqueous solutions [5].

These aqueous solutions can be characterized by determining the concentration of a particular hydrocarbon in both the solution and the vapor in equilibrium with solution. The ratio of the solute concentration in the two phases is a stoichiometric equilibrium constant, commonly called the partition coefficient, K. The solubility may be determined from the value of K and the solute saturation vapor pressure. Another thermodynamic property of interest is the solute activity coefficient based on volume fraction, γ_ϕ, which may be calculated

About the Authors: Stanley P. Wasik, who like his fellow NBS authors is a research chemist in the Bureau's Center for Chemical Physics, did some of the work reported on here while on sabbatical leave at the University College of Swansea where J. H. Purnell is a professor of chemistry and a researcher.

[1] Figures in brackets indicate literature references at the end of this paper.

from the value of K, the solute molar volume, and the solute saturation vapor pressure. This property is of particular importance in developing correlations based on some additive property of the solute, such as molar volume or carbon number, since γ_ϕ depends only weakly on temperature and varies significantly less with solute structure and configuration than does the corresponding correlation with solubilities or with the mole fraction-defined activity coefficient, γ_x.

We have previously described a method for measuring K using a head-space technique [6, 7, 8] which is best suited for measuring K in the range $1-10$. We now report a method without limitations on the value of K. In this method, the soluble hydrocarbons are extracted from aqueous salt solutions by very small bubbles of hydrogen generated electrolytically from a gold electrode located at the bottom of a cylindrical cell. The partition coefficient is determined from the volume of aqueous solution and the solute concentration in the head-space after a measured volume of hydrogen has bubbled through the cell. The concentration of the hydrocarbon in the head-space is analytically determined by conventional gas chromatography. The partition coefficients, solubilities, and activity coefficients for 18 alkylbenzenes in aqueous 0.5 M NaCl at 25 °C measured by this method are reported here.

Experimental

Figure 1 shows the extraction cell. The compartments A and B have internal volumes of 50 and 40 ml, respectively. The two compartments are connected by means of a 14 mm o.d. glass tube with a 10 mm o.d. coarse porosity glass frit on one end. A silicic acid plug is precipitated on the compartment B side of the frit to prevent the flow of liquid from one compartment to another and to provide low resistance for the flow of electric current. The gold electrode (1 mm o.d. wire) in compartment A is positioned by means of a septum held in a $1/4\times 1/4$ in union fitting. This electrode has a spiral configuration to provide a large surface area. The electrode in compartment B is a straight segment of 1 mm o.d. platinum wire.

The extraction cell is immersed in a bath controlled to ± 0.02 °C. The thermometer used in this work was calibrated with an accuracy of ± 0.01 °C by the National Bureau of Standards. The head-space is sampled by a gas injection valve thermostated at 150 °C. The 1/8 in o.d. stainless steel tube connecting the extraction cell with the valve is heated to 150 °C by a heating tape.

The chromatographic column is a 15 m$\times$0.5 mm i.d. *SCOT* column prepared with finely ground diatomaceous earth on a fused silica support and coated with a mixture of m-bis(m-phenoxy phenyl) benzene and Apiezon L. The effluent is monitored by a hydrogen flame detector with an electronic integrator measuring peak areas.

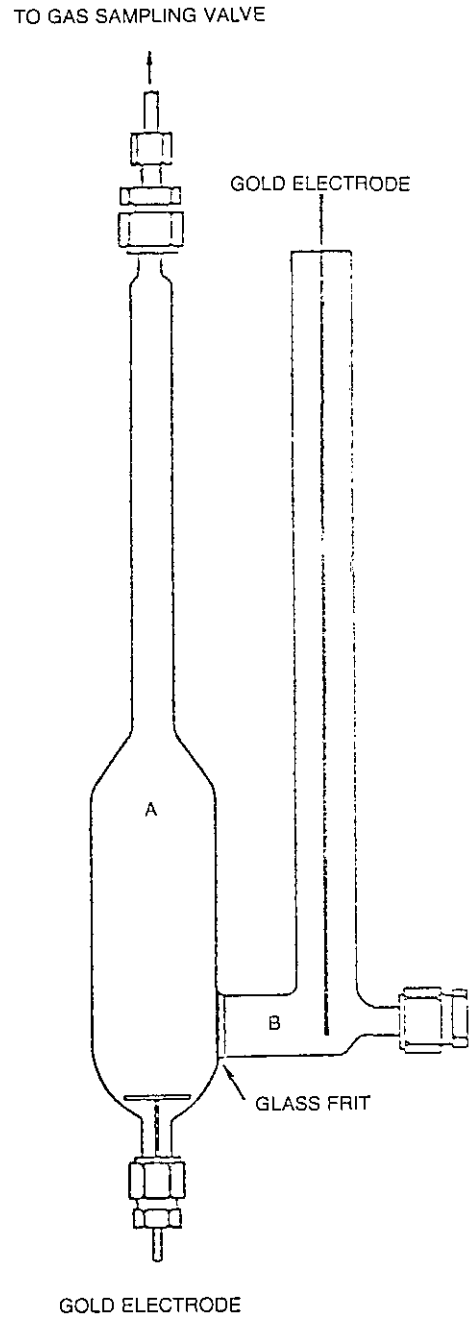

Figure 1—Extraction cell compartments A and B have internal volumes of 50 and 40 ml, respectively.

A constant current power supply with a stability of 1/10,000 provides electrical current to the extraction cell. The volume of hydrogen plus water vapor, V, bubbled through compartment A is calculated from the equation

$$V=(it/2F)\,[RT/(p_A-p_w)] \tag{1}$$

where i is current; t, the time in seconds; F, the Faraday constant; R, the gas constant; p_A, the atmospheric pressure; and p_w, the vapor pressure of the aqueous solution at temperature T(K).

The aromatic hydrocarbons used in this study had a stated purity of 99.9 mole %. The water used in the preparation of solutions was doubly distilled over potassium permanganate.

Procedure

A mixture of several of the alkylbenzenes was prepared such that their partial pressures at 25 °C were approximately the same. Five ml of the mixture was gently stirred with 100 ml of aqueous 0.5 M NaCl for 2 h and then allowed to stand overnight. Compartment A was filled with the aqueous solution leaving only a small volume of head-space (<1.0 ml) above the solution. The volume of the solution was determined from the weight of the cell before and after filling and from the density of the solution. Compartment B was filled to the same level as compartment A with 5% v/v H_2SO_4 solution. The extraction cell was then immersed in the constant temperature bath for 1 h before electric current (0.2–0.4 amp) was passed through the cell. A small volume of the head-space (0.3 mL) was injected into the gas chromatograph via the gas sampling valve for analysis. The alkylbenzenes were chosen so that there was a baseline separation for each peak. The peak areas were recorded along with the time of sample injection. This procedure was repeated every 10 min until the peak areas were approximately 1/100 their original value.

In order to measure the peak area corresponding to the solute saturation vapor pressure three columns were constructed of stainless steel tubing, 2.5 mm i.d. and 0.5 m in length. The solid support was Chromosorb W (60–80 mesh) with toluene, ethylbenzene, and n-propylbenzene as the stationary phase, respectively. Each column was immersed in the constant temperature bath, and helium saturated with water vapor was allowed to flow through it before being sampled for analysis.

Thermodynamic Background

Consider a known volume, V_L, of aqueous salt solution of hydrocarbons in a cylindrical vessel containing a gold electrode at the bottom. Connected to this vessel by means of a glass fritted disc is another vessel containing an aqueous solution of H_2SO_4. When electric current with the appropriated polarity passes through the cell, hydrogen in the form of very small bubbles is evolved at the electrode in the vessel containing the aqueous solution, and oxygen is evolved at the other electrode. Water vapor and the dissolved hydrocarbons in the aqueous solution are equilibrated with the hydrogen bubbles. The hydrocarbon concentrations in the head-space are measured by means of gas chromatography. We may assume that the concentration of a particular hydrocarbon in the head-space is proportional to its concentration in the aqueous solution. One then has the relationship

$$C_{wi}(v)=K_i\,C_{hi}(v) \tag{2}$$

where $C_{wi}(v)$ and $C_{hi}(v)$ are the concentrations of the i^{th} hydrocarbon in the aqueous solution and in the head-space, respectively, after a volume V of hydrogen plus water vapor has bubbled through the cell and K_i is the proportionality factor. Under equilibrium conditions K_i would be the partition coefficient. Conservation of mass requires that the ratio of $C_{hi}(V)$, corresponding to the passage of volume V, to its value, $C_{hi}(0)$, at zero hydrogen volume is given by the expession

$$\ln\,[C_{hi}(V)/C_{hi}(0)]=-V/(V_L\,K_i) \tag{3}$$

The peak area for the i^{th} hydrocarbon, $A_i(V)$ may be expressed as

$$A_i(V)=\sigma_i\,C_{hi}(V)\,V_s \tag{4}$$

where σ_i is the instrument sensitivity constant for the i^{th} hydrocarbon and V_s is the volume of the gas sampling valve sample loop. Substituting for $C_{hi}(V)$ in eq (3),

$$\ln\,[A_i(V)/A_i(0)]=-V/V_L\,K_i. \tag{5}$$

A plot of ln $A_i(V)$ versus V (or time) should thus be linear if K_i is constant, and the slope will give the value of K_i.

The attainment of equilibrium of the dissolved hydrocarbons in the aqueous solution with the hydrogen bub-

bles depends on the size of the bubbles and the contact time. Hydrogen bubbles generated electrolytically are less than 0.1 mm in diameter. Under these conditions the bubbles are small enough and the contact time with the solution long enough that equilibrium would be expected before the bubbles reached the surface, and the measured K_i should be the partition coefficient.

During the course of the measurements water is continually being removed from the generating cell as saturated water vapor. For measurements near room temperature the amount of water removed is very small ($<0.1\%$); hence, no corrections are made for this effect.

Activity Coefficient

The partition coefficient K_i may be defined as

$$K_i=\frac{C_{wi}(\mathrm{v})}{C_{hi}(v)}=\left(\frac{n_i}{V_L}\right)\frac{RT}{P_i} \tag{6}$$

where n_i is the number of moles of the i^{th} hydrocarbon, P_i is the partial pressure of hydrocarbon at temperature T, R is the gas constant, and V_L is the total volume of aqueous solution. The partial pressure (P_i) may be expressed in terms of volume fraction-based activity coefficient ($\gamma_{\phi i}$) as

$$P_i=\gamma_{\phi i}\phi_i P_i^o \tag{7}$$

where P_i^o is the saturated vapor pressure of the solute and ϕ_i is the solute volume fraction combining eqs (6) and (7) we get

$$K_i=\frac{RT}{\gamma_{\phi i}V_i P_i^o} \tag{8}$$

where V_i is the molar volume of the i^{th} hydrocarbon at temperature T.

Solubility

In order to calculate the hydrocarbon aqueous solubility from K values, it is essential that the hydrocarbon concentration in the aqueous phase be proportional to its concentration in the gas phase, P_i/RT, up to the solute saturation vapor pressure, p_i^o, i.e., a two-phase system, liquid solute and aqueous solution saturated with solute. Under these conditions

$$K=C_w^o RT/p^o \tag{9}$$

where C_w^o is the solubility of the solute temperature T. When liquid hydrocarbon is present at equilibrium with an aqueous phase, it will dissolve some water. The amount of water dissolved is so small, however (the solubility of water in all hydrocarbons at 25 °C is well under $x=0.01$) that no correction need be made for its effect on the hydrocarbon's vapor pressure.

Results and Discussion

Ln $A(V)$ versus V plots (eq (5)) for some alkylbenzenes in which the initial aqueous solution was saturated with the solute indicate that the proportionality between solute concentration in the gas phase and aqueous phase holds up to the solute saturation concentration in the aqueous phase (solubility) and that eq (9) may be used to calculate solubilities for these compounds. Values for ln A_i (0) (time equal to zero) were obtained from the saturation vapor pressure at 25 °C using pure solute.

The partition coefficients were calculated from the slopes of the $\ln A_i(V)$ versus V plots for the alkylbenzenes. These values are given in table 1 along with values of the solute activity coefficients calculated via eq (8). For comparison, values of the solute activity coefficients calculated from solubility data measured using the generator column method [10] are given in the same table. The good agreement between the two sets of data justifies the assumption made in deriving eq (7), i.e., $\gamma_\phi \neq 1$ for an apolar solute in equilibrium with an aqueous phase.

The head-space method proposed in this paper may be used to measure K for any type of compound. The largest error in the measurements comes from measuring peak areas. Since one needs to know the peak area at time t, as well as the peak area corresponding to the saturation vapor pressure, the average error in the partition coefficients is approximately 1.5%.

The method has a disadvantage in that K can be measured only in salt solutions since some electrolyte is required in the solution to conduct the electrical current. In order to determine K in pure water, K must be measured in salt solutions of differing concentration, C_s, and then extrapolated to zero salt concentration using Setchenow's expression

$$\log(K^w/K^{sw})=k_s C_s \tag{10}$$

where K^w is the solute partition coefficient in water, K^{sw} is the solute partition coefficient in salt water of concentration C_s, and k_s is the salting-out coefficient.

Table 1. Partition coefficients, solubilities and activity coefficients for alkylbenzenes in aqueous 0.5 M NaCl at 25.0 °C.

Solutes	P_2 (mm)	V_i (mL/mole)	$K_{a/w}$	$C_s^w \times 10^3$ (M)	log γ_ϕ
Benzene	95.18	89.4	3.47±0.03	17.76	2.799
Toluene	28.45	106.9	2.74±0.02	4.19	3.349(3.292)[1]
Ethylbenzene	9.51	123.1	2.19±0.02	1.12	3.861(3.809)
1,2-Dimethylbenzene	6.62	121.2	3.52±0.02	1.25	3.820(3.735)
1,4-Dimethylbenzene	8.84	123.9	2.24±0.02	1.06	3.882
n-Propylbenzene	3.43	140.1	1.53±0.01	0.282	4.403(4.419)
Isopropylbenzene	4.64	140.2	1.20±0.001	0.299	4.378(4.260)
1,3,5-Trimethylbenzene	2.61	139.6	2.01±0.01	0.282	4.405
1,2,4-Trimethylbenzene	2.096	137.9	2.78±0.02	0.313	4.365
2-Ethyl-1-Methylbenzene	2.521	137.1	2.66±0.02	0.361	4.305
3-Ethyl-1-Methylbenzene	2.999	139.7	1.69±0.02	0.273	4.419
n-Butylbenzene	1.011	156.8	1.18±0.01	0.0642	4.997(4.952)
Isobutylbenzene	1.929	158.1	0.677±0.01	0.0702	4.955
sec-Butylbenzene	1.873	156.4	0.870±0.01	0.0876	4.863
t-Butylbenzene	2.208	155.6	1.13±0.01	0.134	4.681
1,3-Diethylbenzene	1.134	156.1	1.22±0.01	0.0744	4.935
1,2-Diethylbenzene	1.043	153.2	1.81±0.02	0.1015	4.794
1,4-Diethylbenzene	1.051	156.4	1.26±0.01	0.0712	4.953

[1] The values in brackets are calculated from experimental solubility data using the equation $\gamma_\phi = (C_s^w V_i)^{-1}$ where V_i is the molar volume of the solute [10].

References

[1] Tsonopoulos, C. and J. M. Prausnitz. Activity coefficients of aromatic solutes in dilute aqueous solutions. Ind. Eng. Fundam. **10** (4): 493-600; 1971.

[2] LeFeurre, A. R. *Water and Water Pollution Handbook*, Vol. 1; Ciaccio, L. L., editor. New York: Marcel Dekker, Inc.; 1971. 263.

[3] Peake, E., and G. W. Hodgson. Alkanes in aqueous systems. I. Exploratory investigations on the accommodation of $C_{20}-C_{33}$ n-alkanes in distilled water and occurrence in natural water systems. J. Am. Oil Chemists Soc. **4**: 215-222; 1966.

[4] Ben-Naim, A. Statistical mechanical study of hydrophobic interactions. III. Generalization and further applications, J. Chem. Phys. **57** (12): 5257–5265; 1972.

[5] Ben-Naim, A. *Water and Aqueous Solutions*; Horne, R. A., editor. New York: Wiley; 1972. 452.

[6] Wasik, S. P.; R. L. Brown, and J. I. Minor, Jr. Partition coefficients and solubility measurements of dimethylmercury in fresh and sea water over a temperature range 0–25 °C. J. Environ Sci. Health. **A11** (1): 99–105; 1976.

[7] Brown, R L., and S. P. Wasik. A method of measuring the solubilities of hydrocarbons in aqueous solutions. NBS J. Res. **78A** (4): 453–460; 1974.

[8] Wasik, S. P. Partition of organoelements in octanol/water/air systems, Chap. 19 in *Organometals and Organometalloids*; Brinckman, F. E. and J. M. Bellama, editors. Washington, DC: ACS; 1978; 314–326.

[9] Wasik, S. P.; Y. B. Tewari, M. M. Miller, and J. H. Purnell. Measurements of the octanol/water partition coefficient by chromatographic methods. NBS J. Res. **87** (4): 311–315; 1982.

[10] Tewari, Y. B.; M. M. Miller, S. P. Wasik, and D. E. Martire. Aqueous solubilities and octanol/water partition coefficient of organic compounds at 25.0 °C. J. Chem. Eng. Data. **27** (4): 451–454; 1982.